ADVANCED MASTERS IN STRUCTURAL ANALYSIS
OF MONUMENTS AND HISTORICAL CONSTRUCTIONS

Master's Thesis

Evandro Araldi

Identification of the mechanical behavior of rammed earth including water content influence

Evandro Araldi

Czech Republic | 2017

Czech
Technical
University
IN PRAGUE

UPC
UNIVERSITAT POLITÈCNICA
DE CATALUNYA

Education and Culture

Erasmus Mundus

ARCCHIP

UPC

ADVANCED MASTERS IN STRUCTURAL ANALYSIS
OF MONUMENTS AND HISTORICAL CONSTRUCTIONS

Master's Thesis

Evandro Araldi

Identification of the mechanical behavior of rammed earth including water content influence

MASTER'S THESIS PROPOSAL

study programme:	Civil Engineering
study branch:	Advanced Masters in Structural Analysis of Monuments and Historical Constructions
academic year:	2016/2017

Student's name and surname:	Evandro Araldi
Department:	Department of Mechanics
Thesis supervisor:	Prof. Ing. Petr Kabele, Ph.D.
Thesis title:	Identification of the mechanical behavior of rammed earth including water content influence
Thesis title in English	see above

Framework content: This work comes first to identify the different plastic failure surfaces on rammed earth by means of experimental tests on different stress paths. This failure surfaces are the ones involved in a new constitutive model (CJS-RE) specially developed for rammed earth at the University of Lyon. Moreover, the role of the water content on the mechanical behavior was addressed. The set of experimental results are discussed and some prospects for future studies are indicated

.

Assignment date:	7/04/2017	Submission date:	10/09/2017

If the student fails to submit the Master's thesis on time, they are obliged to justify this fact in advance in writing, if this request (submitted through the Student Registrar) is granted by the Dean, the Dean will assign the student a substitute date for holding the final graduation examination (2 attempts for FGE remain). If this fact is not appropriately excused or if the request is not granted by the Dean, the Dean will assign the student a date for retaking the final graduation examination, FGE can be retaken only once. (Study and Examination Code, Art 22, Par 3, 4.)

The student takes notice of the obligation of working out the Master's thesis on their own, without any outside help, except for consultation. The list of references, other sources and names of consultants must be included in the Master's thesis.

....
Master's thesis supervisor   Head of department

Date of Master's thesis proposal take over: September 2017

....
Student

DECLARATION

Name: Evandro Araldi

Email: pf.evandro@gmail.com

Title of the
Msc Dissertation: *Identification of the mechanical behavior of rammed earth including water content influence*

Supervisor(s):   Eric Vincens; Petr Kabele

Year: 2017

I hereby declare that all information in this document has been obtained and presented in accordance with academic rules and ethical conduct. I also declare that, as required by these rules and conduct, I have fully cited and referenced all material and results that are not original to this work.

I hereby declare that the MSc Consortium responsible for the Advanced Masters in Structural Analysis of Monuments and Historical Constructions is allowed to store and make available electronically the present MSc Dissertation.

University: Czech Technical University in Prague

Date: September 10th, 2017

Signature:

_____

ACKNOWLEDGEMENTS

ABSTRACT

Identification of the mechanical behavior of rammed earth including water content influence

Rammed earth constructions can be found in many regions around the world, generally within territories where the access of earth was easy contrary to other historic-traditional materials, e.g. stone. The great number of historical earthen structures and the need to protect their heritage values come with the resurgence of a modern interest in rammed earth, mainly due to its environmental benefits. However, the lack of regulation and codes to guide the design and the conservation of earthen constructions characterizes the main disadvantage of the material. Funded by a French national project devoted to rammed earth, a new constitutive model (CJS-RE) was developed at the *Laboratoire de Tribologie et Dynamique des Systèmes* (LTDS), at the University of Lyon. However, due to the lack of data some statements were considered. This work comes first to contribute with the experimental identification of failure surfaces along different stress paths (compression, extension and tensile stress path) on rammed earth based on CJS-RE model. Additionally, the experimental stress-strain relationship obtained for compression is compared with the one resulted by CJS-RE model. Results showed that CJS-RE is a great approach for describing the behavior of rammed earth material. The stress-strain relationship was strongly suitable when compared the one obtained by the unconfined compressive tests. As a result of the identification of the plastic parameters, a very strong dissymmetry between compression and extension stress paths of shear failure surface was observed.

A second issue regarding rammed earth behavior lies on the uncertainties about the influence of water content on the mechanical properties of the material. Earth is herein a mixture of different granular classes that are bonded together by clayey particles. The material is processed with sufficient additive water and then compacted. The mechanical resistance only develops over time when most of water has left the material due to evaporation. This resistance results from the creation of strong capillary tensile bonds within the pore network that play the role of a binding agent. At any moment in the building lifetime, these tensile forces can be destroyed if the water content accidentally increases (rain, capillary rise within the walls), which can lead the structure to failure. Within the framework of the national research project PRIMATERRE, funded by the French Agency of Research, there is a need to understand how the mechanical properties of earth are influenced by the water content. Thus, two different water contents are evaluated and a third is proposed as further research. Results indicated that most of the parameters from CJS-RE had a decrease about 30% to 40% regarding the increase of water content from 2% to 4%. The dissymmetry parameter, however, was reduced by 3%. The radius at failure was the only parameter which was has increased, showing a difference of 8%.

Key-words: rammed earth; mechanical behavior; plasticity

ABSTRAKT

Identifikace mechanického chování dusané hlíny při zohlednění vlivu obsahu vody

Stavby z dusané hlíny se vyskytují v mnoha oblastech po celém světě, obecně na územích, kde byla hlína dostupnější ve srovnání s jinými historickými tradičními materiály, jako je např. kámen. V současné době je třeba chránit velké množství historických hliněných staveb jako kulturní dědictví a zároveň vzrůstá zájem o moderní využití dusané hlíny, a to především kvůli přínosu této technologie pro životní prostředí. Hlavní nevýhodu této technologie lze spatřovat v chybějících normách pro navrhování a preventivní údržbu hliněných konstrukcí. S finanční podporou francouzského národního projektu zaměřeného na dusanou hlínu byl v *Laboratoire de Tribologie et Dynamique des Systèmes* (LTDS) na univerzitě v Lyonu vyvinut nový konstitutivní model (CJS-RE). Nicméně, vzhledem k nedostatku je třeba některé aspekty dořešit. Příspěvkem této práce je v prvé řadě experimentální identifikace ploch porušení při různých trajektoriích napětí (tlak, protažení a tah) pro model dusané hlíny CJS-RE. Dále jsou porovnány experimentálně získané vztahy napětí-deformace v tlaku pro dusanou hlínu s výsledky modelu CJS-RE. Výsledky ukázaly, že CJS-RE je skvělým přístupem k popisu chování dusané hlíny. Zejména vztah mezi napětím a deformací v prostém tlaku byl velmi dobře reprodukován. Vyhodnocené parametry plasticity poukazují na velmi silnou asymetrii smykové plochy porušení při namáhání tlakem a protažením.

Druhá otázka týkající se chování dusané zeminy spočívá v nejistotách ohledně vlivu obsahu vody na mechanické vlastnosti materiálu. Zemina je směs částic různých tříd zrnitosti, které jsou spojeny jílovitými částicemi. Materiál se zpracovává s dostatkem přidané vody a pak se zhutní. Mechanická odolnost vzrůstá pouze po určitém čase, poté kdy se většina vody odpaří. Tato odolnost je důsledkem vytvoření silných kapilárních vazeb v pórové struktuře, které působí jako pojivo. V každém okamžiku životnosti stavby mohou být tyto vazby zničeny, pokud se náhodně zvýší obsah vody (v důsledku deště, kapilárního vzlínání ve stěnách), což může vést k selhání konstrukce. V rámci národního výzkumného projektu PRIMATERRE, financovaného Francouzskou agenturou pro výzkum, je třeba objasnit, jak jsou mechanické vlastnosti zeminy ovlivněny obsahem vody. Proto byly vyhodnoceny vzorky se dvěma různými úrovněmi obsahu vody a třetí byl navržen pro další výzkum. Výsledky ukázaly, že většina parametrů modelu CJS-RE vykazuje pokles o přibližně 30% až 40% při nárůstu obsahu vody z 2% na 4%. Parametr asymetrie však klesl o 3%. Poloměr při porušení byl jediným parametrem, který se zvýšil, a to o 8%.

Klíčová slova: dusaná hlína; mechanické chování; plasticita

RESUMO

Identificação do comportamento mecânico da taipa incluindo a influência do teor de água.

Construções em taipa (terra batida) podem ser encontradas em muitas regiões ao redor do mundo, geralmente inseridas em territórios onde o acesso à terra era fácil, ao contrário de outros materiais tradicionalmente históricos, como por exemplo a pedra. O grande número de estruturas históricas de terra existentes e a necessidade de proteger os seus valores como patrimônio juntam-se com o ressurgimento de um interesse moderno da taipa, principalmente devido aos seus benefícios ambientais. No entanto, a falta de regulamentos e normas para guiar o projeto e a conservação de construções em terra caracteriza-se como a principal desvantagem do material. Patrocinado por um projeto nacional francês dedicado à taipa, um novo modelo constitutivo (CJS-RE) foi desenvolvido no *Laboratoire de Tribologie et Dynamique des Systèmes* (LTDS), na Universidade de Lyon. No entanto, devido à falta de dados, alguns pressupostos foram considerados. Este trabalho surge primeiramente para contribuir na identificação experimental das falhas de rupturas ao longo de diferentes caminhos de tensão (compressão, extensão e tração), com base no modelo CJS-RE. Adicionalmente, a curva experimental de tensão-deformação obtida à compressão é comparada com aquela resultante do modelo CJS-RE. Os resultados mostraram que o CJS-RE é uma ótima abordagem para descrever o comportamento do material da taipa. A relação tensão-deformação adequou-se fortemente quando comparada àquela obtida pelos testes de compressão não-confinados. Como resultado da identificação dos parâmetros de plasticidade, uma grande dissimetria entre o caminho de tensão à compressão e à extensão da superfície de ruptura ao cisalhamento foi observada.

Uma segunda questão a respeito do comportamento da taipa reside nas incertezas quanto à influência do teor de água nas propriedades mecânicas do material. Neste caso, a terra é uma mistura de diferentes classes granulométricas que são unidas por partículas argilosas. O material é processado com adição suficiente de água e então compactado. A resistência mecânica somente se desenvolve com o tempo quando a maior parte da água deixa o material através da evaporação. Essa resistência resulta da criação de fortes ligações de tração capilar dentro da rede de poros que desempenham o papel de agentes ligantes. Em qualquer momento da vida-útil da construção, estas forças de tração podem ser destruídas se o teor de água aumentar acidentalmente (chuva ou ascensão capilar dentro das paredes), o que pode levar a estrutura à ruptura. No âmbito do projeto de pesquisa nacional PRIMATERRE, financiado pela Agência Francesa de Pesquisa, há a necessidade de entender como as propriedades mecânicas da terra são influenciadas pelo teor de água. Assim, dois teores de água diferentes são avaliados e um terceiro é proposto como pesquisa adicional. Os resultados indicaram que a maior parte dos parâmetros do CJS-RE tiveram uma redução aproximadamente de 30% a 40% em relação ao crescimento do teor de água de 2% para 4%. O parâmetro de dissimetria, entretanto, reduziu em 3%. O raio de ruptura foi o único parâmetro a aumentar, mostrando uma diferença de 8%.

Palavras-chave: construção em taipa; comportamento mecânico; plasticidade

TABLE OF CONTENTS

LIST OF FIGURES

ANNEXES AND APPENDICES

LIST OF TABLES

ANNEXES AND APPENDICES

1. INTRODUCTION

This work is dedicated to the study of rammed earth, an ancient construction practice based on earth material which has survived through decades and now is resurging as a sustainable technique. The main objective of this work is to determine the key parameters included in an elasto-plastic model (CJS-RE) for a rammed earth material. It implies to perform tests under different stress paths. Additionally, this work contributes for a first assessment to the influence of variation of water content on the mechanical behavior of rammed earth and more precisely on the model parameters of CJS-RE.

1.1 Context and motivations

This section comprises the context of earthen constructions on the heritage field, the exposure of the main characteristics of rammed earth technique and the importance of controlling water content for the proper structural and material behavior. In fact, there are several types of construction techniques based on earth material, from which some are briefly characterized here, including rammed earth technique (D'Monte, 2009; Silva *et al.*, 2012):

> a) rammed earth (*pisé* in French, *taipa* in Portuguese, *tapial* in Spanish, *hlína dusaná do bednění* in Czech): layers of compacted moist earth between a removable formwork to make a homogeneous mass wall;
>
> b) adobe (mud blocks): blocks made from sand, clay and water to which straw is often added. Some fibrous or organic materials may also be included. The blocks are shaped using frames and then left to dry in sun. Adobes are used to build masonry walls, arches, vaults or domes, with usually an earth mortar;
>
> c) cob: contains earth, water and straw or other fibers, such like adobe, but normally applied and shaped by hand in large ball-shape cobs for the building process;
>
> d) wattle-and-daub: a wooden structure covered and filled by a sticky material usually made of wet soil, clay, sand, straw and sometimes also animal dung;
>
> e) compressed earth block (CEB): a mix of mud, sand, silt and clay in appropriate proportions (usually low clay content), which is shaped in blocks and then mechanically compressed in a press with high pressure. Binders are frequently added to the mix to increase strength. This is the most standardized from all the techniques.

1.1.1 Earthen constructions on the heritage background and current interest

Historical buildings preserve many values involving different aspects from cultural to economic resources. The International Scientific Committee on the Analysis and Restoration of Structures of Architectural Heritage (ISCARSAH) and the International Council on Monuments and Sites (ICOMOS) provide the most important proceedings and guidelines (ISCARSAH, 2014; ICOMOS, 2016) to increase the perception of cultural heritage values from structures of different materials.

Up to few years ago, most of studies were concentrated on historic-traditional materials such as stone, brick masonry, wood, and steel, since they are commonly found on heritage constructions (Soria, Guerrero and García, 2011). Published archaeological reports about earth constructions are extremely rare to find (Syrová and Syrový, 2012). For Guerrero Baca (2006), the lack of interest in earth was explained by the limited quantity of systematic documentation related to the design and construction with this material. Because most of earthen constructions are abandoned due to a certain vulnerability – for example to earthquakes –, the material evidences are in general lost or not proper for analysis.

Despite this reduced level of scientific knowledge, there is still a great number of ancient earthen structures over the world. For example, some sections of the famous Great Wall of China, such as the Jiayuguan fort, were built using different local materials, including rammed earth (Bui *et al.*, 2009). Earthen built heritage requires special attention to comprehensively understand the structure, regarding history, construction phases, materials behavior, structural analysis, and other elements. Therefore, understanding earthen built heritage allows to recognize and keep their historical and cultural value, providing protection, conservation and, eventually, further repair or renovation. Fortunately, the First International Conference on the Conservation of Earthen Architecture in 1972 was able to promote a new level of development into earthen architecture conservation (Martínez, 2015).

During the last years, new researches about earth material have been promoted in different regions. In France, for example, a national research project launched in 2013, PRIMATERRE, aims to guide the implementation of primal materials, such as rammed earth, in sustainable constructions, providing means to measure, recognize and guarantee the materials performance (Morel, 2013). In Portugal, Martínez (2015) developed a complete work about preservation and repair of rammed earth constructions, while Librici (2016) evaluated the seismic performance of vernacular rammed earth constructions. In Czech Republic, several researches about rammed earth have been developed during the last years. Some of them focus on the mechanical properties of different clays (Otcovská and Padevĕt, 2016, 2017; Žabičková, Otcovská and Padevĕt, 2016), others studied the water absorption by clays (Mužíková, Otcovská and Padevĕt, 2017; Otcovská, Mužíková and Padevĕt, 2017).

Concerning the complexity of the material, Morel *et al.* (2001, p. 1121) pointed out that 'the general suitability of soil composition for construction is not readily standardized because of its inherent natural variability'. That means, the heterogeneity of earth has fully compromised the development of this non-standardized technique. However, during the past years, new researches established in different institutions over the world have contributed to sustain the practice of earthen constructions. This group of studies works with a common objective to create more economical and sustainable characteristics in the building construction environment, improving the quality of life in society (Guerrero Baca, 2006).

In fact, modern interest in earth as building material has increased since the end of the 20th century, mainly due to its low embodied energy[1], i.e., low environmental impact, since the material can be locally extracted, avoiding long transportation and high industry energy (Silva *et al.*, 2012). Moreover, earth as a building material has a high hydric mass, which means it contributes to a passive humidity control, thus promoting healthy and comfortable interior ambient (Allinson and Hall, 2010). Good thermal performance, good noise insulation, fire-resistant property and simple building process are some of the main advantages experienced by using earth material on constructions (Silva *et al.*, 2012).

On the other hand, the lack of regulation and standardized design codes to guide the use of earthen materials characterizes the main disadvantage for their use on building constructions. Other disadvantages are: low mechanical properties such as low strength and brittle failure behavior; high seismic vulnerability; problems with dry shrinkage phenomena, which results in cracking, diminishing the material strength; low water resistance; and a higher maintenance demanding when compared to other materials, such as concrete or stone (Silva *et al.*, 2012). Clearly, there is still a need to better understand the behavior of rammed earth material, which will help to reduce these limits.

1.1.2 Understanding the basis of rammed earth technique

This work emphasizes the behavior of rammed earth material by experimentally testing rammed earth cylinders. The term "rammed earth" can refers to the material (soil mixture of sand, gravel, silt and clay) or to the construction technique (Jaquin *et al.*, 2009). The technique of building rammed earth walls consists in compacting into a wooden or metal formwork layers of earth soil, which contains enough fraction of clay and no organic component. Normally, the layers are about 10 cm to 20 cm thick and each layer is rammed with a manual or pneumatic rammer. Compaction is performed on earth with the so called optimum moisture content. It is considered a dry method since this water content during compaction usually varies from 9 to 12%, while a paste (wet method) has about 25% (Bui *et al.*, 2008). Figure 1.1 illustrates the fabrication steps of rammed earth wallettes (small sizes) for experimental tests.
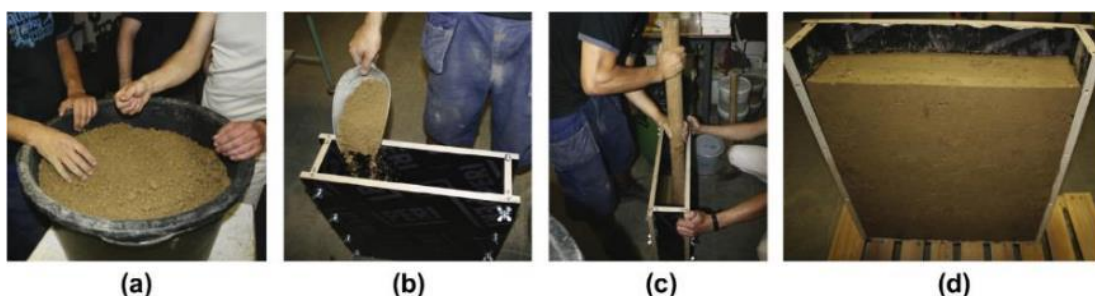
Figure 1.1 – Fabrication process steps of rammed earth wallettes by (a) check the moisture content, (b) fill into the formwork with earth, (c) compact the respective layer, and (d) remove the formwork after all layers were filled in and compacted (Miccoli, Müller and Fontana, 2014)

---

[1] Embodied energy is defined as the sum of all energy required directly and indirectly to produce any good or service (Costanza, 1979). In case of rammed earth, Morel *et al.* (2001) included in their analysis the economic and ecological conditions, as if these parameters were incorporated in rammed earth product itself.

The traditional method, referred to "unstabilised rammed earth", is that applied with the natural binder phenomena provided by clay particles. By adding industrialized binders (cement, hydraulic or calcium lime) to the clay, the so called "stabilised rammed earth" experiences some improvements, such as increase of compressive strength and higher durability respect to water. Nevertheless, it is important to understand that the use of binder other than the natural clay infers neglecting the sustainable advantages of traditional (unstabilised) rammed earth. Stabilizers increase constructions costs, in some regions their availability is reduced or even inexistent, and they have a high environmental impact in the demolition phase (Bui *et al.*, 2008). Furthermore, stabilised rammed earth loses its re-usable characteristics after breaking and it will need a further process to crush it. It is uncertain, though, that such a material could be processed again at the same way that unstabilised rammed earth. Hence, the emphasis in this work is given to the unstabilised rammed earth. Unless mentioned differently, the technique here discussed will always be referred to unstabilised rammed earth.

As an unbaked earthen construction, rammed earth technique is mainly identified by its environmental benefits. Morel *et al.* (2001) evaluate the energy consumption of houses built with local materials. The rammed earth house object from their study required about 240% less energy when compared to the traditional one built with concrete. In fact, the sustainable characteristic of rammed earth covers different aspects. Despite both rammed earth and concrete houses presented a similar construction time, the earthen one was built with materials requiring less energy consumption, it presented lower transport impact on the environment and better thermal insulation, which contributes to the inner comfort.

Rammed earth technique has been applied over time in many ancient constructions from different regions of the world, including Europe, North Africa, North and South America, Australia, and Asia (Maniatidis and Walker, 2003). In France, the existence of about 2.4 million earthen houses in 1987 (Michel and Poudru, 1987[2]; cited in Bui *et al.*, 2008) sustained the concern to provide them a proper maintenance. In Japan, a rammed earth wall, built approximately 1300 years ago, surrounds Horyuji Temple, the Japan's first World Cultural Heritage site (Hall and Djerbib, 2004). In Spain, a great example is the Alhambra of Granada, where several historical rammed-earth buildings still survive (Sebastián and Cultrone, 2010). Another successful examples of such a heritage can be found in Moravia, in the east of Czech Republic, where many rammed earth constructions contribute to the local building stock, mainly because materials other than soil were difficult to extract (Syrová and Syrový, 2012).

1.1.3 The importance of moisture content control on rammed earth material behavior

Rammed earth materials are constituted mainly by sandy-clayey components, though water plays an important role on the structural behavior. The clay particles act as a bond in the presence of a certain amount of water. Clay eases the existence of a very narrow porous network where capillary forces can act providing cohesion between particles. To optimize the compaction process, the soil needs to be

---

[2] Michel, P. and Poudru, F. (1987) 'Le patrimoine construit en terre en France métropolitaine', *Le patrimoine européen construit en terre et sa réhabilitation – Colloque international ENTPE*, pp. 529-551.

used in its optimum moisture content before being compacted inside the formwork. After compaction, the rammed earth element is left to dry for some weeks, providing the definitive mechanical strength of the structure (Q. B. Bui *et al.*, 2014).

The control of moisture content on rammed earth is very important for the mechanical behavior during and after the manufacture process. In fact, water is always a concern in any earth material. The increase of moisture content after construction destroys the capillary forces and can lead to a dramatic decrease of the shear resistance of the material. For example, damage on external rammed earth walls is very common, since they are frequently subjected to large changes in humidity and wetting from rain (Jaquin *et al.*, 2009).

1.2   Description of the problem

Within the framework of the national French research project PRIMATERRE, a hierarchical elasto-plastic model (CJS-RE) was especially developed for rammed earth at the *Laboratoire de Tribologie et Dynamique des Systèmes* (LTDS), University of Lyon, in France. So far, the use of this model was undergone under some statements for there is no existing comprehensive mechanical study of the behavior of rammed earth including a variety of stress paths, able to warranty a correct identification of all the model parameters. The considered statements are based on experimental results obtained on concrete for which a vast literature is available. This approach was justified by analogies of behaviour existing between rammed earth and concrete which are both quasi-brittle materials. This work aims to provide new information and data by means of tests performed according to different stress paths in order to provide a proper background for the CJS-RE validation.

Moreover, the mechanical resistance of rammed earth elements only develops over time when a great amount of water has left the material due to evaporation. At any moment in the building lifetime, the capillary tensile forces within the pores can be destroyed if the water content accidentally increases (rain, capillary rise within the walls), which can lead the structure to failure. Thus, a greater understanding is needed about the quantitative evolution of the mechanical properties due to a variation of the water content. This can help, for example, to better estimate the vulnerability of earthen walls to unexpected capillary effect due to migration of water from the foundations.

1.3   Objectives

In this work, a first objective is to bridge the gap in the similarities between rammed earth and concrete by performing unconfined but also confined compression and extension tests, as to Brazilian tests, in order to identify the whole set of model parameters involved in the constitutive model CJS-RE. In a second stage, the aim is to estimate how some main model parameters of CJS-RE evolve with the change of water content in the rammed earth material.

The full work comprises eight chapters. This first chapter developed the context where rammed earth is inserted and exposed the main objectives of this study. Through the following chapters, rammed earth material and technique are broadly discussed and an experimental campaign is carried out to achieve the proposed objectives.

Chapter 2 is dedicated to the understanding of rammed earth behavior, providing its main properties and characteristics. This literature review is assessed with the background on different experimental works developed during the past years.

Chapter 3 approaches the constitutive modelling for rammed earth. Special attention is given to CJS-RE, an elasto-plastic constitutive law which was specially developed for rammed earth material at the *Laboratoire de Tribologie et Dynamique des Systèmes* (LTDS), in France. The main equations of two hierarchical levels from this model are indicated.

Chapter 4 addresses the methodology developed in this work and presents the properties of soil material including physical properties of samples. Main manufacturing and testing procedures are also included.

Chapter 5 provides the results of the experimental work carried out in this study. First, compression and extensions tests allowed the model parameters of CSJ-RE to be identified including those involved in the plastic shear failure surface. After, results of Brazilian tests identified the model parameter related to the tensile failure surface, which is the second plastic failure surface of CJS-RE model

Chapter 6 focuses on the study of the stress-strain relationship for rammed earth, based on the experimental tests which were carried out. The Young's modulus and the isotropic plastic hardening parameter were identified.

Chapter 7 compares the experimental results of plastic failure surfaces from the two different water contents suggested in this work. The modelling parameters from CJS-RE constitutive law are presented for both studied water contents in order to identify a pattern on the changes of the mechanical behavior of rammed earth.

Finally, chapter 8 gives the conclusions of this work and some prospects for further investigation.

2. BEHAVIOUR OF RAMMED EARTH

Here, the main properties of rammed earth material are presented, including the grading of soil, clay mineralogical composition, plasticity, dry density, optimum moisture content, suction, and anisotropy. The mechanical properties firstly approached are the elastic parameters, the compressive strength, the tensile strength, the shear strength, the flexural (bending) strength, and the durability.

2.1 Properties of soil for rammed earth material

Soils result from several alterations of rocks developed through many centuries and promoted by different actions: mechanical, physical, chemical and biological (Martínez, 2015). Compacted soils used in rammed earth constructions have their specific properties, which are discussed next.

2.1.1 Grading of soil

In soil mechanics, the ISO 14688-1 (International Organization for Standardization, 2002) defines grading as the measurement of the particle size distribution by mass. Information of particle size distribution (PSD) has become a common practice to understand the behavior of soil for rammed earth (Maniatidis and Walker, 2003). Dry sieving methods are the most common tests to determine the grading of a soil. Regarding the identification of the fine fraction, the sedimentation tests are widely applied (Martínez, 2015).

Soils for engineering use, and so for rammed earth, are classified according to the size proportion of their main elements: gravel, sand, silt and clay (Maniatidis and Walker, 2003). Among different classifications, the one provided by ISO 14688-1 (International Organization for Standardization, 2002) considers the following limits for:

a) gravel: 2 mm to 63 mm;

b) sand: 0.063 mm (63 µm) to 2 mm;

c) silt: 0.002 mm (2 µm) to 0.063 mm (63 µm);

d) clay: less than 0.002 mm (2 µm);

For applications of rammed earth on small samples, different authors limit the use of gravel size up to 10 mm until 20 mm, because high-size gravels can greatly change the mechanical behavior of small rammed earth specimens. Hall and Djerbib (2004), for example, followed the BS 1377-4 (British Standard, 2002) procedure for compaction tests and opted for gravels with maximum 20 mm size, from which the PSD curves are verified in Figure 2.1. This is an example graph, where the vertical axis shows the cumulative weight of particles passing by the respective sieves and the horizontal axis indicates the grain sizes of particles in a logarithmic scale (Martínez, 2015).
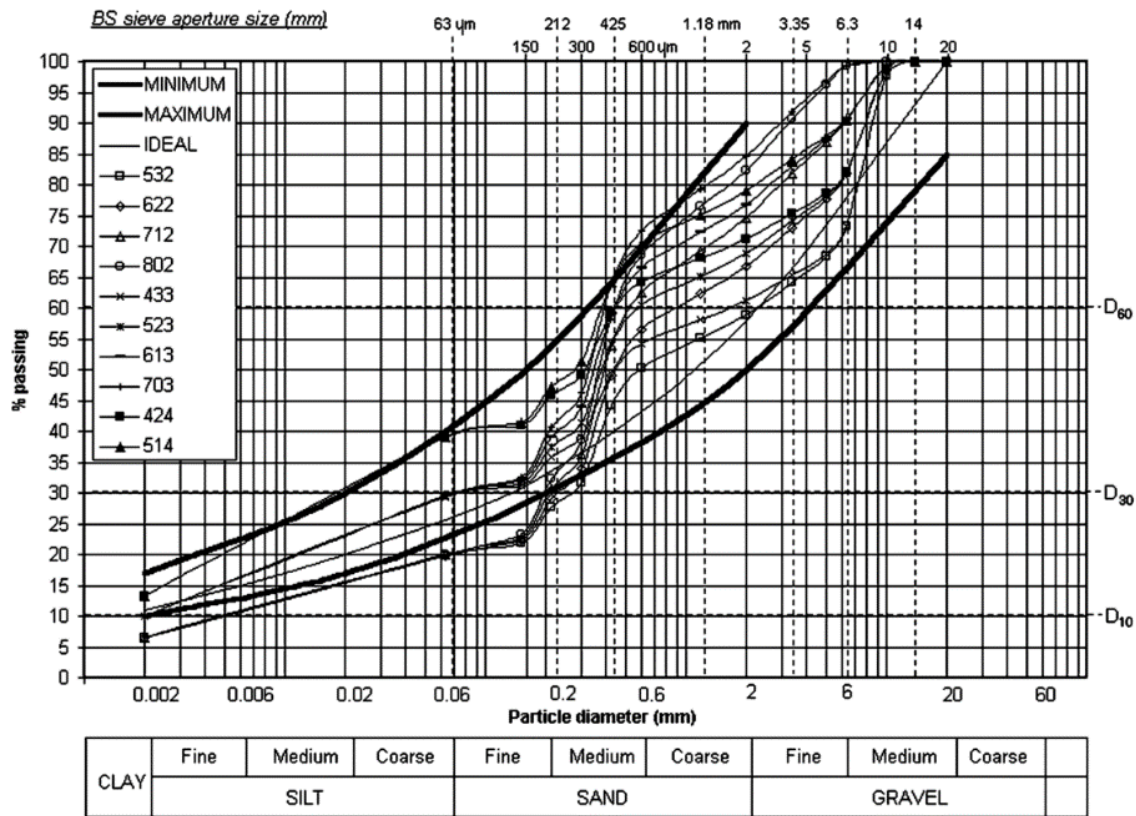
Figure 2.1 – Curves of PSD for different soils (Hall and Djerbib, 2004)

The number of voids influences the mechanical properties of soil; when the void ratio is low, the contact between soil particles is higher. Thus, smaller void ratio provides higher mechanical strength and weathering resistance (Maniatidis and Walker, 2003). This reflects the importance of providing a proper compaction work during the execution of rammed earth components (wall, column, etc.).

A soil with no voids is assumed as the one with ideal distribution, which is an impossible condition on natural soils, i.e., voids will always exist (Maniatidis and Walker, 2003). Void ratio and particle size distribution will contribute to define the mechanical behavior of the earth material. The cohesive forces observed inside the voids of a soil act differently according to the PSD and the type of soil. For example, cohesion in a sandy soil is primarily provided by capillary forces between particles in a pore network that cannot allow the development of strong forces. In a clayey soil, though, cohesion is provided not only by capillary forces between particles in a very thin pore network but also by attraction forces of clay particles (Q. B. Bui *et al.*, 2014).

Different types of tests can be applied to characterize the soil and provide its suitability for the use in rammed earth technique. Silva *et al.* (2014), for example, opted to use expeditious tests (sedimentation test, ribbon test, drop test and dry strength test) and laboratory tests (PSD analysis, consistency limits and standard Proctor).

More researches about suitable grading for rammed earth technique are certainly a need. Nevertheless, different sources agree on the limits (minimum and maximum percentages) of the main soil elements that should be used, as pointed by Maniatidis and Walker (2003) and described in Table 2.1.

Table 2.1: Lower and upper limits for PSD of rammed earth soils (Maniatidis and Walker, 2003)

element	Minimum limit	Maximum limit
combined clay and silt	20% - 25%	30% - 35%
sand	50% - 55%	70% - 75%

Champiré *et al.* (2016) prevent that suitability of a certain type of soil for rammed earth construction is not a singular function of the PSD, but might be related to other factors. For rammed earth soils, Maniatidis and Walker (2008) add that an excessive clay content can promote significant shrinkage on drying. They suggest that a clay fraction between 8% and 15% is usually suitable for most rammed earth soils, but the proper amount depends on the clay plasticity. On the other hand, Walker *et al.*(2005[3]; cited in T. T. Bui *et al.*, 2014) point out that clay fraction higher than 10% is not suitable for rammed earth manufacture. Clearly, suitability of clay fraction also requires more studies.

2.1.2 Clay mineralogical composition

In rammed earth material, clay plays – together with water – an important role as a binder. Both clay components and water content assure the material strength and shrinkage behavior (Otcovská and Padevět, 2016).

Clay minerals (phyllosilicates) are the smallest grain size portion of earth. The group of phyllosilicate (sheet silicates) minerals is characterized by a platy, sheet-like, crystal structure. Between layers of each mineral, there is a cohesive force primarily electrostatic, which is then amplified by Van der Walls attraction. The number of different crystal structures of clay minerals is very extended, and they are identified according to the number of atom substitutions within the crystal structure (Verhoef, 1992). Thus, clay minerals basically differ by their property of absorbing cations and water into the clay structure (Valde, 2008). Among a considerable classification of minerals compiled by Valde (2008), some examples are:

> a) montmorillonite: an aluminous mineral, a swelling clay (expansive) mostly occupied by silicon (Si) within its layers;
>
> b) kaolinite: clay with no charge (not expansive), which contains only aluminum (Al);
>
> c) illite: a high charge aluminous mineral, which contains also other substitutive elements. It is the most common mica-like (i.e. non-true mica structure) mineral found in earthen materials.

---

[3] Walker, P., Keable, R., Martin, J. and Maniatidis, V. 2005. '*Rammed earth: design and construction guidelines'*, BRE Bookshop.

Champiré *et al.* (2016) support the conclusion that the activity of clays may have more effect on the mechanical behavior of rammed earth than the amount of clays, as long as the clay content is enough to ensure the binding phenomena to take place. As described by Q. B. Bui *et al.* (2014), the mineralogical composition of clays can be identified by the clay activity index. This index can be calculated from the methylene blue value (MetBV) by carrying out specific methylene blue tests just on the clay fraction, removing bigger particles.

Methylene blue test is suitable for soils with certain rocky materials and it is comprehensively described by the French standard NF P 94-068 (Norme Française, 1993). For materials with high clay content, there is also another way to obtain the clay minerals composition: determining the Atterberg's limits (liquid limit, plastic limit and shrinkage limit). The Atterberg's limit test is generally recommended to soils with a percentage of fines (80 µm) greater than 35% (Sétra, 2007). X-ray powder diffraction is also a common method to identify mineralogical properties of earthen materials (Miccoli, Müller and Fontana, 2014).

The methylene blue test consists in preparing a soil portion mixed with distillate water and measuring the quantity of methylene blue (MetB) which can be adsorbed on this soil. This quantity is directly proportional to the fraction of soil particles within 0 to 50mm sizes. The dosage is carried out by adding successive different quantities of MetB, keeping the soil-water suspension shaking. After each addition, the adsorption control is taken by removing a drop from the suspension and depositing it on a filter paper. The first drops result on a stain with fixed MetB in the middle, and surrounded by colorless wet zone (negative test). The objective is to repeat the test until finding the maximum adsorption, which is indicated by a persistent light blue halo that appears at the periphery of the MetB stain (positive test) (Norme Française, 1993). Figure 2.2 illustrates both negative and positive tests.
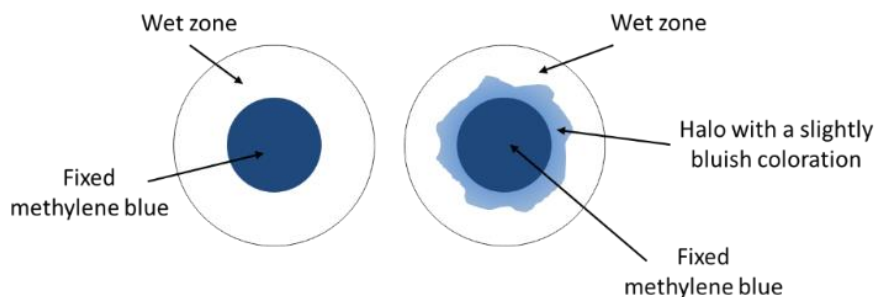
**Figure 2.2 – Negative (left) and positive (right) tests for the
maximum methylene blue adsorption on the soil**

Hence, the MetBV can provide suitable knowledge regarding the sensibility to water of the clay minerals, i.e., the capacity of the clay particles of a soil to store water in their pores (Table 2.2). Furthermore, the MetBV can be related to many geotechnical properties of soil (swelling and shrinkage, shear strength, etc.) (Verhoef, 1992). Together with Atterberg's limits and others specific tests of a soil, methylene blue tests can positively help to understand the mineralogical composition of the material.

Table 2.2: Classification of soils regarding their sensitivity to water

MetBV	Description of clay particles activity of a soil
0.1	soil is insensitive to water
0.2	soil starts to present some sensitivity to water
1.5	it distinguishes sand-silty soils from sand-clayey soils
2.5	it distinguishes silty soils with low plasticity from those with medium plasticity
6.0	it distinguishes silty soils from clayey soils
8.0	it distinguishes clayey soils from high-clayey soils

Q. B. Bui *et al.* (2014) carried out methylene blue tests in their experimental work, which helped to understand the soil's sensitivity to water. Table 2.3 indicates the minerals identified in each soil.

Table 2.3: Clay's mineralogical composition of the soils used (Q. B. Bui *et al.*, 2014)

soil	Clay content (by weight) (%)	Kaolinite (%)	Illite (%)	Montmorillonite (%)
Soil A	5	35	0	65
Soil B – stabilised soil	4	15	0	85
Soil C	9	0	65	35
Soil D	10	18	18	64
Soil E – stabilised soil	10	18	0	82

After analyzing the results from unconfined compressive strength tests on the five soil samples, Q. B. Bui *et al.* (2014) observed that the compressive strength of soils B and E – despite the fact they were stabilised with hydraulic lime – were lower than the unstabilised samples, when keeping the same moisture content. The authors pointed out that the high fraction of expansive Montmorillonite (85% for soil B and 82% for soil E, from the total clay) may have played an unfavorable role for compressive strength. This is just one example on how important is to identify the clay's mineralogical composition.

2.1.3   Soil plasticity

Within earth behavior study, plasticity is the state reached by the soil from which irreversible deformations occur with the increase of loading (Maniatidis and Walker, 2003). Together with the texture, plasticity is an important property to be measured on earth material, with the aim to decide about its suitability (Silva *et al.*, 2012). Soil plasticity is characterized by its plasticity index. This parameter

represents the water content within a soil required to transform its state from plastic to liquid (Maniatidis and Walker, 2003).

In practice, the value of the plasticity index comes from the numerical difference between liquid and plastic limits (the Atterberg's limits). A higher value of the plasticity index indicates the soil is composed by greater clay content and/or active clay minerals. Consequently, shrinkage is most probable to occur when the earth dries (Maniatidis and Walker, 2003).

Regarding recommended limits, Silva *et al.* (2012) advise is preferable to work with soils of liquid limit between 25% and 50% and plastic limit between 10% and 25%. The authors present an envelope curve for these recommended plasticity index (PI) values, which is reproduced in Figure 2.3.
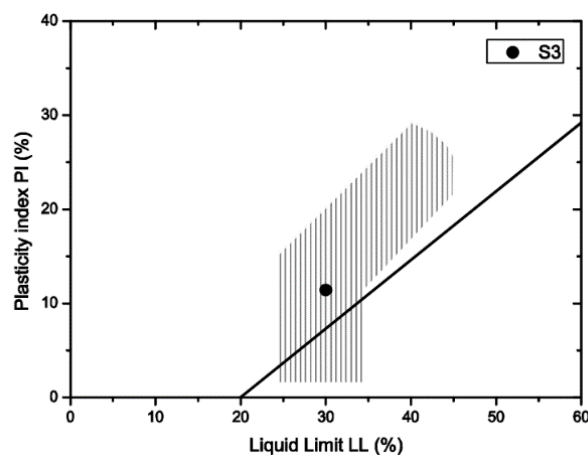
**Figure 2.3 – Envelope for the plasticity properties of soils
(Houben and Guillaud, 2008[4]; cited in Silva *et al.*, 2012)**

In this example, the black dot within the envelope curve represents the plasticity index for the soil S3 used on Silva *et al.* (2012) work. For this soil, the liquid limit (LL=30%) and the plastic limit (PL=19%) resulted a plasticity index (PI) of 11%, which fits inside the envelope. Silva *et al.* (2012) affirm soils S1 and S2 had low clay content (6% and 5%, respectively), thus, they were non-plastic soils and difficult to manipulate and shape for the dropping ball and ribbon tests (to evaluate compaction, texture and binding force).

2.1.4 Dry density (bulk density) and optimum moisture content (OMC)

The proper assumption for the value of the dry density of rammed earth is not only important for better representing the material, but also because it will impact on the element design by means of the calculation of loads on it (Maniatidis and Walker, 2003). Three main features which influence the value of dry density are: the soil type, the moisture content during compaction and the compaction effort

---

[4] Houben, H. and Guillaud, H. (2008). '*Earth Construction, A Comprehensive Guide*', CRATerre – EAG, Intermediate Technology Publication, London, UK.

(Maniatidis and Walker, 2003). The experimental scale could also interfere on the value of dry density, since two set of samples with great difference in size could be subjected to different compaction response, though, presenting two different sets of dry densities. Indeed, Bui *et al.* (2008) pointed out that in small samples the thickness of each layer is thinner when compared to in-situ element, therefore the earth is denser and more compact.

Different dry densities experimentally achieved for small specimens are summarized in Table 2.4. Based on them, the range of dry densities achieved by mechanical compaction methods can vary mostly from 1800 to 2200 kg/m^3.

Table 2.4: Dry densities results from different experimental researches – small scale tests

Reference	Dry density range/mean (kg / m³)	gravel, sand silt, clay proportion	Moisture content during compaction	Compaction method and sample size
(Hall and Djerbib, 2004)	2118 to 2145 kg/m^3 Average 2135 kg/m^3	gravel: 20% sand: 60% silt clay: 20%	8%	Standard Proctor with varying compaction energy cubes 10 cm side
(Maniatidis and Walker, 2008)	Average 1850 kg/m^3	gravel: 30% sand: 45% silt: 13% clay: 12%	12.5%	Modified Proctor cylinders 10 cm diam. x 20 cm high
(Bui *et al.*, 2008) [5]	Average 1900 kg/m^3 1980 kg/m^3 (up) 1820 kg/m^3 (low)	gravel: ~17% sand: ~47% silt: ~32% clay: ~4%	10%	Pneumatic Rammer 9.5 x 14 x 29.4 cm^3 (CEB)
(Jaquin *et al.*, 2009)	2017 to 2061 kg/m^3 [*sic*]	gravel: 25% sand: 60% silt clay: 15%	12%	Vibrating hammer cylinders 10 cm diam. x 20 cm high
(Martínez, 2015)	Maximum dry density 2100 kg/m^3	cobble: 1% gravel: 37% sand: 32% silt: 16% clay: 14%	10.1%	Standard Proctor no information about size of samples during Proctor test

For a given cohesive soil and keeping the same compaction effort, there is an optimum moisture content which will provide the maximum value for the dry density. There are three types of soil compaction tests that can be chosen to determine the maximum dry density and the optimum moisture content. Two of them are manual, the so-called Proctor compaction tests, which are more commonly used. The "standard" Proctor test is applied by a 2.5 kg rammer on a soil-sample and the "modified" one by a 4.5

---

[5] The fractions for the particles gravel, sand, silt and clay were estimated from the PSD curve available in Bui *et al.* (2008) work, and they may not correspond to the exact percentages.

kg rammer. The third type (vibrating hammer), is mainly intended for more granular soils. Additionally, other different tests could be used, regarding their specific standard guidelines (British Standard, 2002).

The compaction method needs to be applied for at least five cylindrical specimens. Then, their wet weights are recorded and the samples are left to dry (the samples should reach different moisture contents). After the drying period, a graph curve can be plotted by moisture contents versus dry densities (Figure 2.4). This resultant curve will provide the optimum moisture content, which corresponds to the maximum dry density for a given compaction effort (Maniatidis and Walker, 2003).
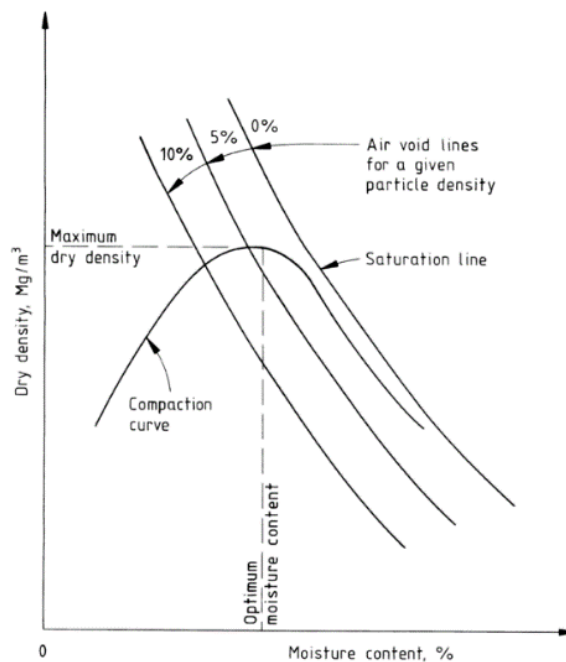
Figure 2.4 – Relationship curve between dry density and moisture content (British Standard, 2002)

When manufacturing rammed earth specimens for the compaction test, many authors consider an average dry density for the entire sample. This is an acceptable simplification, however, the compaction technique itself explains the existence of a gradient of densities from top to bottom within each layer. Because of the direct contact with the rammer, the upper portion of a layer is denser than the lower one (Bui *et al.*, 2008).

Bui *et al.* (2008) and Bui and Morel (2009) showed in their works a first approach to take into consideration the gradient of densities within each layer, which they called "homogenization process". They assumed that two consecutive rammed earth layers present perfect adhesion between them, and that all layers are identical with same thickness. Thus, each layer has two different homogeneous portions: the upper and the lower dry density.

As described here, two soil properties are well-known after the Proctor compaction test: the maximum dry density and the optimum moisture content. The initial moisture content before manufacturing a

rammed earth element is then often associated as being that optimal moisture content. However, Schoreder (2011) developed an experimental work for rammed earth material to study the influence of initial moisture content and drying period to the final strength of rammed earth material. As a conclusion, the author affirms that water content during rammed earth compaction should be chose 10% higher than the optimal moisture content obtained by the Proctor compaction test. Further research is suggested, though, in order to consider also the compaction effort as a parameter which influences the process of moisture transfer and change in strength during drying period.

2.1.5 Suction

As described before, rammed earth material consists of compacting earth through several layers and then left it to dry. Thus, the material become unsaturated, i.e., the soil particles will be surrounded by air in addition to the remaining water. There will always exist an amount of water even for oven-dry soils, because zero water content is an ideal condition (Jaquin *et al.*, 2009).

Suction is defined as a 'fundamental physical property of unsaturated soils describing the potential with which a given soil at given water content adsorbs and retains pore water' (Likos and Lu, 2003, p. 1). The total soil suction is in fact a sum of two components: a matric component and an osmotic component. The matric suction is associated with capillary between particles and with the mechanism of particle surface hydration. The osmotic suction is a function of dissolved solutes in the pore water. Typically, moisture-suction characteristics curves are used to describe the relation between moisture content and suction. These curves are represented either by the matric or total suction (Likos and Lu, 2003; Jaquin *et al.*, 2009).

Jaquin *et al.* (2009) and Q. B. Bui *et al.* (2014) studied and confirmed that suction is a source of strength in unstabilised rammed earth, including the increase of shear strength. Q. B. Bui *et al.* (2014) proved by several tests on different soils that compressive strength is linearly correlated with increase of suction. In soils composed mostly by sand (low clayey soil), two spherical particles of sand with a rough surface create a bridge of attractive forces due to capillary condensation. The phenomenon consists in four phases:

     a) asperity phase: after two asperities get in contact with each other, condensation starts and the cohesive force increases non-linearly with the amount of moisture.

     b) roughness phase: the force continues increasing with the amount of moisture, but now linearly due to the lateral spreading of the liquid surrounding several asperity couples;

     c) classical phase: different from the second phase, the meniscus now is no longer sensitive to the roughness of asperities, and so the cohesive force does not depend to the amount of moisture anymore (this indicates the attractive forces are constant on samples in dry state, i.e., with moisture content between 2% and 4%);

     d) saturation phase: while the moisture content increases, the liquid between asperities merge, and the cohesion force decreases (Q. B. Bui *et al.*, 2014).

In the case of clayey soil, there are two phenomena involved: the capillary forces between particles as described for the sandy soil, and the attraction between clay particles (plate shapes) due to Van der Waals force (as described in the section 2.1.2). Basically, in this second phenomenon, the double layers surrounding each clay particle (plate) are mutually repulsive due to their positive charger. When the thickness of the double layer is high [*sic*] (high concentration and high valence of the cations between layers), the attraction prevails, plates attract, so cohesion occurs. Or else, when the thickness is low (as a consequence of increase of water), the particles push one to the others, so cohesion is lost (Q. B. Bui *et al.*, 2014).

A simplified method to quantify the suction inside rammed earth samples was presented by Q. B. Bui *et al.* (2014), based on Likos and Lu (2003). They defined suction as the difference between the pore air pressure and the pore water pressure. Suction is also linked to the relative humidity (RH) of the pore air through the following Kelvin's equation:

$$s = u_a - u_w = -\frac{R \cdot T}{g \cdot w_v} \ln\left(\frac{P}{P_0}\right) = -\frac{R \cdot T}{g \cdot w_v} \ln(RH) \tag{1}$$

where u_a is the pore air pressure (KPa); u_w the pore water pressure (KPa); R is the universal gas constant (8.31432 J mol^{-1} K^{-1}); T is the absolute temperature (K); g is the acceleration due to gravity (g = 9.81 m/s²); w_v is the molecular mass of water vapor (18.016 kg/kmol); RH is the relative humidity (%), defined by the ratio of partial vapor pressure P in the considered atmosphere and the saturation pressure of pure water vapor P_0 which depends on the temperature (Likos and Lu, 2003; Q. B. Bui *et al.*, 2014). The equation indicates that drying of the wall will continue until equality of the pore air humidity and the humidity of surrounding air (Jaquin *et al.*, 2009; Q. B. Bui *et al.*, 2014).

In fact, the increase of apparent cohesion is limited, expected to peak at certain point between "zero-water" content and saturation state. The remaining adsorbed water on clay particles will still be available to generate suction even in the "zero-water" state (Jaquin *et al.*, 2009). By dealing with a simple method of measuring suction using filter paper, Q. B. Bui *et al.* (2014) studied the limit of moisture content that maintain the mechanical strength. They verified that the variation of suction is slight for the samples in dry state (moisture content less than 4%), but it highly decreases with increase of moisture content (Q. B. Bui *et al.*, 2014), as observed in Figure 2.5. The authors also showed that a slight increase in the moisture content of dry rammed-earth wall does not cause a sudden drop in strength.

By means of six unconfined compression tests at constant water, Jaquin *et al.* (2009) measured suction on each sample prior to shearing in a triaxial test. All the samples had the same compaction water content (12%), but they differed on the target water content after air-drying. The initial water content is linked to both suction and strength during shear test of the six samples. The authors observed a brittle behavior in the driest soil specimens, whereas the wetter samples showed a greater ductility. Figure 2.6 indicates that suction reduces following axial strain in unsaturated soils. In fact, suction dropped during

the test of samples at low initial water content (5.5%, 7.1%, and 8.3%), whereas in those at high initial water content (9.4% and 10.2%) suction increased.
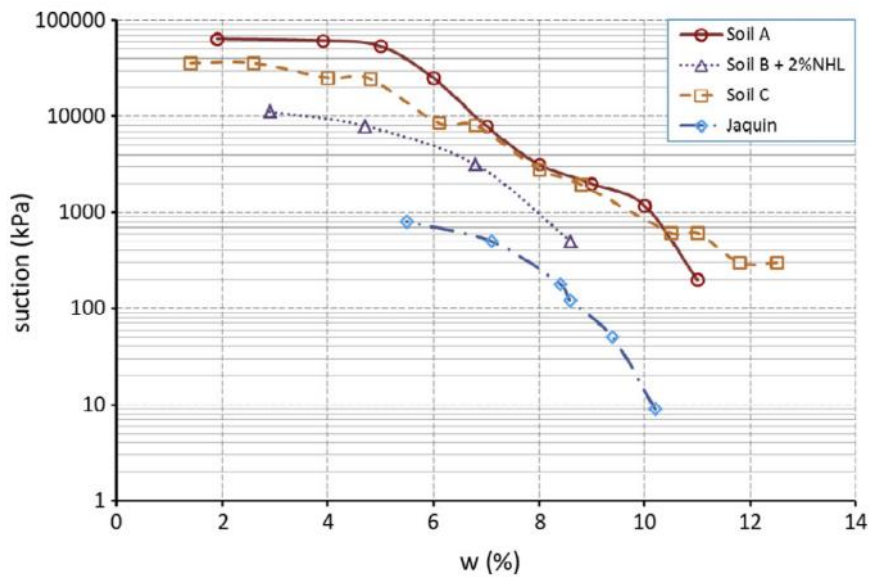
Figure 2.5 – Variation of suction (s) following samples' moisture content (w)
(Q. B. Bui *et al.*, 2014)
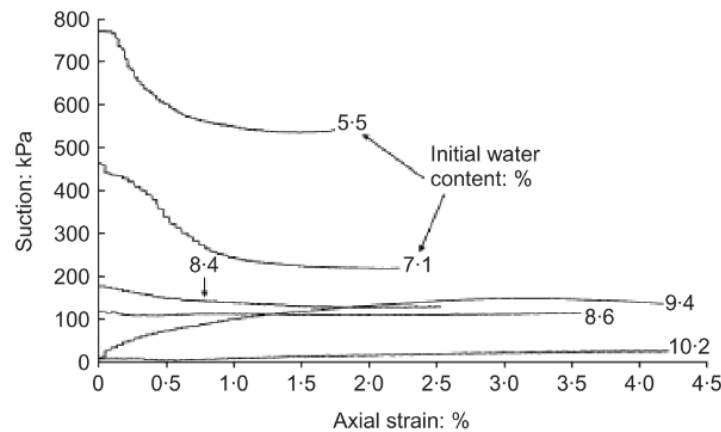
Figure 2.6 – Plots of suction against axial strain during triaxial shearing tests
(Jaquin *et al.*, 2009)

Another interesting behavior is that suction may reduce even more when volumetric dilatation occurs. This is explained by the fact that suction is a response of intra-aggregate (within particles) compression, whereas the dilatant volumetric behavior is influenced by inter-aggregate shearing, i.e., shear between aggregates (Jaquin *et al.*, 2009).

In actual situations, in-situ rammed earth walls should present the same behavior as the laboratory soil samples. Being exposed to atmosphere, soil materials of rammed earth walls can dry down to a great low degree of saturation. In a suitable climate, the expectation is a development of very large suctions in the remaining pore water from these walls, which led to increase of strength over time (Jaquin *et al.*, 2009).

2.2 Mechanical properties of rammed earth

Previously, it was mentioned that suction is the main mechanism which is responsible for the strength on rammed earth material. In addition to suction, other features promote the increase of strength, such as the densification and possible particle interlock promoted by the ramming process during the layers' construction (Jaquin *et al.*, 2009). In the same way, some materials properties of rammed earth are difficult to predict, and specific values of the mechanical strengths (compression, tensile, shear, etc.) are impossible to be given without carrying out any prior testing (Maniatidis and Walker, 2003).

Bui and Morel (2009) conclude that rammed earth material is isotropic, and though some mechanical properties (compressive strength, elasticity moduli, and failure moduli) are similar in both directions perpendicular and parallel to the layers, as long as the layers remains adherent to each other.

This section focuses on the study of the main mechanical properties of rammed earth elements: elastic parameters, strength in compression, in tension, in shear and in bending, and finally durability. But first, it is positive to present a review of different scales for experimental works.

2.2.1 Scales of samples analysis

Experimental works are necessary regarding the study of mechanical performance of different materials. Rammed earth behavior can be evaluated by many types of scale, i.e., groups of specimens with different sizes. For example, Bui et al. (2008) worked with three different scales for their analysis: in-situ walls, representative elementary volume (REV), and micro-mechanical scale of equivalent compressed earth blocks (CEBs). Similarly, Maniatidis and Walker (2008) applied tests on three different experimental phases: full-size columns, large scale prisms, and small scale cylinders.

The main difficulties when proposing laboratory studies is to make representative samples. Thus, in-situ measurements could be used to validate laboratory results. The unique characteristic of REV scale is to ensure a faithful representation of in-situ material. The micro scale composed by CEBs can be used to facilitate the laboratory test procedure, and the results are very close to REV scale (Bui *et al.*, 2008). Important issues concerning the manufacture of REVs are well described by Bui *et al.* (2008):

> a) rammed earth is a manual construction technique, which means the compaction energy depends on the experience and practice of each mason. When using the Proctor compression test, it is important to correlate both compaction energies of sample and in-situ rammed earth element;

  b) the material grain size should be small enough so the test could be considered homogeneous at the representative scale. Plus, as already stated before, a density gradient is observed in each layer of the sample. The upper part of each layer in contact with the rammer is denser than the lower part;

  c) the size of the samples should be carefully defined, because they need to be sufficiently big to represent in-situ material. Moreover, the slenderness ratio requires special attention, since samples with low value (ratio less than 2), do not give direct results. In such cases, a correction factor should be applied, e.g., the factor 0.7 used by Hall and Djerbib (2004) for their compressive strength results, given that their samples had a slenderness ratio of 1.

2.2.2 Compressive strength and elastic parameters

There are different ways of measuring the compressive strength and the elastic parameters of rammed earth material, which can be done by field tests or laboratory tests. The laboratory compression tests are the most common and they provide better accuracy. The information recorded during compression allows to build the stress-strain relationship curves and to obtain, for example, the Young's modulus (Maniatidis and Walker, 2003).

In fact, during experimental compression tests, loading on rammed earth samples can be done at two main modes: at constant speed until failure (classical unconfined compression test) or by successive unloading-reloading cycles with different increases of stress level. The first (classical test) is generally used to obtain the compressive strength (f_c), while the second (one-way loading cycles) allows determining the Hooke's law elastic parameters (Champiré *et al.*, 2016).

Compression strength and elastic parameters can vary depending on the sample geometry, type of earth used and test conditions (Champiré *et al.*, 2016). In this sense, a wide variability of rammed earth mechanical properties is found on literature. Values for the compressive strength obtained by laboratory tests can vary from 0.5 MPa to 4.00 MPa (Miccoli, Müller and Fontana, 2014; Librici, 2016). On the other hand, values for the characteristic unconfined compressive strength recommended by some codes are more strict and they mostly vary from 0.4 to 0.7 MPa (Maniatidis and Walker, 2003).

Values for the Young's modulus are commonly found in a range between 60 MPa and 1000 MPa (Miccoli, Müller and Fontana, 2014; Librici, 2016). The Poisson's ratio is another important parameter, which depends on the water content (Champiré *et al.*, 2016). On Q. B. *et al.* (2014) experiments, Poisson's ratio values were about 0.2 for rammed earth samples with moisture content in dry state (1-2%), and about 0.37 for the wet ones (11-13%).

Regarding the anisotropy study from Bui and Morel (2009) experiments, the values of compressive strength parallel to layers showed just a small difference (10% higher) from those of compressive strength perpendicular to layers. Under certain low level of preloading, the Young's modulus measured parallel to the layers was about 25% higher than the one measured in the perpendicular direction. This difference was insignificant for a higher preload on those samples (0.4 MPa).

In Bui *et al.* (2008) experiments at the REV scale, the authors performed for each sample several cycles at different load levels (corresponding to stress levels of 0.06 MPa, 0.12 MPa, 0.22 MPa, and 0.4 MPa for one specific sample). The idea was to verify the existence of an elasticity of the material and, if so, determine its modulus. Figure 2.7 gives an example of a strain-stress curve resulted from an unconfined compression test applied on the rammed earth sample n°. 1. On the left graph of Figure 2.7, each stress level (0.06 MPa, 0.12 MPa, and 0.22 MPa) corresponds to a load level. For each load level, three cycles were performed to verify the modulus of elasticity. A zoom from three cycles of the third load level is given on the right graph of Figure 2.7. The purpose of several load levels was to identify the changes in elastic modulus, especially at the non-linear portion of the curve due to roughness of the upper and lower surfaces of the sample (Bui *et al.*, 2008).

In some materials, such as steel, the conventional elastic modulus is determined in the linear portion of the strain-stress curve, called in Bui *et al.* (2008) study as $E_{tangent}$. But, in the case of rammed earth material, Bui *et al.* (2008) confirmed the inexistence of any statement about this elastic portion at the beginning of tests on rammed earth. Given a certain preload, the authors verified that the material behavior becomes almost elastic-linear for stresses under this preload. Additionally, they observed that the more this preload increased, the more the elastic modulus increased.

The complex mechanical behavior of rammed earth, which combines damaged elasticity, irreversibility, and unsaturated mechanisms, is underlined by Champiré *et al.* (2016). Regarding the compressive behavior, since suction is the main property that explains the material strength, even a small increase of water content (or increase of relative humidity) is followed by a high decrease of both compressive strength and elasticity modulus (Champiré *et al.*, 2016).
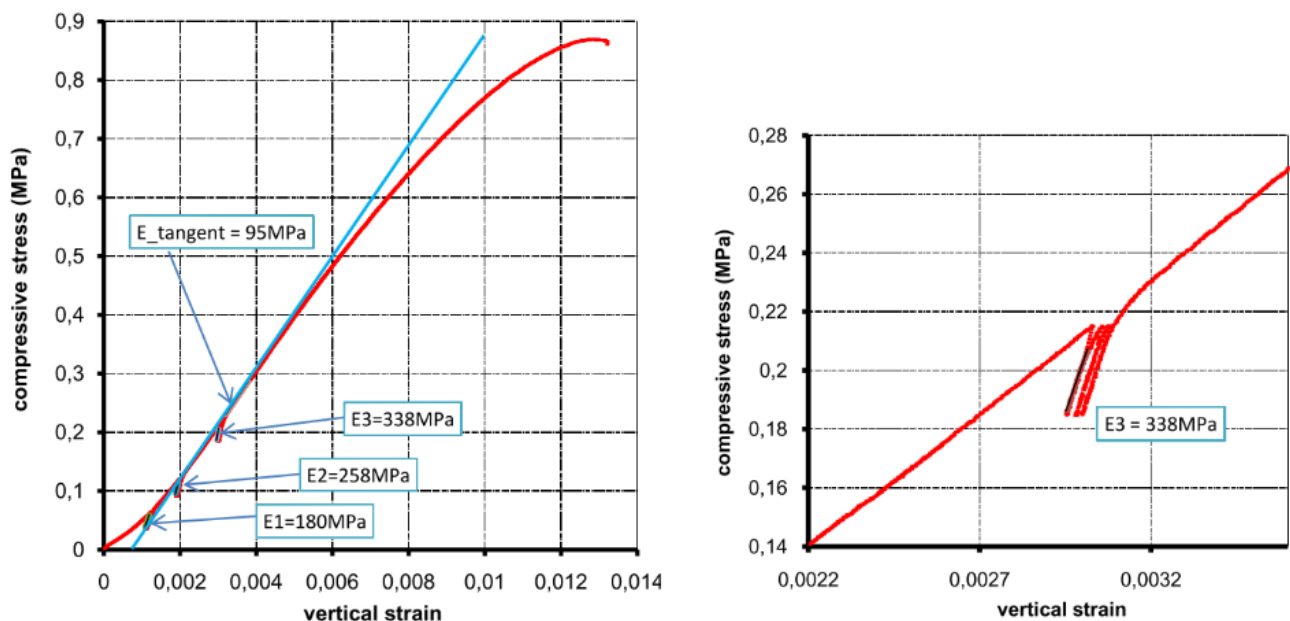
Figure 2.7 – Left: strain-stress curve of sample n°. 1 (40×40×65) cm^3.
Right: zoom of cycles at the third level (Bui *et al.*, 2008)

2.2.3   Tensile strength

Rammed earth material is very weak in tension and, for this reason, standards and guidelines recommend that rammed earth elements should not be designed for pure tension (Maniatidis and Walker, 2003). Therefore, in general, the tensile strength is assumed around zero, but there are certain cases when specific performance is required that some contribution could be considered (Librici, 2016). Araki *et al.* (2016) added that the tensile strength of rammed earth walls is an important factor to be evaluated for seismic analysis behavior.

Maniatidis and Walker (2008) provided an experimental study of rammed earth columns behavior under concentric and eccentric axial compression loading. As a conclusion, the authors observed that special attention is needed for columns under high load eccentricities, since the samples presented suppressed cracking due to material low tensile strength and confinement.

T. T. Bui *et al.* (2014) presented experimental results on tensile and shear strength of stabilised and unstabilised rammed earth. To determine the tensile strength, cylindrical specimens were manufactured for Brazilian test. To evaluate the anisotropy of rammed earth in traction, they distinguished two tensile strengths: the tensile strength within each layer and the tensile strength at the interfaces of earth layers. Surprisingly, test results showed that both tensile strength within each layer and tensile strength at interfaces between layers are similar. This fact confirmed the assumption of an isotropic material for rammed earth, as presented by Bui and Morel (2009). Furthermore, the work proposed that tensile strength can be estimated as 11% (or 10% for simplification) of the compressive strength (before applying the respective safety factors).

Araki *et al.* (2016) evaluated the tensile strength of three kinds of rammed earth material (two unstabilised and one stabilised with calcium oxide). To identify the tensile properties, they applied two types of tests for the experiments: direct tension tests (direct method) and splitting tests (indirect method). They found that the unstabilised rammed earth samples reached a range of 5.0-12.5% of the corresponding unconfined compressive strength, while the stabilised samples varied between 15-20%. The authors add that direct tensile test should be used to evaluate the tensile strength at a layer interface, since it is an important factor during the analysis of the seismic performance of a wall.

2.2.4   Shear strength

According to T. T. Bui *et al.* (2014), from Mohr-Coulomb theory it is known that shear strength is a function of cohesion (c), normal stress (σ) and friction angle (φ). Cohesion can be determined by applying the Mohr's circles for two compression tests with different confining pressures. In their work, T. T. Bui *et al.* (2014) proposed that $c = 0.14f_c$, and $\varphi = 51°$. From their results, they pointed out that, as a first proposal, shear strength should be taken as 10% of the unconfined compressive strength (before considering safety factors). Such relationships, though, cannot avoid testing, since the estimate of parameters is very crude with such an approach. Yet, the authors suggest the need to conduct new experiments on other types of soil to validate their approach.

Miccoli *et al.* (2016) investigated the response of rammed earth walls under in-plane cyclic shear-compression tests, which were provided by increase of lateral load and displacements. When evaluating the mechanical properties under static loading, the samples results showed a very low shear strength (τ_{max}) of 0.07 MPa. The shear modulus (G) was also measured, reaching 1582 MPa.

To evaluate the shear strength behavior on rammed earth walls (and two other earth type materials), Miccoli, Müller and Fontana (2014) applied diagonal compression tests – very common for masonry material – on their wallettes specimens. For this test, rammed earth wallettes were turned by 45° around the middle axis, so the configuration could induce shear forces (Figure 2.8). The failure observed revealed a strong shear component, different from usual monolithic materials. The problem is that this is not a homogeneous test, and despite creating shear stresses, the failure takes place mainly in tension. Thus, this is not a recommended test for evaluating the shearing performance on rammed earth.
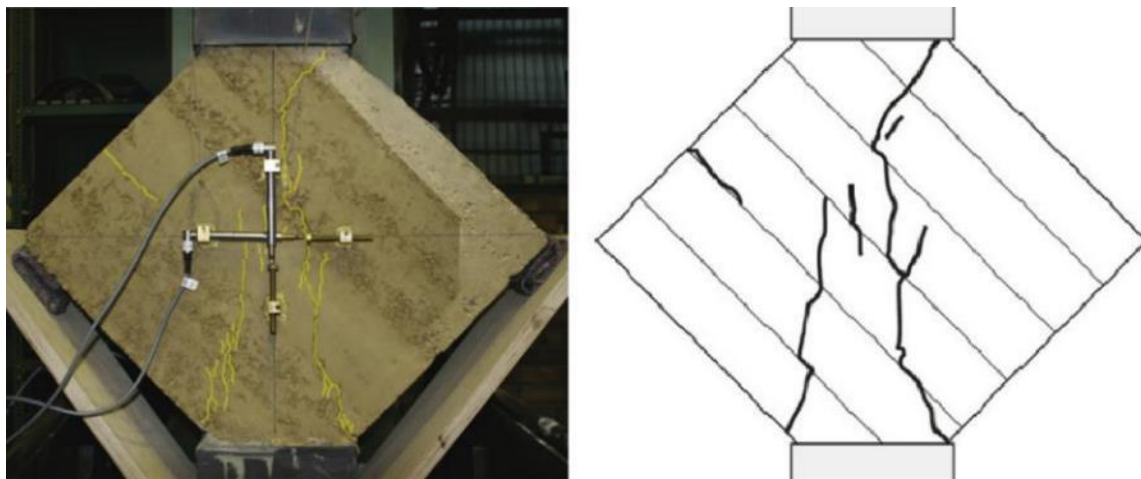
**Figure 2.8 – Diagonal compression test performed on a rammed earth wallet
(Miccoli, Müller and Fontana, 2014)**

Results of shear tests from Vargas-Neumann[6]; cited in Miccoli, Müller and Fontana (2014) showed that clay, water content and compaction highly influence the shear resistance of rammed earth. In fact, rammed earth walls from their work were 40% more resistant to earthquakes when compared to adobe masonry walls. Jaquin *et al.* (2009) studied the behavior of rammed earth walls, including the source of shear strength, which increases as the matrix suction increase.

2.2.5   Flexural (bending) strength

As pointed out for the tensile and shear strength, the same is suggested for bending: designing for pure flexural should not be taken, but assuming a value around zero (Maniatidis and Walker, 2003; Librici, 2016). However, sometimes is necessary to evaluate the behavior of rammed earth on bending.

---

[6] Vargas-Neumann, J. (1993) 'Earthquake resistant rammed earth (tapial) buildings', *Proc. 7a conferência internacional sobre estudo e conservação da arquitetura de terra.* pp. 140-151.

Values of bending strength was provided on Otcovská and Padevět (2017) work by means three-point bending tests carried out on small prisms (4 cm base x 16 cm high). They evaluate the dependence of bending strength on the amount of clay and its dependence on the amount of water, separately. Three different soils were used for these both analyses. Results showed an increase of bending strength followed by the increase of clay content. On the opposite, for the second analysis with the clay content fixed, results indicated bending strength also increased with increase of water content. This last result was not expected, though the authors proposed further studies to evaluate that behavior (Riyono, Vincens and Plassiard, 2017).

2.2.6   Durability

Bui *et al.* (2009) presented an extensive study on the durability of stabilised and unstabilised rammed earth walls, by exposing them for 20 years to natural conditions in France. According to them, durability of rammed earth structures is still controversial, which is mainly linked to the fact that earth is very sensitive to water. However, the authors point that there are several old buildings with still suitable performance, such as the traditional rammed earth houses in France.

The durability of the specimens is linked to the erosion on the walls surface. Bui *et al.* (2009) observed for most of the walls that the upper part (about 20% of the height) was less eroded due to the protection of the roof. An erosion depth up to 5% of the wall thickness is acceptable for occupants, regarding rammed earth walls are overdesigned and constructed with a high safety factor (from 3 to 10). The mean erosion depth observed on the 20-years-studied walls was of 2 mm (0.5% of the wall thickness) for the stabilised and about 6.4 mm (1.6% of the wall thickness) for the unstabilised walls.

The erosion of a rammed earth wall through time is not a linear function. It is higher during the first years after construction, and then it stabilizes. High initial erosion may happen due to the loss of compaction energy in contact with the formwork which causes friction. The region in contact with the formwork is less compacted and though more eroded (Bui *et al.*, 2009).

3. CJS-RE: A NEW CONSTITUTIVE MODEL FOR RAMMED EARTH

Numerical modelling is an important tool for the understanding of mechanical behavior of rammed earth structures. Additionally, it is useful to prior decisions regarding conservation and repair of rammed earth constructions (Silva *et al.*, 2014). But in fact, there are several difficulties in modelling the mechanical behavior of rammed earth. As observed by Riyono *et al.* (2017), defining the most suitable theory that should be used is a complex process. According to them, rammed earth is similar to concrete as a quasi-brittle material, so they could probably follow similar constitutive law. Nevertheless, the possibility of using available constitutive laws from concrete directly on rammed earth modelling is still uncertain.

Simple constitutive laws for the study of rammed earth material, such as those based on linear elastic isotropic and elastic-perfectly plastic behavior (Jaquin, 2008; Bui *et al.*, 2016), are not very representative (Riyono, Vincens and Plassiard, 2017). Models within the framework of damage elasticity can also be found (T. T. Bui *et al.*, 2014). Champiré *et al.* (2016) suggest that unsaturated damage elasto-plastic models would be necessary for an exhaustive modelling of rammed earth behavior.

Among all theories previously identified, this chapter is focused on a hierarchical constitutive model for the mechanical behavior of rammed earth walls denoted CJS-RE. This constitutive model, based on the elasto-plasticity theory, was originally developed by Cambou and Jafari (1988) for granular materials and then modified and improved by different works. The hierarchical characteristic of this approach indicates that, between two complexity levels, the more appropriate version can be selected, which depends on the information available to identify a possible set of model parameters (Riyono, Vincens and Plassiard, 2017).

3.1 CJS-RE1: a first-level model

This first approach proposed by Riyono *et al.* (2017) has the background on the elasto-plastic model from Mohr-Coulomb criteria, but adapted to represent quasi brittle materials. Two types of failures can be observed for quasi brittle materials, and two failure surfaces can be associated: one due to excessive shearing (f^s) and the other due to excessive tensile stress (f^t). Both surfaces f^s and f^t are indicated on Figure 3.1, in the meridian plane and in the deviatoric plane. I_1 is the first invariant of the stress tensor, S_{II} is the second invariant of the deviatoric stress tensor, S_1, S_2 and S_3 are the principal stresses of the deviatoric stress tensor. These plastic failure surfaces delimit a domain within the stress space of acceptable state of stress from other that are not physically reached by the material. A review of the deviatoric stress tensor and the invariants is presented in ANNEX A.

The model involves three mechanisms of deformation: one elastic and two plastic. The first mechanism is governed by Hooke's law. The second and the third plastic mechanisms are activated when the

current state of stress reaches one of the failures surfaces by shearing or tension. Thus, the incremental deformation tensor $\dot{\varepsilon}^{total}$ can be written as:

$$\dot{\varepsilon}^{total} = \dot{\varepsilon}^e + \dot{\varepsilon}^{sp} + \dot{\varepsilon}^{tp} \tag{2}$$

where $\dot{\varepsilon}^e$ is the increment of the elastic deformation tensor, $\dot{\varepsilon}^{sp}$ is the increment of plastic deformation tensor due to the shear mechanism and $\dot{\varepsilon}^{tp}$ is the increment of plastic deformation tensor due to the tensile mechanism.
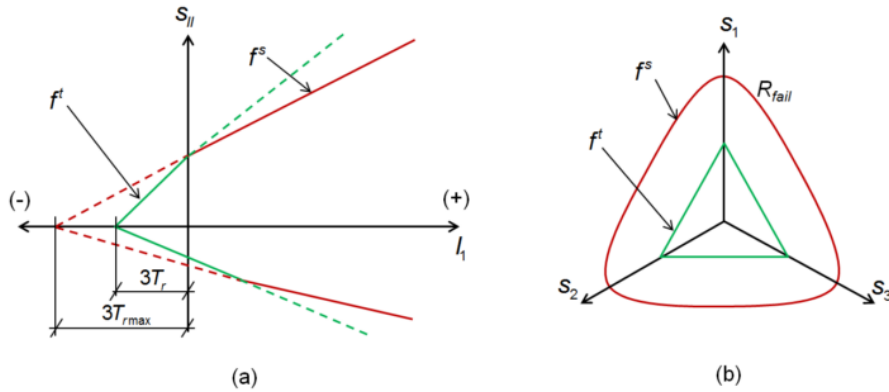
Figure 3.1 - Failure surfaces of CJS-RE1; (a): in the meridian plane (σ2=σ3) and (b): in the deviatoric plane (Riyono, 2017)

3.1.1 Elastic mechanism

The first elastic mechanism computed according to Hooke's law is:

$$\dot{\varepsilon}^e = \left(\frac{1+\upsilon}{E}\right)\boldsymbol{\sigma} - \left(\frac{\upsilon}{E}\right)tr(\boldsymbol{\sigma})\boldsymbol{I}_d \tag{3}$$

where E is the Young's modulus, υ is the Poisson ratio, $\boldsymbol{\sigma}$ is the stress tensor and $\boldsymbol{I}_d$ is the identity tensor.

3.1.2 Shear plastic mechanism

In this first level, both shear yield and shear failure surfaces are confounded and written as:

$$f^s(\boldsymbol{\sigma}, R_{fail}) = s_{II}h(\theta_s) - R_{fail}(I_1 + 3T_{r\,max}) \leq 0 \tag{4}$$

where s_{II} is the second invariant of the deviatoric part of the stress tensor $\boldsymbol{\sigma}$, $h(\theta_s)$ represents the shape factor of the dissymmetry of the shear failure surface, I_1 is the first invariant of the stress tensor, R_{fail} is the average radius of the shear failure surface and $T_{r\,max}$ is the maximum tensile strength of the material.

The shape factor $h(\theta_s)$ is defined as:

$$h(\theta_s) = \left(1 - \gamma cos(3\theta_s)\right)^{1/6} \tag{5}$$

where θ_s is a Lode angle in the deviatoric plane such that $\theta_s = 0°$ corresponds to a compression stress path and $\theta_s = 60°$ to an extension stress path. γ is a model parameter which quantifies the dissymmetry of the failure surface along a compression and an extension stress path.

The increment of plastic shear deformation ($\dot{\varepsilon}^{sp}$) is governed by a non-associated flow rule. The direction of this plastic deformation is given by a potential surface g^s. The flow rule is defined as:

$$\dot{\varepsilon}^{sp} = \dot{\lambda}_s \frac{\partial g^s}{\partial \boldsymbol{\sigma}} \tag{6}$$

where $\dot{\lambda}_s$ is the plastic multiplier of the shear mechanism. To avoid the complexity on defining the potential surface, the direction $\boldsymbol{G}$ of the increment of plastic deformation is directly computed. To compute shearing $\boldsymbol{G}$, different phases of contractancy and dilatancy are necessary and they must satisfy the following dilatancy law of the plastic shear volumetric deformation ($\dot{\varepsilon}_v^{sp}$):

$$\dot{\varepsilon}_v^{sp} = \beta \left(\frac{s_{II}}{s_{II}^{mvc}} - 1\right) \frac{|\boldsymbol{s} \, \dot{\boldsymbol{e}}^{sp}|}{s_{II}} \tag{7}$$

where $\boldsymbol{s}$ is the deviatoric stress tensor, $\dot{\boldsymbol{e}}^{sp}$ is the increment of the deviatoric plastic strain tensor, β is a model parameter to ensure that positive volumetric deformations take place for contraction, according to the chosen convention, and s_{II}^{mvc} is the value of the second invariant of the deviatoric stress tensor at the Maximum Volumetric Contraction (MVC) state for the current value of the mean pressure.

For the sake of simplicity, the MVC surface is considered as isotropic with a similar shape to the shear failure surface:

$$f^{mvc} = s_{II}^{mvc} h(\theta_s) - R_{mvc}(I_1 + 3T_{r\,max}) \tag{8}$$

where R_{mvc} is the average radius of the MVC surface, which is a model parameter. Volumetric deformations are associated to contraction when $s_{II} < s_{II}^{mvc}$, otherwise to dilation.

3.1.3   Tensile plastic mechanism

The tensile yield surface is confounded with the tensile failure surface. This yield surface is able to soften and the tensile strength T_r can drop to zero when failure is triggered. This yield surface writes:

$$f^t(\sigma_3) = \sigma_3 - T_r \leq 0 \tag{9}$$

where σ_3 is the minor principal stress and T_r is the tensile strength. It is important to observe that this plastic flow rule is called associated, since this tensile plastic mechanism causes deformation parallel to the tensile stress direction.

The tensile softening is characterized by a sudden drop of the tensile strength once the tensile criterion is reached. This softening of the tensile yield surface is described by the following exponential function:

$$T_r = T_r^{ini} exp \left(\alpha_t \int \dot{\varepsilon}_t^p \, dt \right) \tag{10}$$

where T_r^{ini} is a model parameter which correspond to the initial value of T_r, α_t is a default parameter which is here equal to -1.0 (recommended). Then, for CJS-RE1 model, α_t does not need to be identified.

3.1.4   Identification of the model parameters for CJS-RE1

This basic level denoted CJS-RE1 involves eight parameters, from which seven can be identified and one is stated. The elastic parameters – the Young's modulus (E) and the Poisson's ratio (υ) – can be identified by a compression test, with the initial tangential properties of the experimental stress-strain curves. The shear plastic parameters (R_{fail}, $T_{r\,max}$, and γ) are obtained from two compression tests with different confining pressures and one extension test. As stated before, the MVC coincides with the failure state, i.e., dilation takes place when shear failure is reached. Parameter β can be estimated from the volumetric deformation curve of the compression test. The value of the tensile strength T_r^{ini} (equal to the maximum uniaxial tensile resistance f_t) can be obtained from a tensile test or Brazilian test. In case any of these tests is available, f_t can be estimated between the range of $5\% f_c$ and $12.5\% f_c$, where f_c is the maximum uniaxial compression resistance. Table 3.1 gives the CJS-RE1 parameters, showing some results of an experimental research obtained from literature.

Table 3.1: Identified model parameters for CJS-RE1 model for rammed earth with values obtained by an experimental work (Silva *et al.,* 2014; Riyono, 2017)

Elastic		Plastic	
E	= 760 MPa	β	= 1.0
υ	= 0,25 MPa	γ^7	= 0.894
		R_{fail}	= 0.37
		T_r^{ini}	= 160 kPa (defined as 8% of f_c)
		$T_{r\,max}$	= 350 kPa
		α_t	= -1.0 (stated as default)

---

[7] The value of γ indicated is the one usual for concrete. It was actually stated by Riyono (2017) in his work because no extension test on rammed earth was available by Silva *et al.* (2014). This proposed work is especially interesting to evaluate this parameter.

3.2 CJS-RE2: a second-level model

This second level of the CJS-RE model is similar to the first one, but it introduces the use of a deviatoric yield surface different from the shear failure, which tends to reduce the domain where elasticity can take place. An isotropic hardening of the deviatoric yield surface is added, which is controlled by a model parameter. Besides hardening, CJS-RE2 model can also exhibit a shear softening and a controlled tensile softening. The failure and yield surfaces are indicated on Figure 3.2, both in the meridian and deviatoric plane.
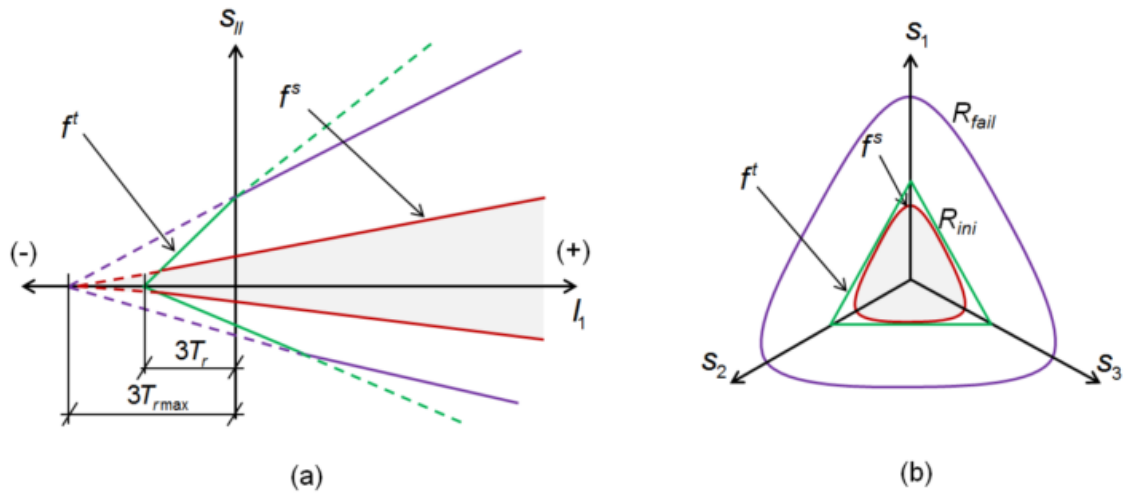
Figure 3.2 - Failure surfaces of CJS-RE2; (a): in the meridian plane (σ2=σ3) and (b): in the deviatoric plane (Riyono, 2017)

3.2.1 Isotropic hardening

When shearing, the yield surface can expand isotropically. Its size can be identified by the average yield surface diameter R, which is written by a hardening law resulting in:

$$R = R_{fail} - (R_{fail} - R_{ini}) \exp(-Ap) \tag{11}$$

where A is a model parameter which controls the velocity of the isotropic hardening, R_{ini} and R_{fail} are respectively the initial value of the yield radius and the maximum size of the yield surface before failure, and, p is a hardening variable which comes from the following normality relationship:

$$\dot{p} = -\dot{\lambda}_s \frac{\partial f^s}{\partial R} = -\dot{\lambda}_s (I_1 - 3T_{r\,max}) \tag{12}$$

The hardening law gives that at the beginning, when the system is at elastic state ($p = 0$), R is equal to R_{ini}. Close to failure ($p \rightarrow \infty$), the value of R tends to R_{fail}.

3.2.2 Shear and tensile softening

In quasi-brittle materials like rammed earth, softening can occur from the development of cracks and decohesion of grains. The shear softening in CJS-RE is modelled by decreasing the maximum tensile resistance $T_{r\,max}$.from an initial to a residual value. The law implies that if the tensile failure surface is first reached, instead of the shear failure surface, the shearing capacity of the material automatically decreases according to the modelling. The shear softening law writes:

$$T_{r\,max} = (T_{r\,max}^{ini} - T_{r\,max}^{res}) \exp\left(\alpha_s \varepsilon_{diff}^{sp}\right) + T_{r\,max}^{res} \tag{13}$$

$$\varepsilon_{diff}^{sp} = \left\| \varepsilon^{sp} - \varepsilon^{p\,fail} \right\| \tag{14}$$

where $T_{r\,max}^{ini}$ is the initial value of $T_{r\,max}$, $T_{r\,max}^{res}$ is the residual value of $T_{r\,max}$, which is stated to be in this model equal to 20% of $T_{r\,max}^{ini}$, α_s is a parameter that controls the rate of shear softening, and ε_{diff}^{sp} is the norm of the difference between the current deviatoric plastic strain ε^{sp} and the deviatoric plastic strain at peak $\varepsilon^{p\,fail}$.

In this second level, CJS-RE2, the tensile yield surface softens with a velocity that can be controlled through the value of the parameter α_t, which was previously presented for CJS-RE1 model. In this case, α_t is stated as equal to -0.5 to give a gradual tensile softening.

3.2.3 Identification of the model parameters for CJS-RE2

CJS-RE2 level involves twelve parameters, from which ten can be identified and two are stated. The identified parameters are two from elastic state (E and υ) and eight from plastics state ($\gamma, R_{fail}, T_{r\,max}^{ini}$, $T_r^{ini}, \beta, R_{ini}, A$ and α_s). The three additional parameters compared to CJS-RE1 are R_{ini}, A and α_s. The initial yield radius (R_{ini}) is obtained from a compression test and corresponds to the linear zone of behaviour in the stress-strain curve. The isotropic plastic hardening parameter (A) of the shear yield surface and the parameter which controls the shear softening velocity (α_s) are determined by a trial-and-error method using CJS-RE model. Two plastic parameters ($T_{r\,max}^{res}$ and α_t) are stated therefore not need to be identified. Table 3.2 provides the CJS-RE2 parameters, showing some results of an experimental research obtained from literature.

Table 3.2: Identified model parameters for CJS-RE2 model for rammed earth with values obtained by an experimental work (Silva *et al.*, 2014; Riyono, 2017)

Elastic		Plastic	
E	= 760 MPa	β	= 1.0
υ	= 0,25 MPa	γ^8	= 0.894
		R_{fail}	= 0.37
		T_r^{ini}	= 160 kPa (defined as 8% of f_c)
		$T_{r\,max}^{ini}$	= 350 kPa
		R_{ini}	= 0.16
		A	= 0.00013
		α_s	= -0.0003
		$T_{r\,max}^{res}$	= 70 kPa (stated to be 20% of $T_{r\,max}^{ini}$)
		α_t	= -0.5 (stated to give a gradual softening)

3.3 Stress-strain relationship using CJS-RE model

As previously indicated, the difference between CJS-RE1 and CJS-RE2 hierarchical levels relies on the refinement introduced in the second level, which is the use of a deviatoric shear yielding surface different from the shear failure surface. As consequence, the domain of elasticity in the second level is far smaller than the first one (Riyono, 2017).

Figure 3.3 indicates the typical responses of CJS-RE1 ("a" to "c") and CJS-RE2 ("d" to "e") through a compression stress path where the yield shear surface is activated. The stress-strain curve and the corresponding volumetric deformation curve can be compared for both levels (Riyono, 2017).

---

[8] The value of γ indicated is the one usual for concrete. It was actually stated by Riyono (2017) in his work because no extension test on rammed earth was available by Silva *et al.* (2014). This proposed work is especially interesting to evaluate this parameter.
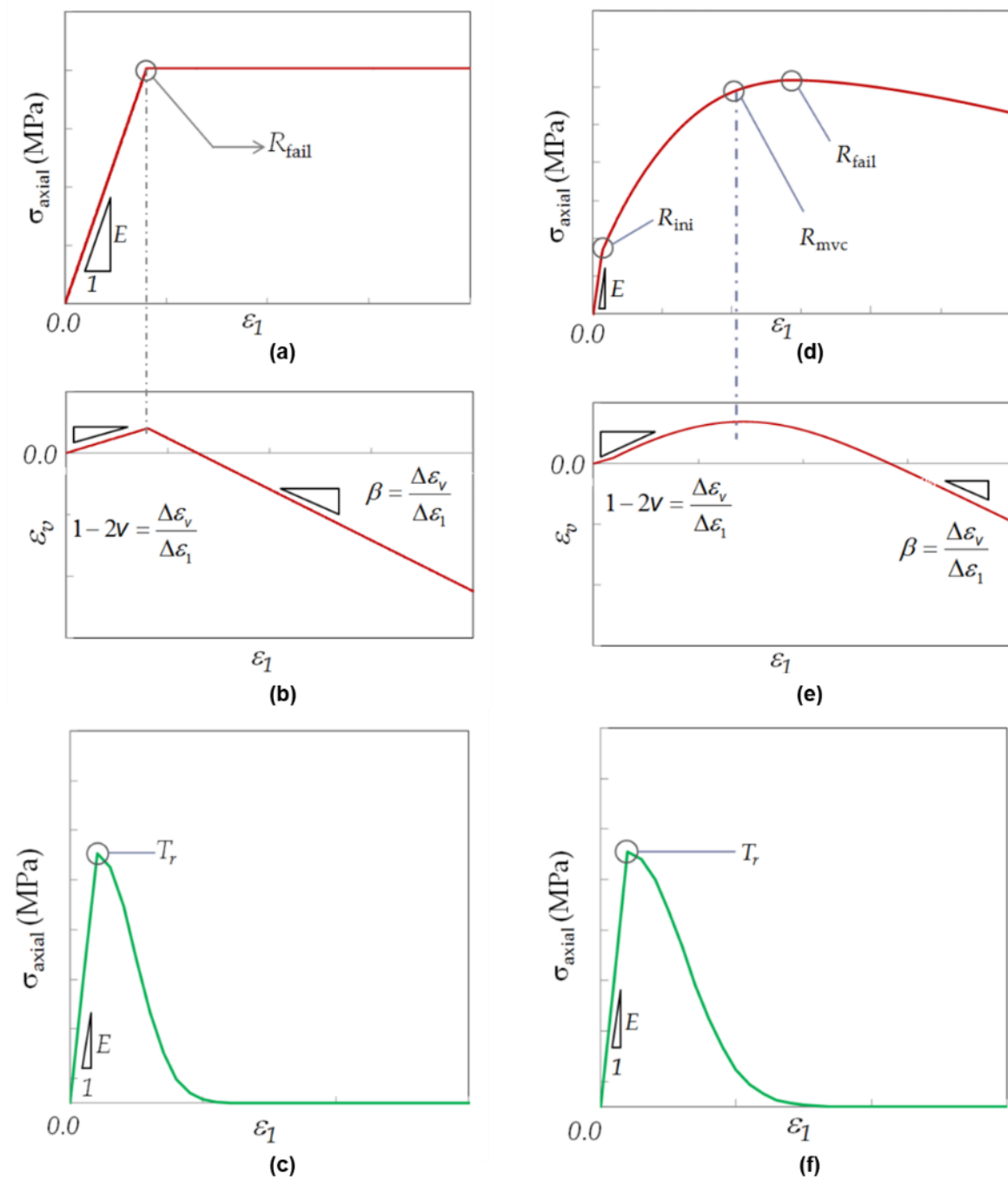
Figure 3.3 – Simulation of a compression stress path with CJS-RE models; (a), (b), (c) for CJS-RE1, and (d), (e), (f) for CJS-RE2 (Riyono, 2017)

4. METHODOLOGY AND TESTED MATERIAL

The main objective of this study – the identification of different plastic failure surfaces – was made possible by carrying out some experimental tests under compression, extension and tensile stress path. The new constitutive law CJS-RE was previously validate using two sets of experiment references from the literature (Riyono, 2017). Though, the experiments here proposed come also to contribute as a third source to the validation of CJS-RE model. But prior to presenting results, providing information about the methodology, materials and manufacturing procedures of samples is of great importance.

4.1 Methodology

In summary, the methodology consisted in carrying out compression, extension and Brazilian tests, which allowed the parameters described by CJS-RE model to be identified. A more detail description of the triaxial device (for compression and extensions tests) is given in APPENDIX A.

Compression tests were carried out using a load frame-based triaxial testing system with displacement control of 1mm/min, which warrantees a quasi-static condition. Together with recorded deviatoric load data, a sensor with 10 kN capacity recorded the vertical displacements. Then, stress-strain curves could be build, providing the maximum resistance and the elastic modulus of each tested sample. Void pressure was applied under the base of the sample to better fix it to the cell. For the confining pressure, a hydraulic system was used for pressures up to 0.6 MPa, whilst an advanced pressure controller was adopted for higher pressures up to 1.3 MPa. The unconfined compression tests had the same procedures, with the difference that no pressure controller was used, obviously because there was no confining pressure within the cell.

Extension tests were performed with the same system. The difference is that void pressure was applied to hold the sample no only under the sample base, but also over the top. For configuration of extension tests, the loading velocity was adjusted for a negative value of -1mm/min.

Brazilian tests were used for indirect measurement of the tensile strength. Samples were set horizontally and the load was increased at a constant displacement rate of 2mm/min. The load was applied perpendicular to the lateral surface of the cylinder until its failure.

Besides providing information about the mechanical behavior of rammed earth by carrying out the tests briefly exposed, this work originally aimed to identify and compare the plastic failure surfaces for three different water contents within rammed earth material. To ensure the repeatability of results, three tests for the same water content and stress path state were originally suggested (see Table 4.1). However, some issues have affected the proper planning and performance of this work within the time available. Technical adjustments of the triaxial system, unexpected repairs performed inside the laboratory for two

weeks, and other difficulties related to the fragility of rammed earth samples in wet state are some of the main problems faced.

Thus, without undermining the importance of this work, the range of water contents to be evaluated was reduced from three to two. Consequently, just the ranges of 1-2% and 3-4% water contents are considered in this work, and the third of 8-10% was not evaluated. For the sake of simplicity, the first range of water content (1-2%) is denoted as w = 2%, and the second (3-4%) as w = 4%. The repeatability of three tests (i, ii, and iii) was provided just for the first range of water content under study. For the second range, a repeatability of two tests (i and ii) showed to be suitable for a first evaluation. For each studied water content, the proper identification of shear and tensile failures is done by carrying out four types of tests:

        a) unconfined compression test;

        b) confined compression test with three different confining pressures (0.3MPa, 0.6MPa and 0.8MPa);

        c) extension test with three different confining pressures (0.6MPa, 0.8MPa and 1.3MPa);

        d) Brazilian test

Considering the points previously exposed, from the global number of 72 tests originally proposed (24 for each one of the three studied water contents), a total amount of 40 cylindrical rammed earth specimens were tested. First, a set of 24 specimens aimed to provide results for the range of w = 2%. This is the water content achieved by letting the cylinders naturally dry for at least a week. Later, 16 specimens were manufactured for evaluation the water content (w = 4%). This higher water content was possible by keeping naturally-dried cylinders inside boxes under relativity humidity of 97% and temperature of 21ºC for about twenty days, with the process previously described.

Table 4.1: Proposed tests for the experimental study

TEST	CONFINED PRESSURE [MPa]	WATER CONTENT w = 2%			WATER CONTENT w = 4%		
		i	ii	iii	i	ii	iii
Unconfined compression	-	Test 03	Test 07	Test 12	Test 18	Test 19	n/a
Confined compression	0.3	Test 01	Test 05	Test 06	Test 17	Test 30	n/a
	0.6	Test 08	Test 13	Test 15	Test 16	Test 49	n/a
	0.8	Test 33	Test 34	Test 36	Test 47	Test 48	n/a
Extension	0.6	Test 27	Test 28	Test 37	Test 32	Test 50	n/a
	0.8	Test 25	Test 26	Test 38	Test 35	Test 51	n/a
	1.3	Test 24	Test 45	Test 52	Test 53	Test 54	n/a
Brazilian	-	Test 40	Test 41	Test 42	Test 43	Test 44	n/a

The range of tests here proposed is suitable for the proper identification of the plastic shear and tensile failure surfaces within the first two water contents. However, further experiments are suggested to achieve the global objective initially conceived, specially to verify the behavior under w = 8-10%.

4.2   Physical properties of material

The material was supplied by a builder from a site where a rammed earth construction was built (using this specific material), close to the city of Lyon.

4.2.1   Soil sensitivity to water

As a first attempt to identify the sensitivity to water, Methylene Blue tests (MetBT) were carried out following the guidelines of the French standard NF P 94-068 (Norme Française, 1993), as presented in section 2.1.2. Firstly, the state of water content within the soil (expected about 1-2%) needed to be confirmed. In this process, a small sample of naturally dried soil was left to dry for 24 h in oven under a temperature of 100°C, and the final weight was measured. After the drying period, the new weight of the soil was measured, and so the water content was calculated by the following formula:

$$\omega_{sample} = \frac{m_w - m_d}{m_w} \tag{15}$$

where ω_{sample} is the water content within the sample, m_w is the mass of soil before the drying period ("wet" state), m_d is the mass of soil after the drying period ("dry" state).

Then, the first approach for the MetBT was taken with the objective to obtain an idea of the magnitude of MetB required by the soil voids to be used for the next tests. Furthermore, the glass burette that receives the MetB liquid had a limit of 50 ml, so choosing an initial sample of soil that requires about 50 ml or less to saturate its voids was especially advantageous: the laboratory procedures were faster and less susceptible to errors.

Next, five tests were carried out to evaluate the concentration of methylene blue (MetB) required by the soil. Each one of these tests had the following steps (Norme Française, 1993):

   a) firstly, the sample of soil was weighed and then mixed with 500 ml of distilled water in a recipient and left to shake for about 5 min by a soil dispersion electric mixer;

   b) a drop was taken from the soil-and-water suspension and set into a filtered paper to verify its initial brown-soil color;

   c) the process started adding 5 mL of MetB inside the suspension, while the electric mixer continued working to disperse it. After 1 minute, a drop was taken from the blend and put into the filtered paper to verify its color. The objective was to verify if the test was positive or negative. The MetBT is positive when a light blue color is observed surrounding the MetB, which has a dark blue color;

   d) after the first drop, a second amount of 5 mL of MetB was added to the suspension and dissolved by distilled water. Then, after 1 minute, a new drop was observed on the filter paper, resulting again a negative test;

f) the same steps were carried out when adding in the suspension 5 mL of MetB each time. Then, when the test appeared to be positive, four verification steps were carried out, taking a drop each 1 minute and evaluating its color;

g) if all four verification steps confirmed the positive test (light blue color halo), then the process of adding MetB stopped. Otherwise, new amounts of 2 mL each time had to be add to the suspension, until a positive test is found;

h) finally, when the positive test is found again and confirmed by the four verification steps, then the final cumulative volume of MetB is registered as the one required to saturate the soil voids, for the mass of soil of each test.

As an example, Figure 4.1 indicates three drops of methylene blue test. They represent different concentration of methylene blue (MetB) into the solution.

(a)   (b)   (c)
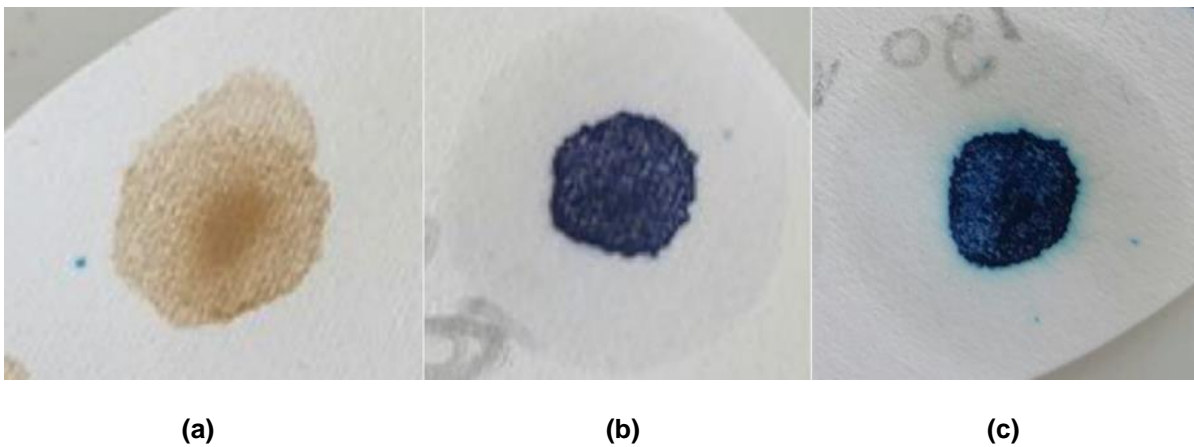
Figure 4.1 – Drops on filtered paper during MetBT: without MetB (a), negative test (b), and positive test (c) representing the MetB required for the maximum adsorption by clay

The final volume of MetB from the first approach and the five tests are presented in **Erro! Fonte de referência não encontrada.**. APPENDIX B includes all steps developed from methylene blue tests. From each test, the Methylene Blue Value (MetBV) was determined by the following relation:

$$MetBV = \frac{100 \cdot B}{m_0} \xrightarrow{B = V \cdot \rho_{MetB}} MetBV = \frac{100 \cdot V\,[ml] \cdot 0.01\left[\frac{g}{ml}\right]}{m_0\,[g]} = \frac{V\,[ml]}{m_0\,[g]} \tag{16}$$

where, from each test, m_0 is the mass of soil of the suspension; B is the MetB mass corresponding to the total MetB volume added to the suspension; V is the volume of MetB added to the suspension; and ρ_{MB} is the density of MetB (0.01 g/ml).

Results of the MetBV showed a good repeatability, with an average of 1.5. Soils with this value, which distinguishes sand-silty soils from sand-clayey soils (review Table 2.2), begin to show some sensitivity to water, i.e., capacity of the material to properly store water within its voids. With this first approach, the soil appears to be suitable for rammed earth technique. The MetBV of 1.5 translates the characteristic

of a soil which contains enough clay to provide the binder phenomenon between particles, but keeping sufficiently low clay content to avoid excessive shrinkage on the material's surface.

Table 4.2: Results of the methylene blue tests (MetBT)

Test	Volume of MB added to the solution	Mass of soil	MetBV
First Approach	120 ml	76.7 g	1.6
Test 1	45 ml	32.9 g	1.4
Test 2	60 ml	38.3 g	1.6
Test 3	50 ml	31.6 g	1.6
Test 4	55 ml	34.5 g	1.6
Test 5	40 ml	26.0 g	1.5
Mean tests 1 to 5	**50 ml**	**32.7 g**	**1.5**

4.2.2   Particle size distribution (PSD)

Particle size distribution (PSD) is an important information which helps understanding the behavior of soil. A dry sieving method should have been proposed to determine the grading of the soil used, however, the test was not developed for the submitted version of this work. Knowing its importance, the PSD curve will be provided for the day of defense.

To apply the soil for rammed earth samples, particles with diameter higher than 15 mm were removed by visual inspection and sieves. This selection of particles was taken because high-size gravels could greatly change the mechanical behavior of the small rammed earth specimens.

4.3   Physical properties of the samples

The soil used for manufacturing samples was firstly selected from an outside deposit and then reused after testing to produce new specimens (Figure 4.2 – a). When possible, condensed particles were break to feat into the limit size of 15mm diam., otherwise they were removed (Figure 4.2 – b). To confirm the initial water content within the soil, a small sample (on "wet" state) was taken from the amount and left to dry inside an oven under 60° for 24 hours. After the drying period, the new weight of the soil (on "dry" state) was measured, and so the respective water content could be obtained.

Then, water was added and mixed to the total amount of natural soil (Figure 4.2 – c) in order to set the optimum water content of 10% within the soil (Figure 4.2 – d). Just after adding the water, the mixture was kept in a plastic bag and strongly wrapped with duct tape to prevent it from drying out (Figure 4.2 – e). This optimum moisture content was defined by previous studies in the laboratory.

| (a) | (b) | (c) | (d) | (e) |
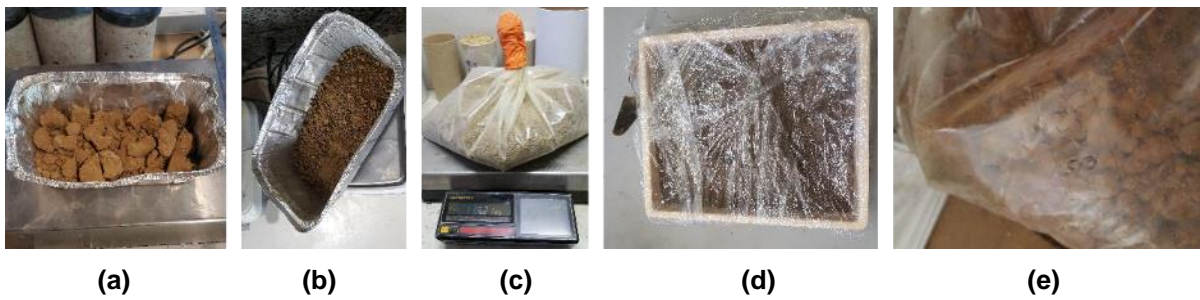
Figure 4.2 – Preparation of soil and samples prior to testing: reuse of soil (a), smashing condensed parts (b), knowing the weight of total soil before adding water (c), mixing water to the soil to obtain 10% of water content (d), and keeping the wet soil in plastic bag (e)

It is important to point out that previously to the development of this research some rammed earth cylinders were manufactured by a professional rammed earth builder, together with three rammed earth wallettes. These cylindrical specimens measured 7 cm diameter and 14-15 cm height, and they are identified in this work as "builder" samples. They were performed to represent in a small scale three rammed earth wallettes of 150 cm x 150 cm x 25 cm size. The walls were built to be loaded under in-plane shear tests for a doctorate research which is not involved with this experimental process. Nevertheless, is advantageous to remark these pre-existing samples, since they were used for comparison with the rammed earth specimens manufactured in this work.

A first approach for making new samples was taken to understand the manufacturing process and the compaction energy required to have similar cylinders as the pre-existing "builder" samples. The new samples were made compressing five layers on a metal mold of 7cm diameter and 15cm height (Figure 4.3 – a). The process was carried out with maximum attention to reproduce the quality of the "builder" samples. However, as a manual process, variation of the compaction effort is inevitable. Thus, the sample's height varied from 14 to 15cm. After practicing, rammed earth specimens were properly manufactured (Figure 4.3 – b). Is important to highlight that the pre-existing samples were not considered as additional data to identify the parameters of the constitutive law CJS-RE. They were tested in order to evaluate the testing processes and also to compare with results of this work.

For all the sample with desired final water content of 2% and 4%, after demolding from the metallic cylinder, the specimens were left to naturally dry for at least one week in order to achieve a proper resistance. Later, a thin layer of plaster (Figure 4.3 – c) was added under the base and over the top of each sample, except for those identified for Brazilian tests. To keep the standard, plaster was also added to the "builder" samples. This plaster provided a plane and smooth surface, which was necessary for a better transfer of load during compression and extension tests. At the end, each sample was identified with a number and its specific properties (day of manufacturing, set of soil and weight) (Figure 4.3 – d).

(a)   **(b)**   **(c)**   **(d)**
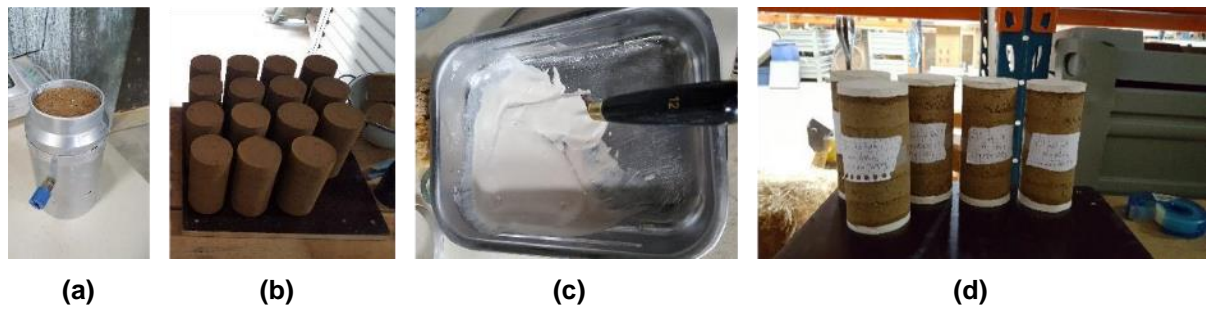
Figure 4.3 – Manufacturing process of samples: cylinder inside metal mold (a), cylinders in wet state after demolding (b), production of plaster (c), samples with base and top of plaster and their identification (d)

Some of the samples previously manufactured, which had already reached a water content of 2% after the natural dry period, were then prepared to gain water content until reaching the range of 4%. For this, they were kept inside boxes under a relative humidity (RH) of 97%. Each box received a solution of 500g of potassium sulfate (K_2SO_4) and 2 liters of water to reach this high RH (Figure 4.4 – a). The samples were then set over a metal grid (Figure 4.4 – b and c), and the boxes were closed and stored in a climatized room at 21ºC. A device with a sensor to measure the RH was used to control the conditions required (Figure 4.4 – d). The rammed earth specimens have been left inside these boxes for about 20 days to reach the range of 3-4% of target water content.

(a)   **(b)**   **(c)**   **(d)**
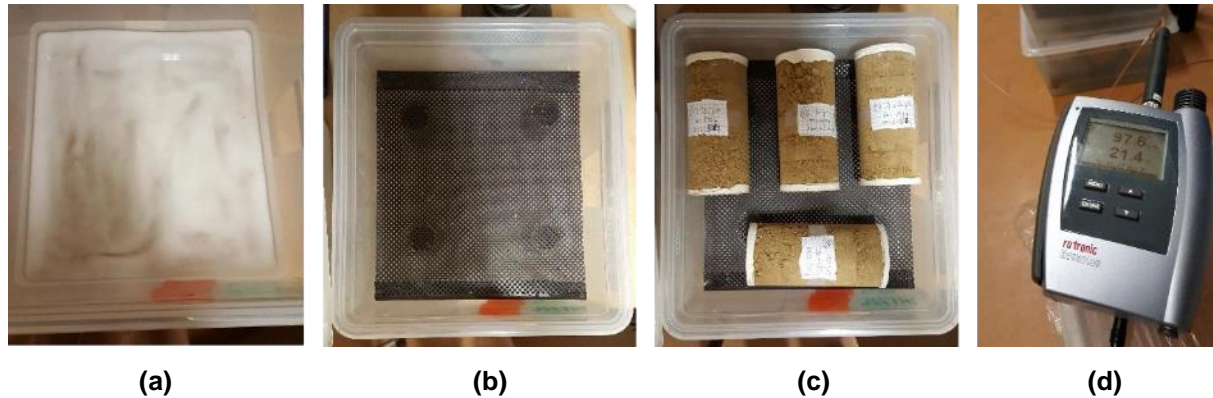
Figure 4.4 – Process to increase the water content within samples: box with K_2SO_4 and water (a), metal grid to support the cylinders (b) and (c), and device to control the RH (d)

The final step prior to testing was to envelop the cylinders with two membranes, the first with 5cm diameter and the second with 7cm diameter (Figure 4.5). The use of theses membranes was necessary to perfectly avoid the contact between water and sample inside the cell of the triaxial testing machine. A third membrane was used for testing under the highest confining pressure (1.3 MPa). This measure was taken after several losses of samples (invalid tests) due to the rupture of the membranes, even before applying the load.

(a)   **(b)**   **(c)**
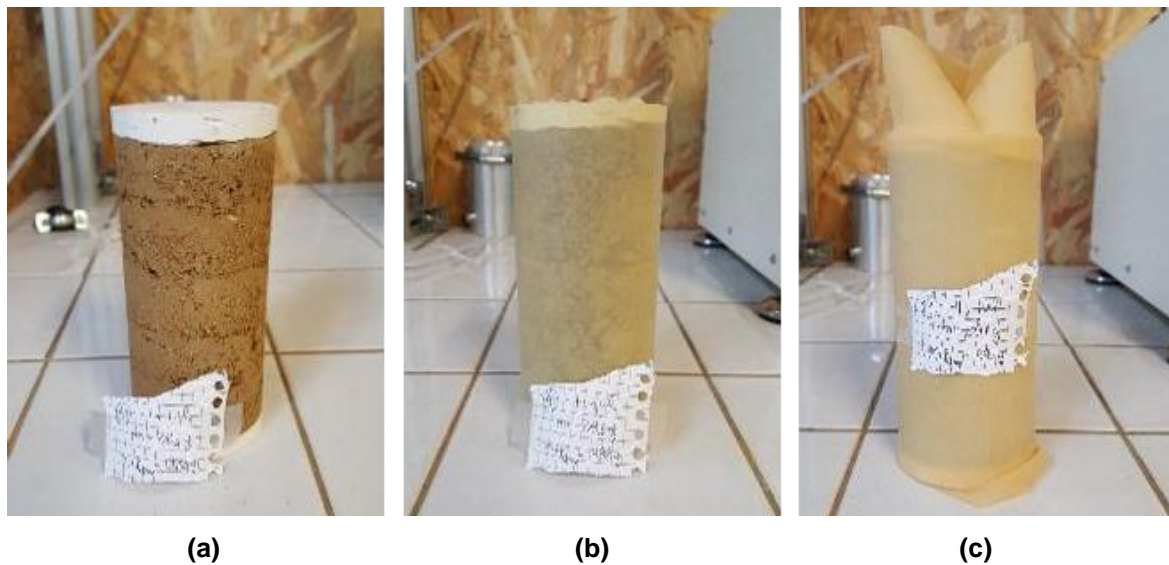
Figure 4.5 – Use of two membranes to envelop cylinders: rammed earth sample (a), thin 5cm diam. membrane (b), and second 7cm diam. membrane (c)

Rammed earth cylinders were manufactured in six different days, following the procedures above described. These six different sets of samples are identified here by the letters "A" to "F". From the six set of samples A to F (69 specimens) and the "builder" samples (15 specimens), a total of 84 rammed earth cylinders were originally considered for testing. The fragile characteristic of these specimens, mainly under wet state, cared for special attention when handling them. Nevertheless, 27 samples (32% of total specimens) broke during each step until testing phase. Some of them broke when demolding, others when adding the plaster, and some broke during the membrane enveloping. In addition, 7 specimens (8%) were destroyed and not considered in the results because of premature fail during testing operations, such as wrong procedures or rupture of the membrane before loading.

For each set of soil (A to F and Bd), the average dry density was estimated using two cylinders and evaluating the water content within them after a period of natural drying. Then, the water content of each sample was calculated knowing its mass, the initial optimum moisture content (around 10%) and the dry density of each set of soil.

The properties of each tested sample used in this study, including the pre-existing "builder" samples, are presented in APPENDIX C. Average values for all samples are indicated in Table 4.3.

Dry density directly influences the strength of rammed earth. Results indicate that the average dry density in this work is lower than those found on literature. Moreover, the set of samples A to F showed a dry density lower than the ones manufactured by a professional builder. As stated on section 2.1.4, this difference is explained mainly because of the following properties:

> a) compaction energy when manufacturing samples: it directly depends on who is applying the technique when compacting layers, thus it can lead to different material strength;

b) type of soil: different grading and clay mineral composition can result specimens with different mechanical properties, including strength;

c) moisture content during manufacture: it influences the suction phenomena and, though, the strength of the material.

The different dry densities among A to F sets are mainly explained because the first three sets of samples (A, B and C) were manufactured using 970g of soil, whilst the last ones (D, E and F) used 998g. Samples from the first sets broke easily, which indicated that the compaction effort was not strong enough. Though, changing the initial amount of soil was necessary to reach the minimum 14cm height for each sample, since they were more compacted. It is known that changing the compaction effort is a disadvantage for the repeatability results, but it was an important step to avoid losing more samples and, though, keep the experimental work. What also justifies the different dry densities is the moisture content during manufacture, which was difficult to control once the bag of wet soil is opened.

Despite those changes, the average dry density among all the set of samples A to F was 1657 kg/m³ (between limits of 1629 and 1698 kg/m³), which shows a low variability among them. This pattern comes to be positive for the experimental analysis, thus it overcomes the fact that dry density is below the average of other studies.

Table 4.3: Properties of samples

Set of samples	Number of samples manufactured	Number of samples tested	Average mass of tested samples [g]	Average dry density [kg/m³]
Bd	15	6	968	1765
A	4	4	908	1629
B	15	7	896	1637
C	16	5	896	1637
D	17	11	925	1675
E	11	8	935	1698
F	6	5	910	1667
Average/Total of sets A to F	69	40	912	1657

5.   IDENTIFICATION OF THE PLASTIC FAILURE SURFACES

Chapter 3 briefly presented the identification process for each parameter related to the plastic failure surfaces from CJS-RE constitutive law. It showed that CJS-RE1 involves eight parameters, from which seven can be identified and one is stated. On the other hand, CJS-RE2 involves ten parameters to be identified and two which are stated.

The stated parameters are those related to softening and plastic volumetric deformations. The experiments which could allow the softening parameters to be identified are much more complex and out of scope of this work, though their values are stated as proposed by Riyono (2017). Moreover, the lack of a sensor within the triaxial system to measure volumetric deformations did not allowed to identify the Poisson ratio (v), so its value was taken from literature based on experiments of rammed earth material.

Next, the identification of plastic failure surfaces is developed for w = 2%. For w = 4%, results will be presented in chapter 7, which is a first attempt to evaluate the influence of water content on the mechanical behavior of rammed earth.

5.1   Identification of shear failure surface

The shear plastic parameters which allow to identify the shear failure surface are the maximum tensile strength $T_{r\,max}$, the dissymmetry of the failure surface γ, and the failure radius R_{fail}. To identify these parameters, rammed earth cylinders were tested under compression and extension tests, following the methodology presented on chapter 4.

5.1.1   Maximum tensile strength $T_{r\,max}$

To identify $T_{r\,max}$, at least two compression tests are necessary. To increase the reliability of results, one unconfined compression test and three confined compression tests under different confining pressures (300 KPa, 600 KPa and 800 KPa) were proposed. It will allow as well to set if the shear failure surface is a cone in this range of stresses or if there is a curving of the surface for larger stresses.

Results of three repeatability tests for each pressure on the compression stress path are given in Figure 5.1. As expected, the maximum resistance increases with a higher confining pressure. Values from unconfined compressions showed a great repeatability. Under confined compression, the variation of maximum deviatoric strength was found larger, but no conclusion with respect to the influence of the confining pressure on the dispersion of results must be drawn.
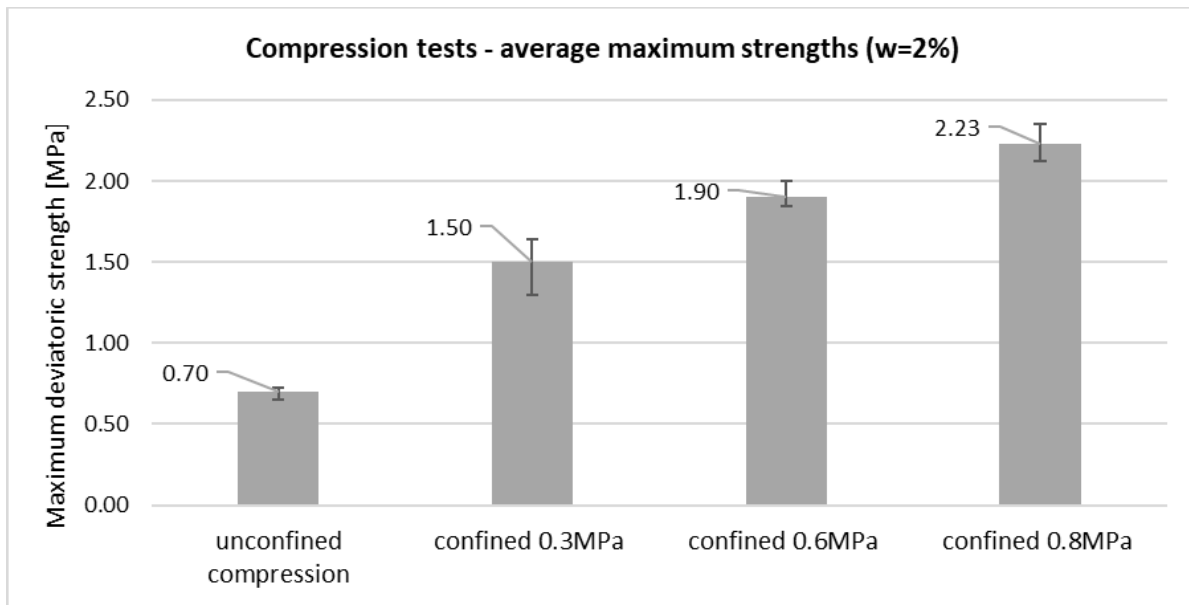
Figure 5.1 – Average results of the maximum deviatoric strength for compression stress path

The evolution of failure on samples under compression test are presented on Figure 5.2. A barrel shape is observed on samples which were under higher confinement pressure (600 KPa and 800 KPa). Apparently, for some samples the inclination angle of the failure surface increased following the increase of confining pressure. However, in several samples the failure surface was difficult to observe, since samples either broke when removing the membranes or the failure met a damaged region (such as layers interface) and its surface was not clear to identify.
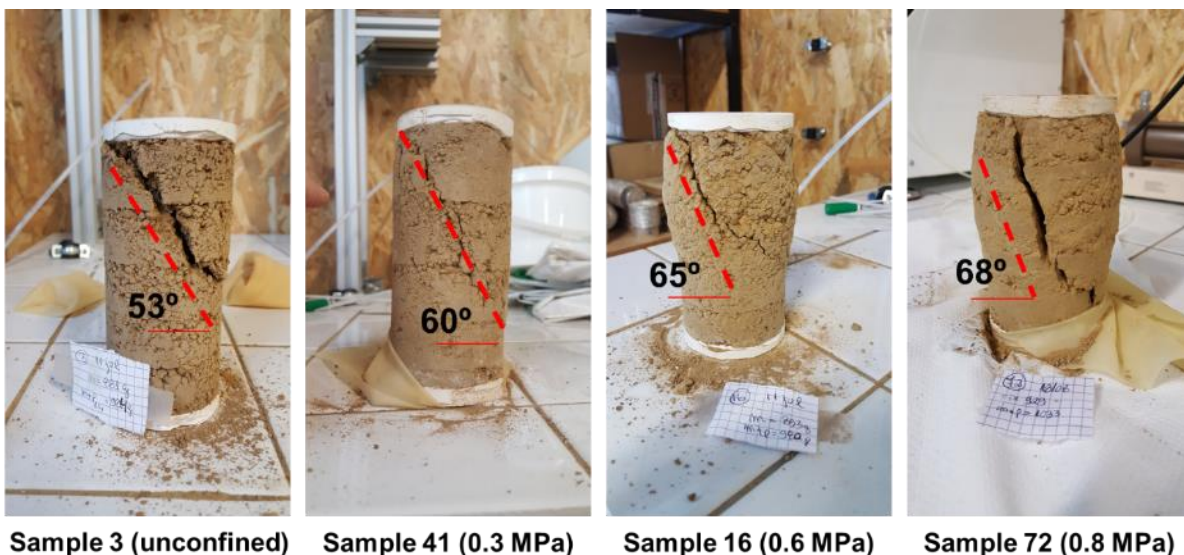
Figure 5.2 – Different failures observed on samples under compression test

After tests, the envelop of shear failure surface under compression stress path was identified with four different points (C1, C2, C3 and C4). Values were plotted in the meridian plane, with the first invariant of the stress tensor (I_1) on the horizontal coordinate and the second invariant of the deviatoric stress tensor (S_{II}) on the vertical coordinate (Figure 5.3). When the trend line of shear failure envelope for compression stress path (red line) finds the horizontal axis, the point T_I is identified. One can note that the shear failure surface is a cone in the range of the studied stresses which validates what was a *a priori* statement

Some expressions can be used to simplify the theory behind CJS model equations. In a triaxial axis-symmetry condition, I_1 and S_{II} write (Riyono, 2017):

$$I_1 = \sigma_1 + 2\sigma_3 = 3\bar{p} \tag{17}$$

$$S_{II} = \sqrt{\frac{2}{3}}|\sigma_1 - \sigma_3| = \sqrt{\frac{2}{3}}q \tag{18}$$

where σ_1 is the major principal stress and σ_3 is the minor principal stress, $\bar{p}$ is the mean pressure, and q is the deviatoric stress (second invariant of the deviatoric tensor).

Using the trend line equation from Figure 5.3, the value of $3T_{r\,max}$ is obtained:

$$3T_{r\,max} = (-)\,1.248\,MPa \rightarrow \boldsymbol{T_{r\,max} = (-)\,416\,KPa} \tag{19}$$
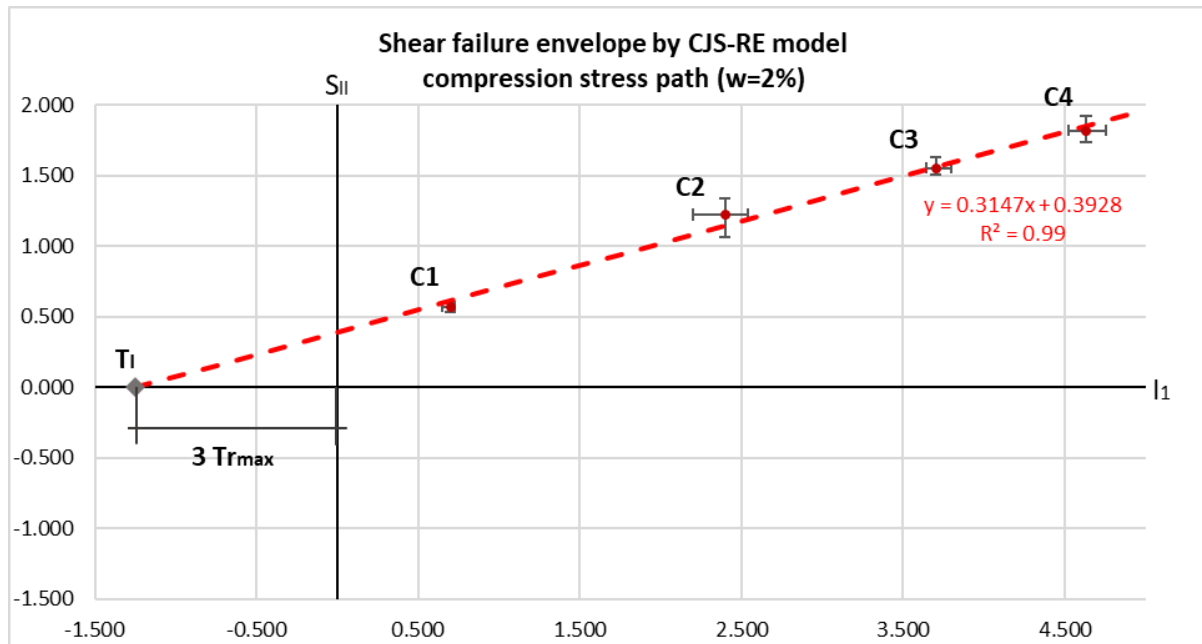
Figure 5.3 – Shear failure envelope for compression stress path

5.1.2 Dissymmetry of the failure surface γ

Parameter γ gives information about the intensity of the dissymmetry of the shear yield surface. It can be determined through triaxial compression and extension test for a same confining pressure.

Though, three repeatability extension tests were carried out for each of the three confining pressures (6, 8 and 13 bars). These pressures were specially selected to avoid reaching the tensile failure surface during extension tests, which could have possibly happened under low confining pressures. Results of the average maximum strength for extension are given in Figure 5.4.
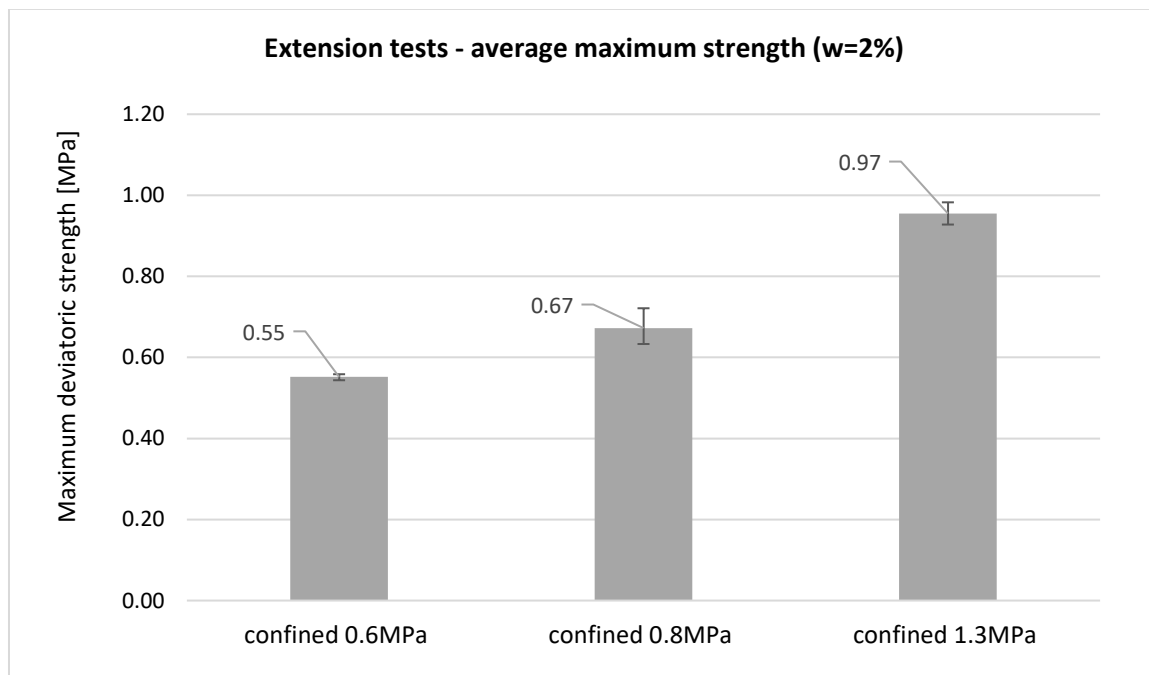
Figure 5.4 – Average results of the maximum deviatoric strength for compression stress path

As happened for the compression stress path, results also confirmed that the maximum resistance increases with a higher confining pressure for the extension stress path. Specimens showed a very good repeatability, especially with confining pressure of 0.6 MPa.

Regarding the observed failures (Figure 5.5), most of the samples broke close to the top or the bottom height. This may be explained by the low dry density (low compaction energy), which it could be responsible for a poor transfer of stresses between layers during extension tests. This can create damaged regions within the sample, from which the failure starts. The pre-existing samples, which had a higher dry density, showed the same behavior on extension. Perhaps, the difference of dry densities between the manufactured samples (sets A to F) and the pre-existing samples (set Bd) was not great enough to provide different failure on samples under extension tests.

Sample 65 (0.6 MPa)   Sample 81 (0.8 MPa)   Sample 84 (1.3 MPa)
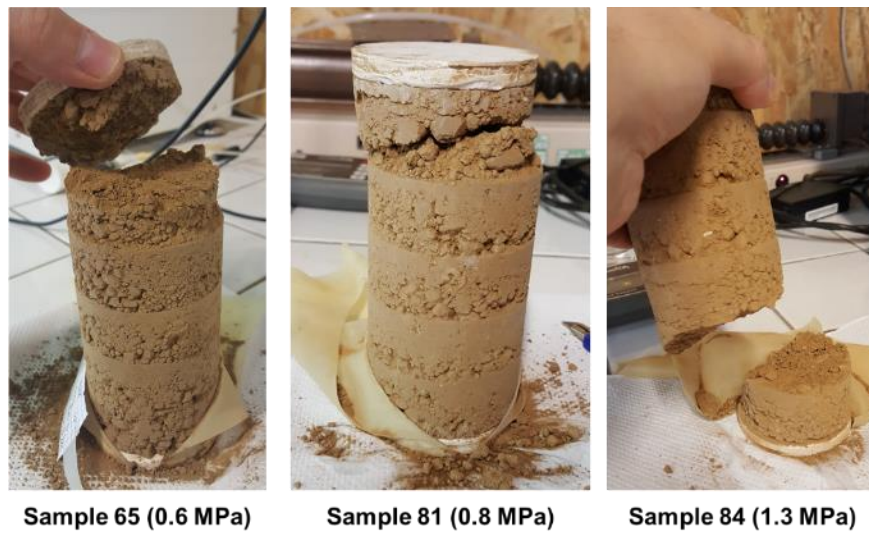
Figure 5.5 – Failure observed on samples under confined extension tests

With results from extension tests, the envelop of shear failure surface for extension stress path (Figure 5.6) could be identified with three different pressures (E1, E2 and E3). Points E1 (0.6 MPa) and E2 (0.8 MPa) were selected to follow the same confining pressures used for compression stress path (C3 and C4, respectively). Additional extension tests under confining pressure of 1.3 MPa gave higher reliability to the trend line of shear failure envelop for extension stress path (green line).
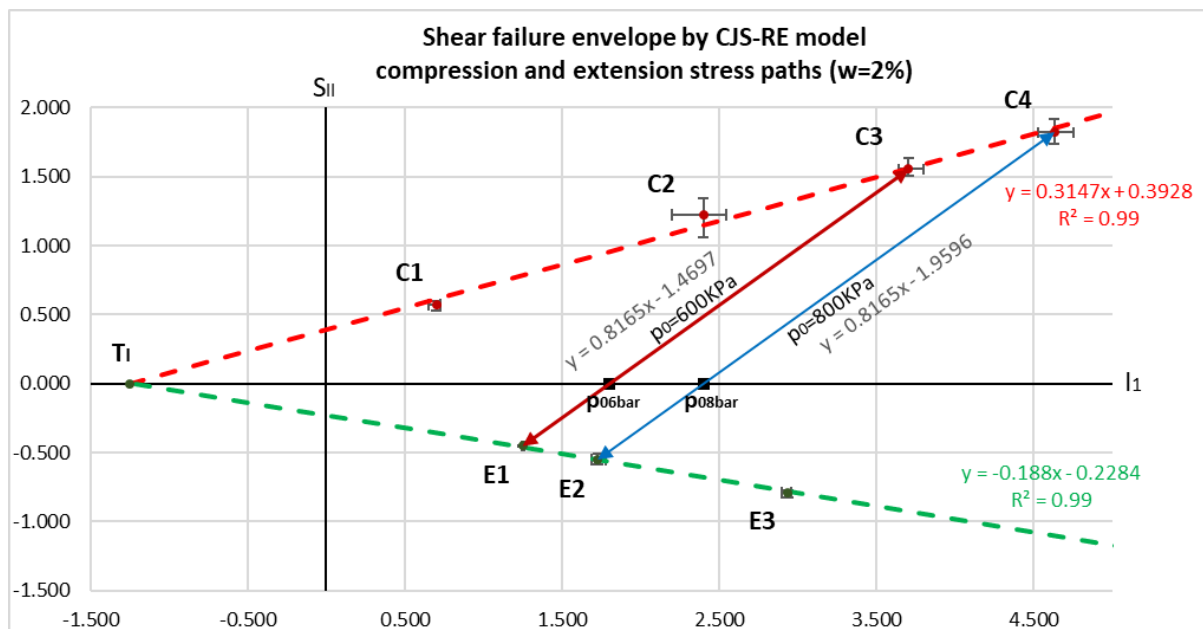
Figure 5.6 – Shear failure envelope for compression and extension stress paths

Now, the dissymmetry parameter of the shear yield surface (γ) can be determined. The following set of equations was used (Riyono, 2017):

$$\gamma = \frac{1 - F^6}{1 + F^6} \tag{20}$$

$$F = \frac{s_{II}^e (I_1^c + 3T_{r\,max})}{s_{II}^c (I_1^e + 3T_{r\,max})} \tag{21}$$

where, for a fixed confining pressure in the deviatoric plane, I_1^c and s_{II}^c are, respectively, the first invariant of the stress tensor and the second invariant of the deviatoric stress tensor when failure reaches the compression stress state; I_1^e and s_{II}^e are, respectively, the first invariant of the stress tensor and the second invariant of the deviatoric stress tensor when failure reaches the extension stress state; and $T_{r\,max}$ is the parameter previously identified, which represents the maximum tensile strength of the material.

Thus, the dissymmetry parameter (γ) can be determined choosing, for example, the stress path for the confining pressure $p0 = 0.6\,MPa$, and making use of the trend line equations of the shear plastic envelop from Figure 5.6 (red equation for compression and green equation for extension). The same process is developed choosing the confining pressure $p0 = 0.8\,MPa$.

The coordinates (values of I₁ and Sₗₗ) of the points C3, E1, C4, and E2 are determined by interception (and not the experimental average values) between shear failure envelopes and the stress path equations, such that:

       a) C3 is the interception between red and purple lines;
       b) E1 is the interception between green and purple lines;
       c) C4 is the interception between red and blue lines;
       d) E2 is the interception between green and blue lines.

The dissymmetry parameter γ was then calculated for both confining pressures using the trend line equations. Results of this interception method is given by Table 5.1.

Table 5.1: Identification of the dissymmetry parameter (γ) by using trend equations

Stress point	I_1^e [MPa]	s_{II}^c [MPa]	I_1^c [MPa]	s_{II}^e [MPa]	F	γ	γ (average)
C3	-	-	3.712	(+) 1.561			
					0.589	0.92	
E1	1.236	(-) 0.461	-	-			
							0.919
C4	-	-	4.688	(+) 1.868			
					0.59	0.918	
E2	1.723	(-) 0.552	-	-			

Thus, the average value for γ writes:

$$\gamma = 0.919 \tag{22}$$

Another method is to use the experimental values of the average maximum strength to determine the coordinates of C3, E1, C4, and E2. Results showed γ equal to 0.930 for the 0.6 MPa confining pressure and equal to 0.914 for the 0.8 MPa pressure (average of 0.922). The dissymmetry parameter should be the same, thus the difference here exists due to the great number of tests, which gave inherent errors between the selected points and the trend line (better saying, the red trend line, for example, does not necessarily match with the coordinates of points C1, C2, C3 and C4). However, this technique will be the one chosen in practical situations, when just a few number of tests would be carried out, i.e., the trend line would be build using just two points (R²=1), so there would be no difference by using either the trend line equation or the specific coordinates I_1 and S_{II} of those two points.

Parameter γ can be also described as a ratio between the radius at failure in tensile and in compression within the meridian plane (R_t/R_c). Figure 5.7 gives the shape of failure surfaces in the deviatoric plane for three different values of γ. The deviatoric plane is plane perpendicular to the hydrostatic axis for which I_1 is a constant.
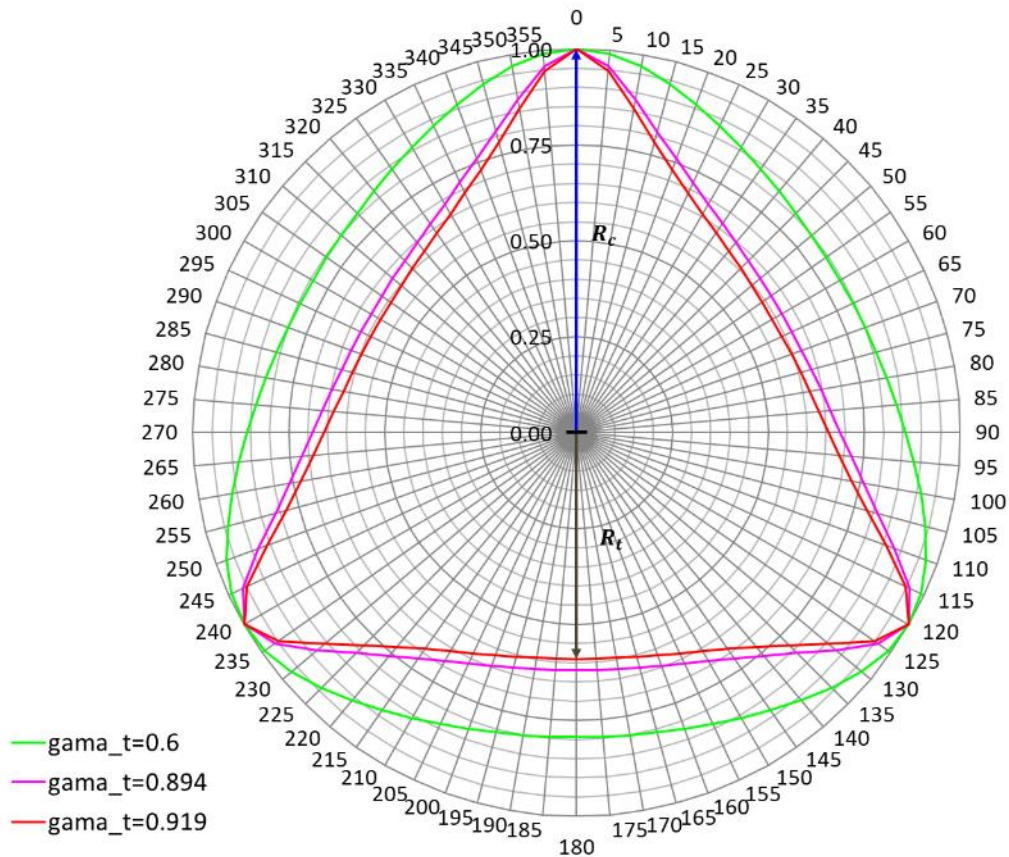
Figure 5.7 – Different shapes of CJS-RE model in the deviatoric plane with different γ (Riyono, 2017)

The value of parameter γ equal to 0.919 (red) results an almost triangular shape of the shear failure surface. One can see that the closer γ is from 0.5, the more circular is the shape of the shear failure surface. On the other hand, when γ increases, the shape becomes more triangular. At this stage, it is worth noting that the usual value for γ for concrete is equal to 0.864 which is very different. So far, no experimental data in the literature was available to estimate this value for rammed earth. Rammed earth results to be much less resistant along an extension path than concrete for a same compression strength.

5.1.3 Failure radius R_{fail}

Once $T_{r\,max}$ and γ parameters are identified, the failure radius can be determined by using the following criteria in shearing (Riyono, 2017):

$$R_{fail} = \sqrt{\frac{2}{3}\left(\frac{q^{fail}(1-\gamma)^{1/6}}{I_1^{fail} + 3T_{r\,max}}\right)} \tag{23}$$

where q^{fail} is the deviatoric stress at failure and I_1^{fail} is the first invariant of stress. In case of unconfined compression test, both q^{fail} and I^{fail} are equal to the maximum resistance under compression of the material.

Applying the expression above with the average results of unconfined compression tests, the parameter writes:

$$\boldsymbol{R_{fail} = 0.191} \tag{24}$$

This value obtained from the experiments is much smaller than that one used by Riyono (2017) for validation of CJS-RE model, which was equal to 0.37. That means that the maximum size of the yield surface before failure is much smaller than expected.

5.2 Identification of tensile failure surface

For the identification of the tensile failure surface, which is also the tensile yield surface, just one type of test is necessary. Brazilian (also called splitting) test allows to determine the tensile strength. As highlighted by Riyono (2017), the indirect tensile strength obtained by Brazilian test is slightly overestimated, mainly due to effects of the sample's size. The difference between unconfined tensile test and Brazilian test is that in this indirect method the failure surface is imposed, while in the direct tensile test the failure starts around local defects within the material.

Results of the three repeatability Brazilian tests which were carried out are: 40.1 KPa, 43.3 KPa and 48.6 KPa. The calculated average value is 44 KPa. It represents 6.3% of the average unconfined compressive strength, which is lower than results found from literature. In fact, this result agrees with

the low average dry density of the samples manufactured for this study. Since the dry density is low (lower compaction energy), there were more critical regions (where failure begins), thus, it was expected that the tensile strength of the samples would be lower as well. Figure 5.8 provides the type of failure by the Brazilian test on sample 78 (w=2%), which is perpendicular to the plane of the imposed load
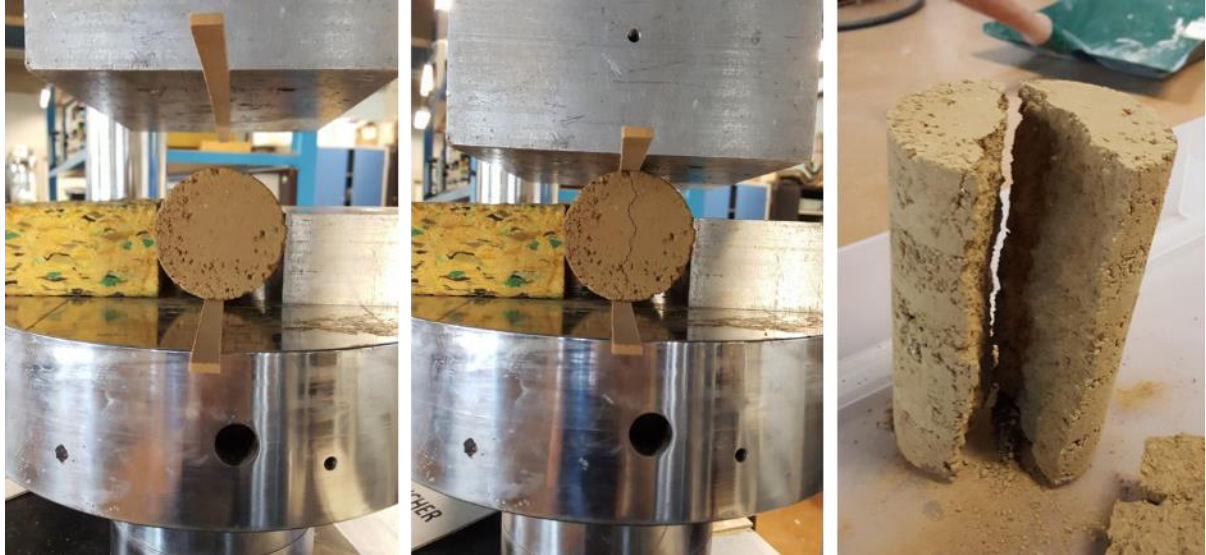
Figure 5.8 – Failure on the sample number 78 by carrying out Brazilian (splitting) test

In CJS-RE model, the parameter which allows to identify the tensile failure surface is T_r. It is equal to the uniaxial tensile resistance (f_t), and it graphically represents the initial point of the tensile failure envelop (where the second invariant of the deviatoric stress is equal to zero). Thus, the average tensile strength obtained is:

$$T_r = f_t = 44 \, KPa \tag{25}$$

Knowing the value of $3T_r$, which is the starting point of the line that describes the envelop of the tensile failure surface, is then possible to identify the second plastic failure surface. The second point of this line (brown line on Figure 5.9 in the extension region) is determined by assuming the tensile stress path for $I_1 = f_t$. Then, the triangle-relation is applied from where the second invariant of the deviatoric stress in this point is $S_{II} = \sqrt{2/3} \, I_1$. Thus, the second point is obtained and, finally, the tensile failure envelope is identified.
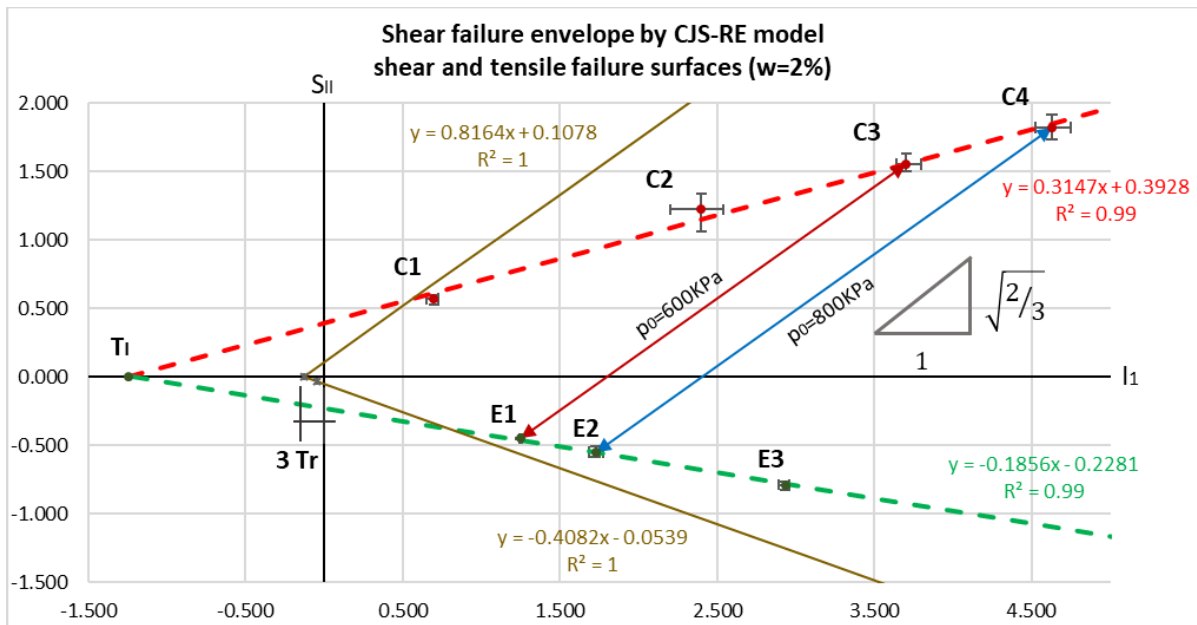
Figure 5.9 – Plastic shear and tensile failure surfaces

This tensile yield surface is similar to the maximum criterion of Rankine for brittle fracture in concrete (Riyono, 2017). As one can see, this tensile failure surface reduces the domain of acceptable stresses within the shear failure surface. The interception points between shear and tensile failure (in both compression and extension regions) shows that choosing the first confining pressure of 300 KPa for compression (point C1) and of 600 KPa for extension (point E1) were important so that the material stress path could effectively reach the shear and not the tensile failure surface. This is the reason why those first confining pressures were chosen.

6. STRESS-STRAIN RELATIONSHIP

The stress-strain relationship curves obtained by compression and extension tests allowed the maximum compressive strength for each specimen to be determined under these two stress paths. To build the stress-strain curves, data was extracted from the software connected to the triaxial tests, which provided the vertical displacements and the deviatoric loads. Knowing the geometrical properties of samples (70mm diam. and 140mm height), the deviatoric stresses and strains were then determined.

6.1 Compression stress-strain curves

Values of the maximum compressive strength were used to identify the shear failure surfaces, as presented in the previous chapter. In this section, they are also used to identify the Young's modulus (E) and the isotropic plastic hardening parameter (A) of CJS-RE model.

Here comes the opportunity to highlight that a correction process was applied on the compression stress-strain curves. The main reasons, common to many specimens, are described here for the sample number 33 (pre-existing builder sample), during a 600KPa confined compression test, which shows that:

a) for the first experiments, the position of the load cell was not well connected to the top of the sample, the reason why the initial displacements did not correspond to the behavior of rammed earth (region A from Figure 6.1). For other tests, more attention was given to this problem in order to reduce the influence of this lack of contact between load cell and sample;

b) even for tests with great initial contact between load cell and sample, the first set of displacements may not translate the correct behavior of rammed earth (region B from Figure 6.2). They may be related to the accommodation of the entire system (load cell + sample), including the plaster placed over and under specimens;

c) in case of confined compression tests, mainly those under high confining pressure (above 600 KPa), an apparently hardening behavior appeared after reaching the plastic state (region C from Figure 6.3). This is hardly the truth, because softening should happen according to other experiments from literature. Plus, the calculated stresses consider that the sample keep a constant sectional area during the entire test. In fact, most of samples showed high lateral displacements, thus, an increase of the sectional area while load was applied.

To reduce the effect of the third problem (region C), an equation was used to correct the sectional area of each step from the stress-strain curve. In cases when volumetric deformation is also measured, this correction is not necessary, since lateral and vertical displacements are directly provided. The follow equation is a rough simplification provided for sand, which gives for each step the sectional area in the middle height (S_i) of the sample:

$$S_i = \left(1 + \frac{3}{2}\varepsilon_i\right) \times S_0 \qquad (26)$$

where ε_i is the vertical strain which corresponds to the moment when the sectional area is calculated, and S_0 is the initial sectional area.
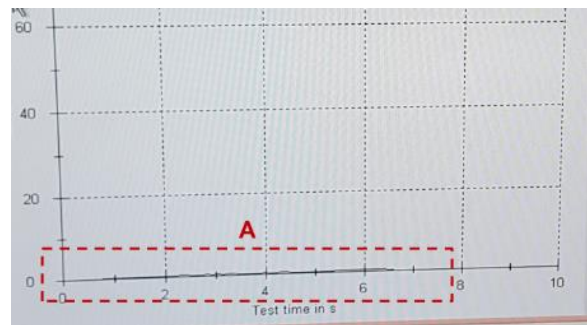
Figure 6.1 – Stress-strain relationship under compression – problem A
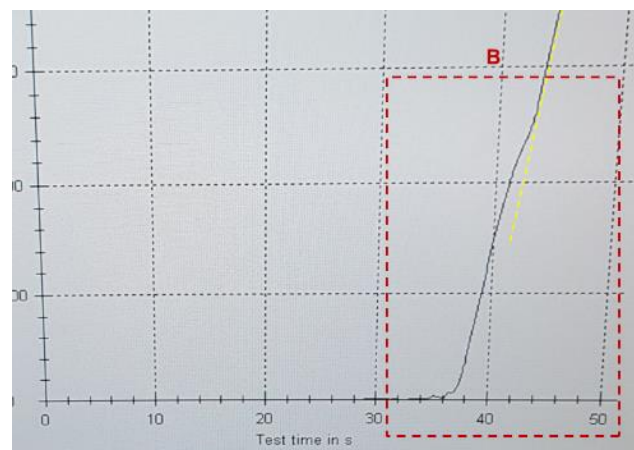
Figure 6.2 – Stress-strain relationship under compression – problem B
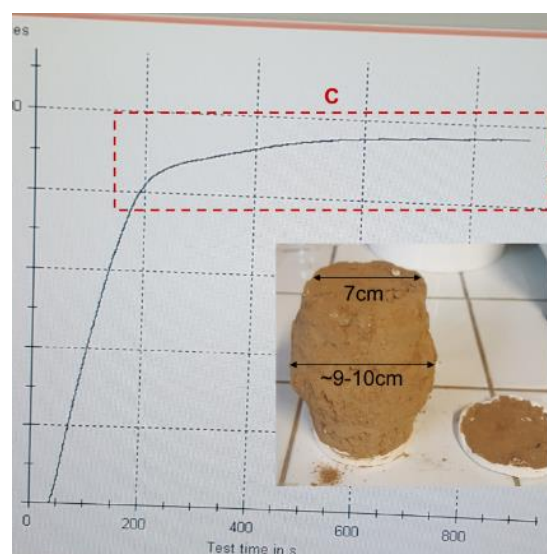
Figure 6.3 – Stress-strain relationship under compression – problem C

Important to say that, by using the corrected sectional area previously indicated, the maximum compression strength was also reduced. This lower value of f_c was the one chosen to allow the identification of the previous shear failure surface. To have a first analysis if the equation was reasonably suitable for these rammed earth experiments, the final diameter at the middle height was measured for some samples (~95 mm for sample 33) and compared to the calculated one (~85 mm for sample 33). It was observed, then, that the calculated sectional area is about 10% lower than the measured. This fact may not play an important role on the identification of elastic and plastic parameters, but could be confirmed by further research using sensors of lateral deformation.

According to CJS-RE, there are two elastic parameters to be identified. First is the elastic modulus (E), which was determined by the corrected stress-strain curves from compression tests. The second parameter, the Poisson ratio (ν), could not be identified in this work, since volumetric deformation was not measured. Though, a value of 0.25 was assumed extracted from other references.

Thus, the correction process previously described also contributes to better determine the value of E. To avoid the influence of the second problem (region B from Figure 6.2) and keep a standard procedure for comparison, the initial tangent value of E was considered in this work, but regarding a window of region generally between 20% and 30% of the maximum compressive strength (f_c). In some tests, this range was not the best region to obtain E, so other limits were used. The Young's modulus was estimated by the equation of a trend line built between three points inside that window. Figure 6.4 presents an example of original and corrected stress-strain curve, which has an E equal to 144 MPa.

Figure 6.4 – Example of original and corrected stress-strain curves

Values of the identified Young's modulus for each sample with w=2% is presented on Table 6.2. The average value of E is 153 MPa. Since no loading-unloading cycle was provided in this work, the identified value of E here presented is just a rough estimation, based on the previous correction process of curves.

Table 6.1: Identified average values of the Young modulus on rammed earth specimens

water content (w)	Test	Average dry density [kg/m³]	Maximum strength [MPa]	Young modulus [MPa]
	Unconfined compression	1637	0.70	127
	Confined compression 0.3 MPa	1637	1.50	179
2%	Confined compression 0.6 MPa	1637	1.90	143
	Confined compression 0.8 MPa	1698	2.23	162
			Average	**153**

Figure 6.5 gives the three repeatability tests of the unconfined compression test carried out for the manufactured samples with water content of 2%. These are the stress-strain relationship curves already corrected by the previous mentioned process. In this case, E varied from 108 MPa (test 12) to 144 MPa (test 7).
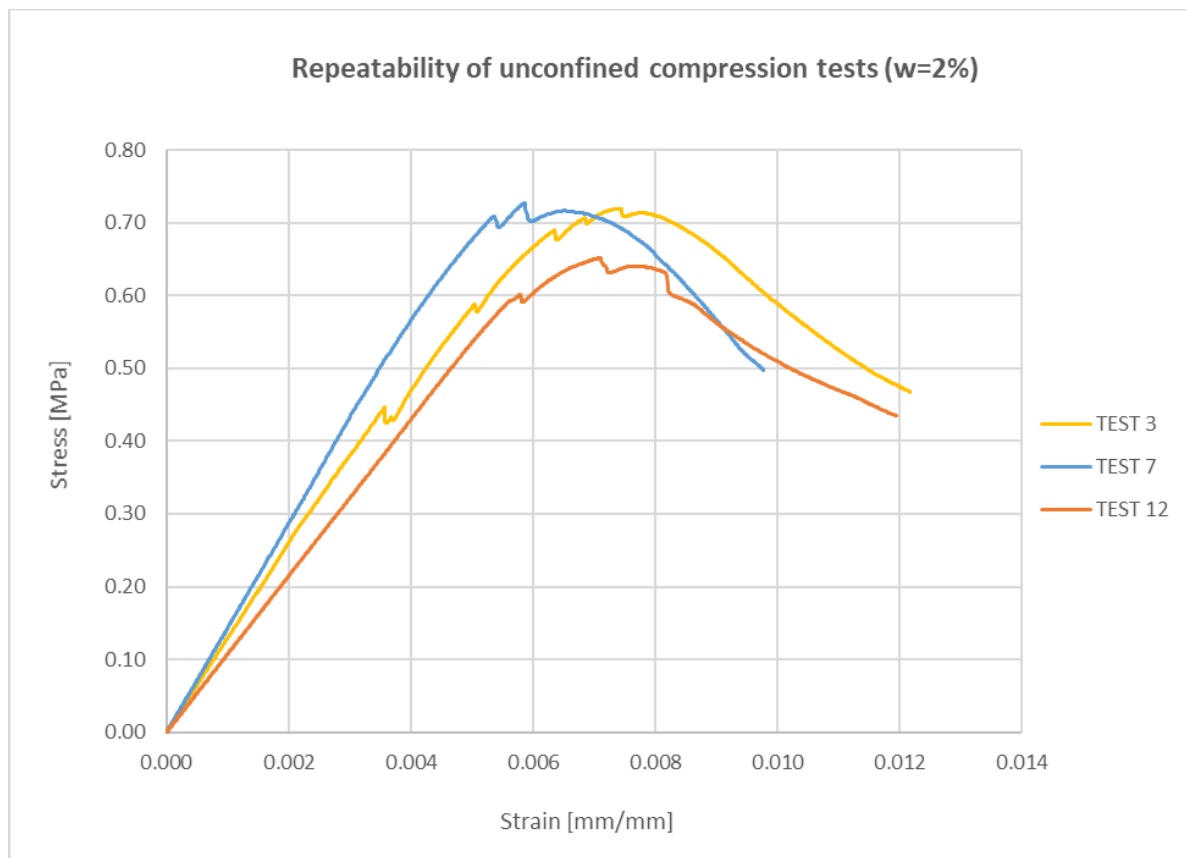
Figure 6.5 – Repeatability curves of the unconfined compression tests (w=2%)
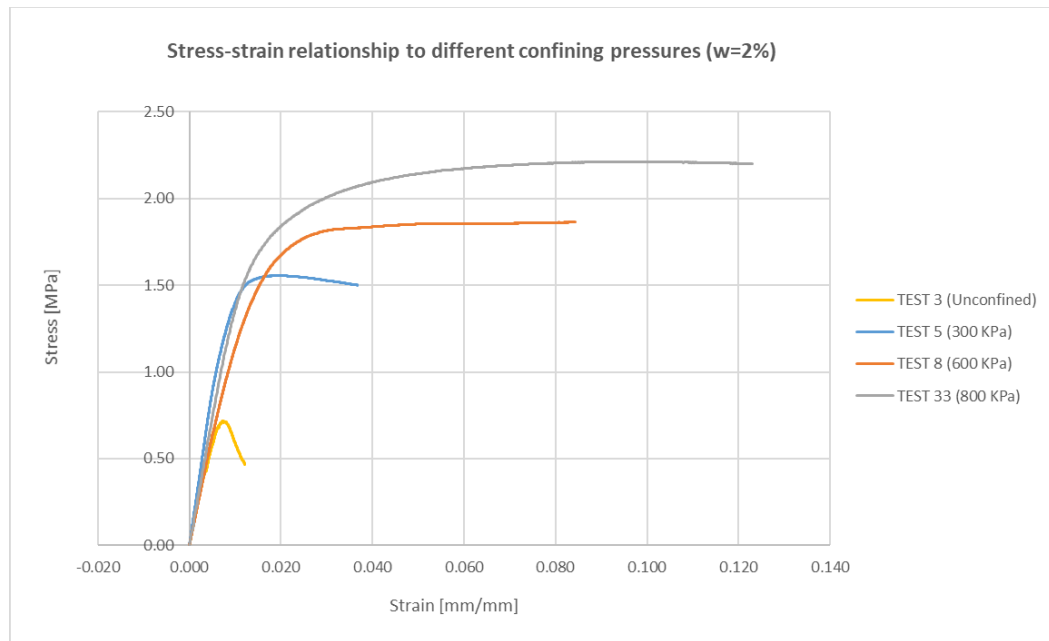
Figure 6.6 – Stress-strain curves to different confining pressures (w=2%)

Analyses of the stress-strain compression curves were also necessary to identify the value of R_{ini}. This is the initial yield radius, another parameter from CJS-RE, which describes the extent of the elastic domain (before the start of yield deformations). To evaluate the value of R_{ini}, a zoom window was taken during a compression test (test number 8) with 0.6 MPa of confining pressure on sample number 8 (Figure 6.7). The linear behavior is observed until when the triaxial test reaches a load of 2.4 kN, which is equal to, approximately, a stress of 0.6 MPa. Table AN 14 presents the maximum strength reached for all samples, and thus, one can see for test 8 this value was 1.87 MPa. In conclusion, 0.6 MPa represents 32% of the maximum strength (1.87 MPa). The same proportion is then observed between R_{fail} and R_{ini}, which agrees with the value proposed by Riyono (2017).
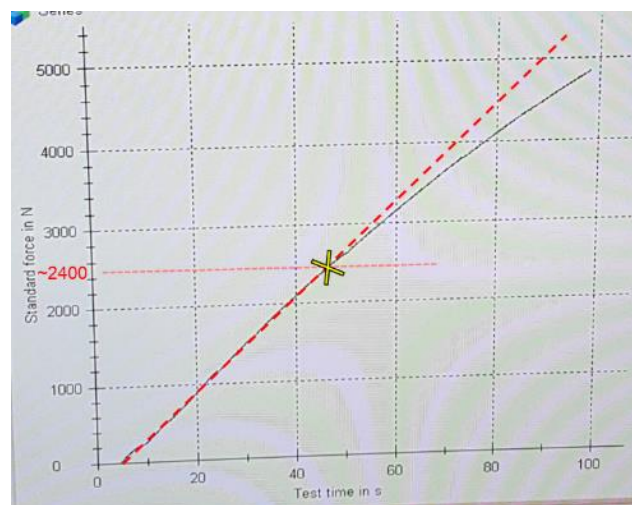
Figure 6.7 – Extent of the linear behavior during compression test on sample 8 (w=2%)

Finally, the value of initial yield radius is taken as:

$$R_{ini} = 30\% \, R_{fail} = 0.06 \tag{27}$$

6.2 Extension stress-strain curves

As presented in the previous chapter, values of the maximum strength under extension load were used to identify the dissymmetry parameter of the shear failure surface. A great repeatability of extension tests was observed for some tests. Figure 6.8 and Figure 6.9 provide the three repeatability curves from extension tests with, respectively, 0.6 MPa and 1.3 MPa.
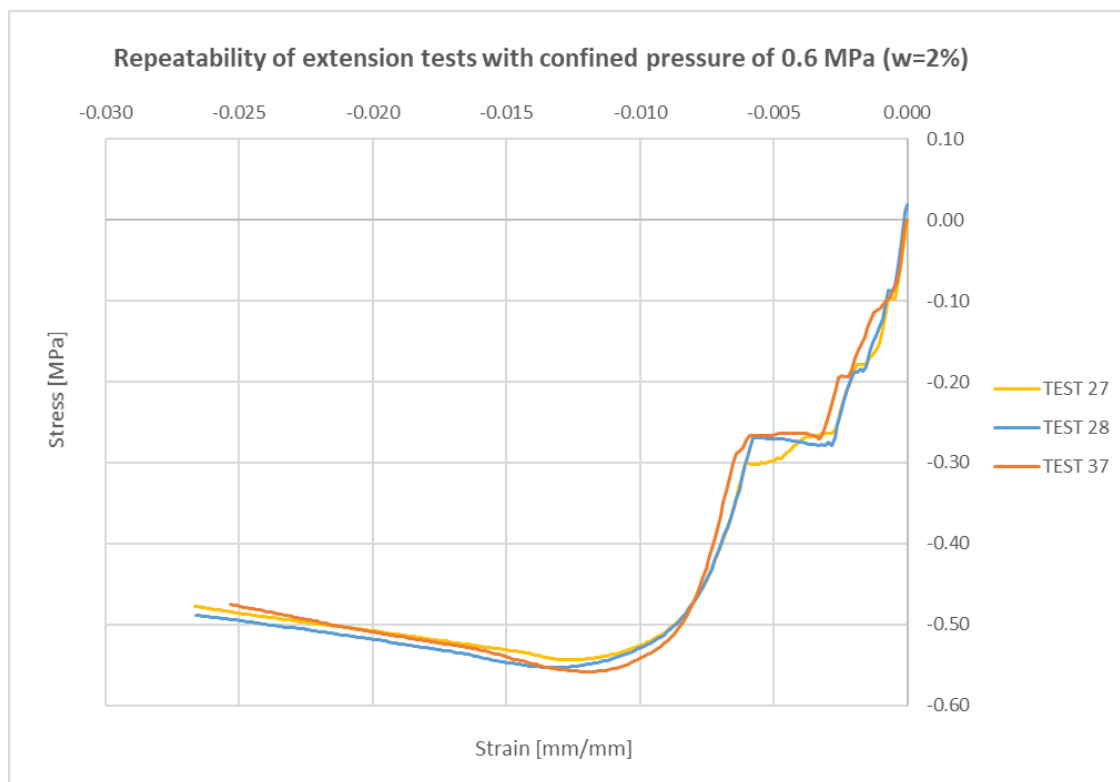
Figure 6.8 – Repeatability curves of the 0.6 MPa extension tests (w=2%)

One can observe the curves had a similar behavior, such as a plateau, close to a stress of 0.25 MPa. This was also observed for other confining pressures. First, a possible explanation was that in this range a certain accommodation of the sample began, especially between layers. A second reason could be the interference of the plaster (bottom and top). In fact, the second point seemed to interfere more, because the interconnection between two different materials (earth and plaster) may be not as strong as those between layers.

To evaluate this hypothesis, one sample without plaster (test 24) was tested for extension and the curve is given in Figure 6.9. First characteristic to observe is that the sample without plaster had an initial

extension load applied (close to 0.23 MPa), maybe due to the lack of initial configuration of the triaxial. Results showed that this sample without plaster behaved more uniformly during the first displacements (strains), which can indicate that the plaster had a significant impact on the stress-strain relationship. Further studies can focus a deep analysis on this feature, including the effects on compression tests.
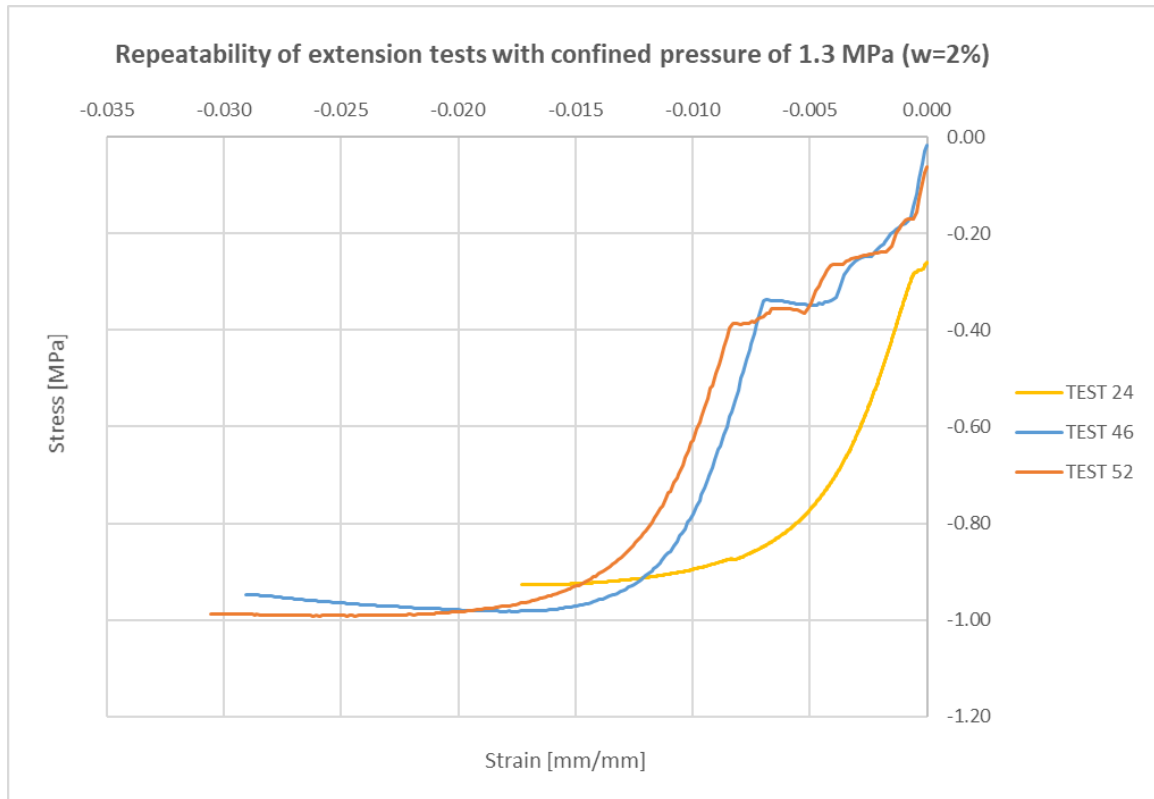
Figure 6.9 – Repeatability curves of the 1.3 MPa extension tests (w=2%)

6.3   Comparison between experimental stress-strain curves and CJS-RE model

Finally, using the previous identified plastic parameters from chapter 5, a comparison is evaluated between the stress-strain relationship obtained by the tests and the one provided by CJS-RE model. A trial-and-error method using CJS-RE was taken to identify the isotropic plastic hardening parameter (A) and the softening of the plastic shear failure (α_s).

To evaluate the values of A and α_s, the trial-and-error method was applied first on results from the unconfined compression tests. Thus, the average values among unconfined tests were used as input in CJS-RE. However, for comparison, just one curve was selected in order to provide a clearer view of the behavior, which is more interesting for comparison.

Table 6.2 reviews the stated and the identified parameters used to build the stress-strain curves with the first hierarchical level CJS-RE1. Similarly,

Table 6.3 gives those parameters related to CJS-RE2. Important to observe that the value of the Young's modulus (E = 127 MPa) considers just the average among unconfined compression results.

Table 6.2: Identified and stated model parameters for CJS-RE1 model based on this study

Elastic		Plastic	
E	= 127 MPa (identified)	β	= 1.0 (stated – no information about volumetric deformations)
υ	= 0,25 MPa (stated)	γ	= 0.919 (identified – shear failure)
		R_{fail}	= 0.191 (identified – shear failure)
		$T_{r\,max}$	= 416 kPa (identified – shear failure)
		T_r	= 44 kPa (identified – tensile failure)
		α_t	= -1.0 (stated as default)

Table 6.3: Identified and stated model parameters for CJS-RE2 model based on this study

Elastic		Plastic	
E	= 127 MPa (identified)	β	= 1.0 (stated – no information about volumetric deformations)
υ	= 0,25 MPa (stated)	γ	= 0.919 (identified – shear failure)
		R_{fail}	= 0.191 (identified – shear failure)
		R_{ini}	= 0.06 (identified – stress-strain compression curve)
		$T_{r\,max}$	= 416 kPa (identified – shear failure)
		T_r^{ini}	= 44 kPa (identified – tensile failure)
		A	= 0.00052 (identified – trial-and-error method using CJS-RE)
		α_s	= -0.0013 (identified – trial-and-error method using CJS-RE)
		$T_{r\,max}^{res}$	= 83 kPa (stated to be 20% of $T_{r\,max}^{ini}$)
		α_t	= -0.5 (stated to give a gradual softening)

Comparison between experiments and CJS-RE model is provided by Figure 6.10, which indicate the curve for an unconfined compression test. The interesting fact about CJS-RE is that this model automatically includes the increase of maximum strength which follows the increase of confining pressures.
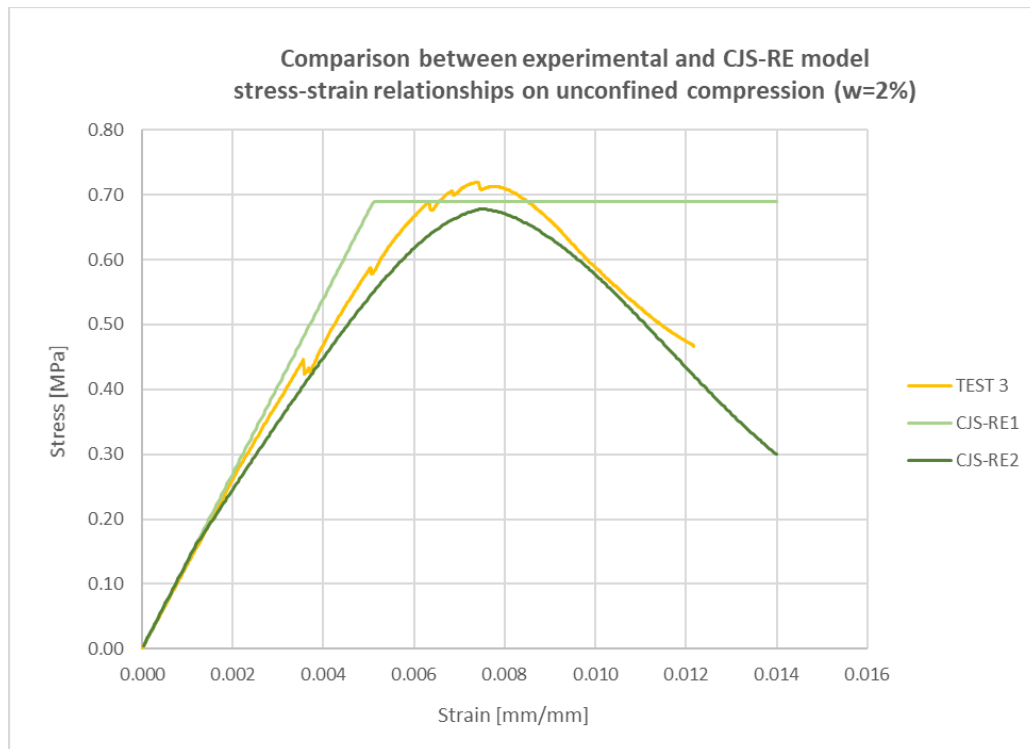
Figure 6.10 – CJS-RE1 and CJS-RE2 stress-strain relationship of test 3 unconfined compression test (w=2%)

The maximum compressive strength, for unconfined compression test, was almost the same for both tested and the modelled stress-strain relationship. Results from confined compressions tests were not presented here for two reasons.

First, with high confining pressures, the maximum strength provided by CJS-RE did not follow that one resulted by experimental tests. About the model, this can be related with the identification of R_{fail}. About the experiments, it is possibly related to the fact that the samples did not have a constant sectional area during load, so the stresses could be even smaller, and thus softening maybe could be observed. Secondly, on rammed earth, softening could be influenced by the increase of confining pressure, which could explain why most of the samples behaved so differently from the model from high confining pressures.

7. INFLUENCE OF WATER CONTENT

Water plays an important role on the structural behavior of rammed earth material. Clay particles within the soil act as a bond in the presence of a certain amount of water, providing cohesion between particles. The mechanical strength of rammed earth structures comes with time, when most of the water has left the porous network of the material.

Thus, controlling the water content on rammed earth during and after the manufacturing process is from great importance to optimize its mechanical behavior. The increase of moisture content after construction destroys the capillary forces and can lead to a strong decrease of the shear resistance of the material. The effect of an increase of the water content is clearly observed by Figure 7.1, from which one can see that the maximum compressive strength and the Young's modulus both decreased.
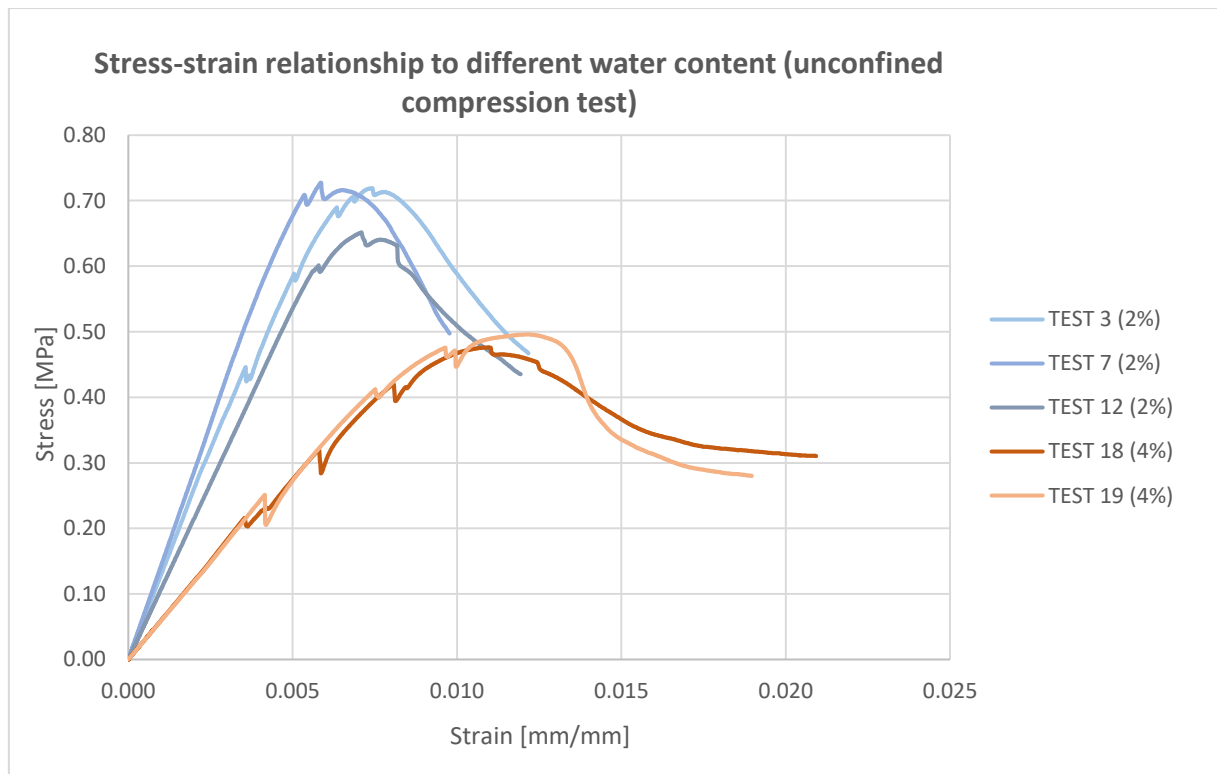
Figure 7.1 – Comparison between behavior of samples with w=2% and w=4% tested by unconfined compression

This chapter explores, then, the influence of water content on the plastic failure surfaces of rammed earth. Results for the first dry state (w=2%) was already presented on chapter 5. Now, a comparison is provided regarding a state with higher water content (w=4%). Figure 7.2 gives all information regarding

the failure surfaces from tests on samples with w=4%. Then, the associated parameters can be compared.
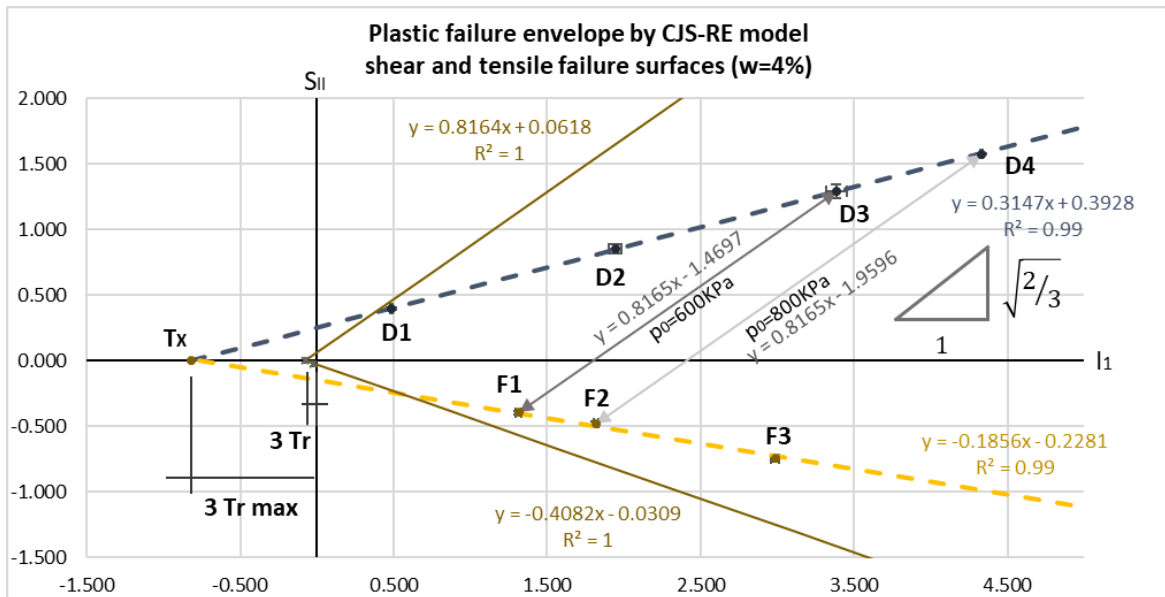
Figure 7.2 – Plastic failure surfaces by CJS-RE model (w=4%)

Figure 7.3 gives the shear failure surface for both studied water contents. One important point to observe is that the value of the maximum tensile resistance ($T_{r\,max}$) greatly reduced. But, the most important difference is that the shear failure surface from w=4% in compression reduced more than the shear failure surface in extension. It means that γ, which means the dissymmetry between shear failure surface in compression and extension, have decreased.
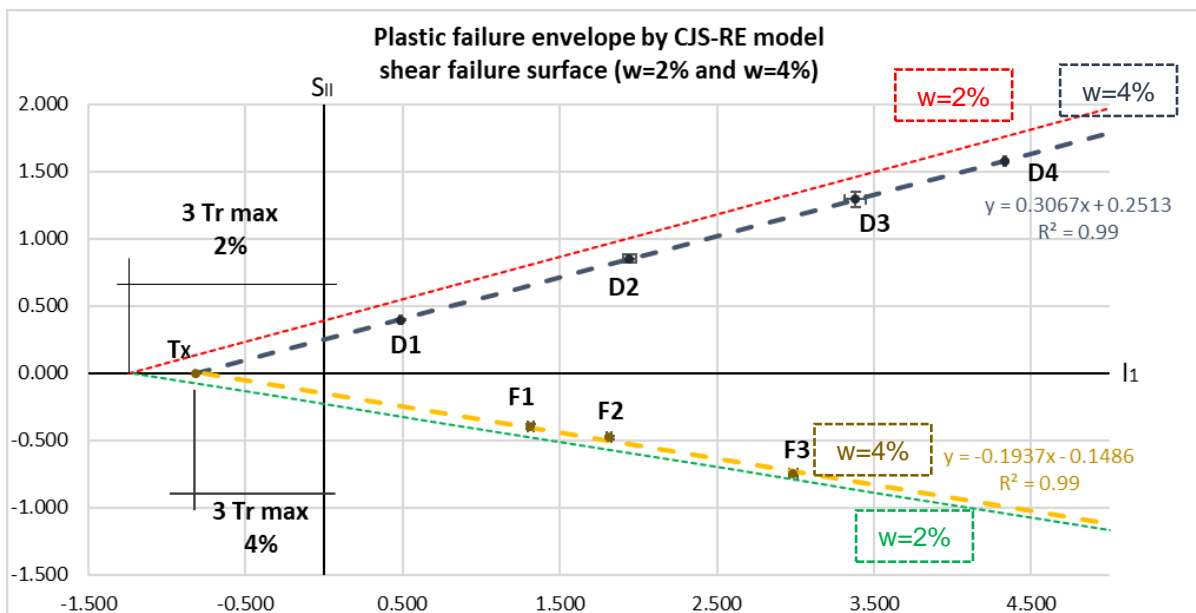
Figure 7.3 – Shear failure surfaces by CJS-RE model with w=4% compared to w=2%

The analysis of the differences between the plastic tensile failure surfaces for w=2% and w=4% is give by Figure 7.4. Rammed earth has already a very low resistance to tensile stresses, though, such changes on the tensile failure surface are difficult to perceive graphically.
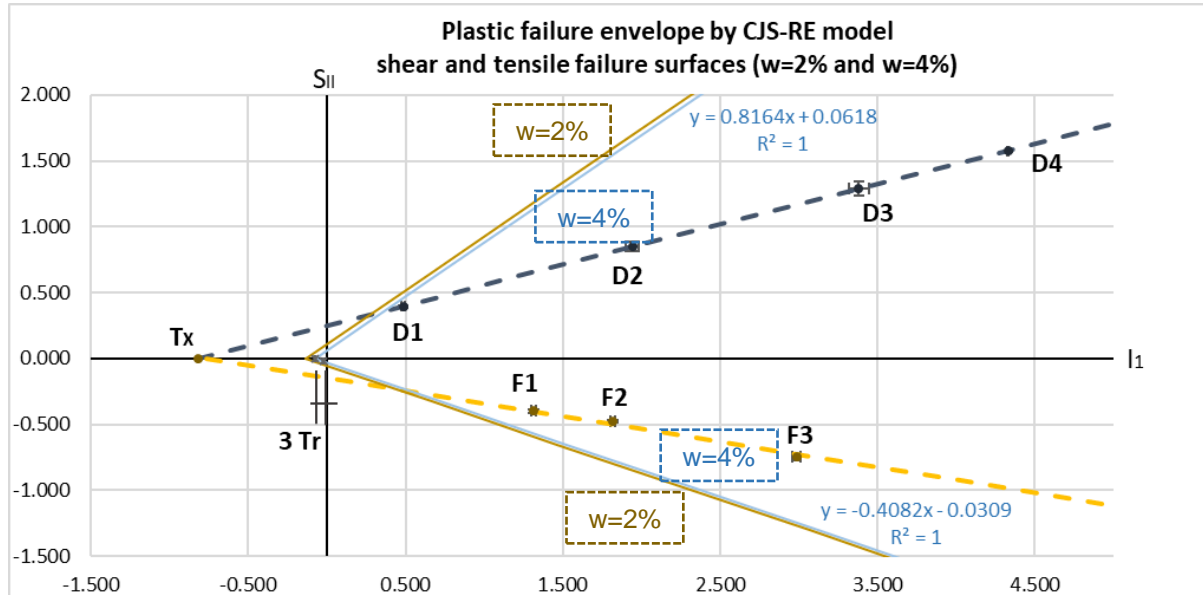
Figure 7.4 – Tensile failure surfaces by CJS-RE model with w=4% compared to w=2%

Table 7.1: Identified and stated model parameters for CJS-RE1 model based on this studyTable 7.1 briefly reviews the parameters obtained by experiments on samples with w=2% and indicates the differences with those with w=4%. Most values of these parameters had a decreased behavior, as expected, since they are related to the strength of the material (E, fc, $T_{r\,max}$, T_r).

Table 7.1: Identified and stated model parameters for CJS-RE1 model based on this study

Parameter	w=2% (i)	w=4% (ii)	% difference (ii-i)/(i)
E (average)	154 MPa	98 MPa	-36%
f_c unconfined (average)	699 KPa	486 KPa	-30%
$T_{r\,max}$	416 KPa	273 KPa	-34%
γ	0.919	0.895	-3%
R_{fail}	0.193	0.209	8%
$T_r = f_t$ Brazilian (average)	44 KPa	25 KPa	-43%

As a final comparison, the fact that the dissymmetry reduced following the increase of water content shows that, for rammed earth, water affects much more the behavior in a compression stress path than

an extension. The increase of R_{fail} is related with changes of γ and T_r, and apparently it slightly increases with water content.

8.   CONCLUSION

In this work, an evaluation of the mechanical behavior of rammed earth has been presented based on a set of tests under different stress paths, such as compression, extension and tensile. Results from samples with a water content of 2%, achieved after natural dry period, were used to build two plastic mechanisms of deformation. These plastic failure surfaces proposed by CJS-RE model were then identified. First, the shear failure surface associated to purely deviatoric stresses was determined and, after, the tensile failure surface. Additionally, tests on samples with a water content of 4% were also evaluated, and a comparison was provided.

Taking into account the need of understanding the material and procedures, a first step is to analyze the soil properties, such as the mineral composition and sensitivity to water. This information helps to define if such soil is suitable for rammed earth technique or if it should be corrected, by adding clay content, for example. Good results were obtained by methylene blue tests, which indicated a soil with a Methylene Blue Value (MetBV) of 1.5. This value indicates the soil has some sensitivity to water due to the presence of clay.

Since the manufacturing process of the first samples, the compaction effort proved to be very important so the material could reach a proper strength. Many samples broke during different phases of the development of this work. Most of them broke when demolding, or enveloping by the membranes, or when plaster was added. The specimens submitted to an increase of water content broke even much more easily, the reason why just two repeatability tests were performed for this studied water content. These problems could be related to the low compaction energy provided, since samples were manufactured using a manual rammer. Plus, the dry density, which is related to the compaction energy, is clearly an important parameter to be analyzed. The average dry density of the manufactured samples was lower than values from literature.

Even though soil is a very heterogeneous material, this study showed a considerably good repeatability regarding the experimental results, with some exceptions. The optimum water content during manufacturing was difficult to control, and thus different dry densities were achieved. Despite that, results were still satisfactory.

The model CJS-RE confirmed a very good approach to describe the stress-strain curve of rammed earth material under unconfined compression tests. The identified elastic and plastic parameters allowed to describe the behavior of rammed earth with strong reliability. Thus, by requiring few parameters, it is a great source for design and maintenance of rammed earth structures. When compared to confined compression tests, keeping the same identified parameters for the unconfined compression test, CJS-RE showed a small difference comparing to the stress-strain relationship experimentally obtained. Further analysis was not made, since the curves obtained by the triaxial device with high confining

pressures showed a hardening behavior, which probably does not represent the real situation. Even after applying a correction process on the stresses, softening was almost indistinguishable in several tests.

Regarding the evaluated parameters, the most important conclusion is that a very strong dissymmetry between compression and extension stress paths of the shear failure surface was observed. The experimental results showed a very high value of γ (the dissymmetry parameter of the shear failure surface), which indicates that rammed earth behaves considerably different in shear under compression and extension. The other identified parameters for the shear failure surface were the maximum tensile strength ($T_{r\,max}$) and the radius at failure (R_{fail}).

Additionally, this work stated a first analysis for evaluating the influence of the water content on the mechanical behavior of rammed earth. Results indicated that most of parameters (E, f_c, $T_{r\,max}$ and T_r), decreased about 30%-40% with an increase of 2% of water content. The dissymmetry parameter (γ) showed a small decrease in its value, which means that dissymmetry slightly reduces with the increase of water content. This happened because, by increasing the water content, the loss of strength was higher in compression stress path than extension. On the other hand, R_{fail} was the only parameter which has increased (difference of 8%) by changing the water content from 2% to 4%.

Finally, this work provided a new set of experiments which are certainly important for the understanding of rammed earth behavior, but as well as important to contribute as a new validation process of CJS-RE. From the observed literature, there are not references for extension tests carried out on rammed earth, which brings the central relevance of this work.

PROSPECTS:

As prospects for further researches, evaluate other different ranges of water content is of great necessity, in order confirm if keeps the pattern observed within this proposed study. Plus, more tests could be performed for the water content of 4% to obtain the third set of three repeatability tests, since this work just provided two sets for this studied water content. There is also a need to develop more tests for samples with higher dry density and its possible influence on the behavior of the plastic failures surfaces.

For next tests, the use of sensors which measure the volumetric deformation is of great importance, especially to evaluate lateral deformations. This will allow to build more precisely the stress-strain relationship curves for rammed earth.

Finally, carrying out compression tests with loading and unloading cycles are suggested in order to better determine the Young modulus. Extension tests on samples without plaster is also a possible prospect for new studies, to also evaluate the Young modulus for these types of test.

REFERENCES

Allinson, D. and Hall, M. (2010) 'Hygrothermal analysis of a stabilised rammed earth test building in the UK', *Energy and Buildings*. Elsevier B.V., 42(6), pp. 845–852. doi: 10.1016/j.enbuild.2009.12.005.

Araki, H., Koseki, J. and Sato, T. (2016) 'Tensile strength of compacted rammed earth materials', *Soils and Foundations*. Elsevier, 56(2), pp. 189–204. doi: 10.1016/j.sandf.2016.02.003.

British Standard (2002) 'BS 1377-4 - Methods of test for Soils for civil engineering purposes - part 4: Compaction related tests', *British Standard*, 3(December).

Bui, Q. B. and Morel, J. C. (2009) 'Assessing the anisotropy of rammed earth', *Construction and Building Materials*. Elsevier Ltd, 23(9), pp. 3005–3011. doi: 10.1016/j.conbuildmat.2009.04.011.

Bui, Q. B., Morel, J. C., Hans, S. and Meunier, N. (2008) 'Compression behaviour of non-industrial materials in civil engineering by three scale experiments: the case of rammed earth', *Materials and Structures*, 42(8), pp. 1101–1116. doi: 10.1617/s11527-008-9446-y.

Bui, Q. B., Morel, J. C., Hans, S. and Walker, P. (2014) 'Effect of moisture content on the mechanical characteristics of rammed earth', *Construction and Building Materials*. Elsevier Ltd, 54, pp. 163–169. doi: 10.1016/j.conbuildmat.2013.12.067.

Bui, Q. B., Morel, J. C., Venkatarama Reddy, B. V. and Ghayad, W. (2009) 'Durability of rammed earth walls exposed for 20 years to natural weathering', *Building and Environment*. Elsevier Ltd, 44(5), pp. 912–919. doi: 10.1016/j.buildenv.2008.07.001.

Bui, T. T., Bui, Q. B., Limam, A. and Maximilien, S. (2014) 'Failure of rammed earth walls: From observations to quantifications', *Construction and Building Materials*, 51, pp. 295–302. doi: 10.1016/j.conbuildmat.2013.10.053.

Bui, T. T., Bui, Q. B., Limam, A. and Morel, J. C. (2016) 'Modeling rammed earth wall using discrete element method', *Continuum Mechanics and Thermodynamics*, 28(1–2), pp. 523–538. doi: 10.1007/s00161-015-0460-3.

Cambou, B. and Jafari, K. (1988) 'Modèle de comportement des sols non cohérents', *Revue Française de Géotechnique*, 44, pp. 43–55. Available at: http://www.geotech-fr.org/sites/default/files/rfg/article/44-4.pdf.

Champiré, F., Fabbri, A., Morel, J. C., Wong, H. and McGregor, F. (2016) 'Impact of relative humidity on the mechanical behavior of compacted earth as a building material', *Construction and Building Materials*, 110(May), pp. 70–78. doi: 10.1016/j.conbuildmat.2016.01.027.

Costanza, R. (1979) *Embodied Energy Basis for Economic-Ecologic Systems*. University of Florida. Available at: http://ufdc.ufl.edu/UF00089540/00001/1.

D'Monte, R. (2009) *Types of Earth Construction*, *SDM Architects*. Available at: http://www.sdmarchitects.com/written-by-sdm--rsdm.html (Accessed: 24 May 2017).

Guerrero Baca, L. F. (2006) 'Una Cultura Constructiva', *Apuntes*, 20, pp. 182–201.

Hall, M. and Djerbib, Y. (2004) 'Rammed earth sample production: Context, recommendations and consistency', *Construction and Building Materials*, 18(4), pp. 281–286. doi: 10.1016/j.conbuildmat.2003.11.001.

ICOMOS (2016) *International Council on Monuments and Sites - Documentation Center*, *ICOMOS publications - Catalogue 2016-2017*. Available at: http://www.icomos.org/en/documentation-center/7842-icomos-publications-catalogue-2016 (Accessed: 17 June 2017).

International Organization for Standardization (2002) *ISO 14688-1: Geotechnical investigation and testing - Identification and classification of soil - Part 1: Identification and description*. Geneva: International Organization for Standardization.

ISCARSAH (2014) *International Scientific Committee on the Analysis and Restoration of Structures of Architectural Heritage - Documents*, *ISCARSAH Documents*. Available at: https://iscarsah.org/documents/ (Accessed: 17 June 2017).

Jaquin, P. A. (2008) *Analysis of historic rammed earth construction*. Durham University. Available at: http://etheses.dur.ac.uk/2169/.

Jaquin, P. A., Augarde, C. E., Gallipoli, D., Toll, D. G. and Note, T. (2009) 'The strength of unstabilised rammed earth materials', *Géotechnique*, 59(5), pp. 487–490. doi: 10.1680/geot.2007.00129.

Librici, C. (2016) *Modelling of the seismic performance of a rammed earth building*. Universidade do Minho.

Likos, W. J. and Lu, N. (2003) 'Automated humidity system for measuring total suction characteristics of clay', *Geotechnical Testing Journal*, 26(2), pp. 179–190. doi: 10.1520/GTJ11321J.

Maniatidis, V. and Walker, P. (2003) 'A review of rammed earth construction', *Developing rammed earth for UK housing*, (May), p. 109. Available at: http://staff.bath.ac.uk/abspw/rammedearth/review.pdf.

Maniatidis, V. and Walker, P. (2008) 'Structural Capacity of Rammed Earth in Compression', *Journal of Materials in civil engineering*, 20(3), pp. 230–239. doi: 10.1061/(ASCE)0899-1561(2008)20:3(230).

Martínez, O. D. (2015) 'Preservation and repair of rammed earth constructions', pp. 1–103.

Miccoli, L., Drougkas, A. and Müller, U. (2016) 'In-plane behaviour of rammed earth under cyclic loading: Experimental testing and finite element modelling', *Engineering Structures*. Elsevier Ltd, 125, pp. 144–152. doi: 10.1016/j.engstruct.2016.07.010.

Miccoli, L., Müller, U. and Fontana, P. (2014) 'Mechanical behaviour of earthen materials: A comparison between earth block masonry, rammed earth and cob', *Construction and Building*

Materials. Elsevier Ltd, 61, pp. 327–339. doi: 10.1016/j.conbuildmat.2014.03.009.

Morel, J. C. (2013) *PRIMATERRE - Sustainable renovation and building: the challenge of local materials*. Available at: http://www.agence-nationale-recherche.fr/?Project=ANR-12-VBDU-0001 (Accessed: 29 May 2017).

Morel, J. C., Mesbah, A., Oggero, M. and Walker, P. (2001) 'Building houses with local materials: Means to drastically reduce the environmental impact of construction', *Building and Environment*, 36(10), pp. 1119–1126. doi: 10.1016/S0360-1323(00)00054-8.

Mužíková, B., Otcovská, T. and Padevět, P. (2017) 'Water Absorption Properties of Rammed Earth Material with Montmorillonite Clay', *55th Conference on experimental stress analysis*.

Norme Française (1993) *NF P 94-068 - Sols: reconnaissance et essais - mesure de la quantité et de l'activité de la fraction argileuse - détermination de la valeur de bleu de méthylene d'un sol par l'essai à la tache*. Edited by AFNOR. AFNOR.

Otcovská, T., Mužíková, B. and Padevět, P. (2017) 'Usage of Illite-kaolinitic Clay for Rammed Earth Manufacturing and Its Drying Rate', *55th Conference on experimental stress analysis*. Vysoké Tatry, Slovakia.

Otcovská, T. and Padevět, P. (2016) 'Dependence of compressive strength of rammed earth on used clay composition', *EAN 2016 - 54th International Conference on Experimental Stress Analysis*, pp. 1–4.

Otcovská, T. and Padevět, P. (2017) 'Dependence of Tensile Bending Strength of Rammed Earth on Used Clay Composition and Amount of Mixture Water', in *Advanced Materials Research - Modern Methods of Experimental and Computational Investigations in Area of Construction II*. Prague, Czech Republic: Trans Tech Publications, Switerzland, pp. 48–53. doi: 10.4028/www.scientific.net/AMR.1144.48.

Riyono, W. A. (2017) *CJS-RE: A hierarchical constitutive model for rammed earth*. Ecole Centrale de Lyon.

Riyono, W. A., Vincens, E. and Plassiard, J.-P. (2017) 'A Hierarchical Constitutive Model for Rammed Earth A Hierarchical Constitutive Model for Rammed Earth', *Journal of Construction and Building Materials (preprint)*, (October), pp. 1–41. doi: 10.13140/RG.2.2.35328.84481.

RockMechs - Rock Mechanics for Engineers (2011) *Deviatoric stress and invariants*. Available at: http://www.rockmechs.com/stress-strain/stress/deviatoric-stress-and-invariants/ (Accessed: 23 June 2017).

Schroeder, H. (2011) 'La transferencia de humedad y el cambio en la resistencia durante la construcción de edificios de tierra.', *Moisture transfer and change in strength during the construction of earthen buildings.*, 63(523), pp. 107–116. doi: 10.3989/ic.10.023.

Sebastián, E. and Cultrone, G. (2010) 'Technology of Rammed-Earth Constructions ("Tapial") in Andalusia (Spain): Their Restoration and Conservation', in M. Bostenaru Dan; R. Poikryl; A. Török (ed.) *Materials, Technologies and Practice in Historic Heritage Structures*. Springer, pp. 11–28. doi: 10.1007/978-90-481-2684-2.

Sétra (2007) 'Guide technique - Design and execution of earthworks - Section 3: test procedures'. Available at: www.setra.equipement.gouv.fr.

Silva, R. a., Oliveira, D. V., Miranda, T., Escobar, C. and Cristelo, N. (2012) 'Rammed earth: Feasibility of a global concept applied locally', *13º Congresso Nacional de Geotecnia*. doi: Cd-rom.

Silva, R. A., Oliveira, D. V, Schueremans, L., Lourenço, P. B. and Miranda, T. (2014) 'Modelling the Structural Behaviour of Rammed Earth Components', *Twelfth International Conference on Computational Structures Technology*, pp. 1–13. doi: 10.4203/ccp.106.112.

Soria, F. J., Guerrero, L. F. and García, A. B. (2011) 'Traditional rammed earth construction: Conservation of built heritage in México', *WIT Transactions on the Built Environment*, 118, pp. 497–506. doi: 10.2495/STR110411.

Syrová, Z. and Syrový, J. (2012) 'Rammed earth in Moravia (Czech Republic) in the context of neighboring lands', *Rammed Earth Conservation*, pp. 229–235.

Valde, B. (2008) 'Clay Minerals', in *Terra literature review- an overview of research in earthen architecture conservation*, pp. 1–7.

Verhoef, P. N. W. (1992) *The Methylene Blue adsorption test applied to geomaterials*. Delft. Available at: http://publicaties.minienm.nl/documenten/the-methylene-blue-adsorption-test-applied-to-geomaterials.

Žabičková, I., Otcovská, T. and Padevĕt, P. (2016) 'Compressive Strength of Unburned Clay Masonry', in Padevĕt, P. (ed.) *Modern Methods of Experimental and Computational Investigations in Area of Construction*. softcover. Prague, Czech Republic, pp. 31–34. doi: 10.4028/www.scientific.net/AMM.825.31.

APPENDIX A – Triaxial testing description

This appendix provides better detail about the procedures of the triaxial tests carried out within this work. Compression and extension tests were performed using the Triaxial Automated System (GDSTAS) from GDS Instruments (Figure AN 1 – a). It is a load frame-based triaxial testing system, mainly composed by:

a) a control panel with: load frame, load cell and back pressure (Figure AN 1 – b);

b) the cell, where the sample is set inside, with a LVDT transducers to measure vertical displacements (Figure AN 1 – c);

c) a computer system with an automated controlled software to manage data acquisition (Figure AN 1 – d);

d) pressure controller, when necessary. For this, a hydraulic system (Figure AN 2 – a) was used mainly for tests under lower confining pressure (0.3 and 0.6 MPa). In other cases, an advanced pressure controller (Figure AN 2 – b) was rather adopted, since it had a better pressure capacity.

| (a) | (b) | (c) | (d) |
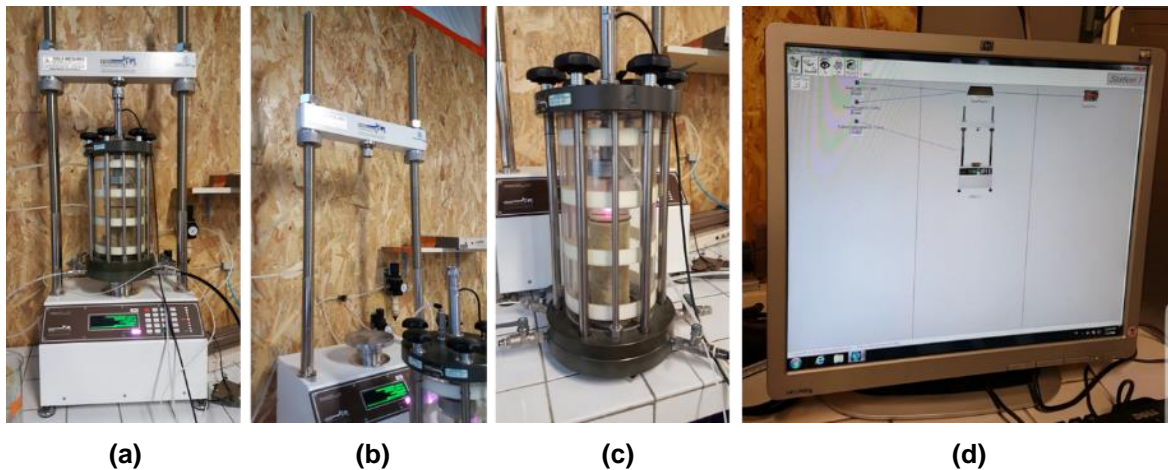
Figure AN 1 – Components of the load triaxial testing system GDSTAS

| (a) | (b) |

Figure AN 2 – Hydraulic (a) and advanced (b) pressure controller systems

APPENDIX B – Step-results of Methylene Blue Tests

Figure AN 3 and Table AN 2 indicate the MetBT process and results of each step from the first approach test. The MetBV obtained is 0.64 (Table AN 1).

Table AN 1: MetBV result of the first approach test

First Approach	Mass of soil (m) [g]	MetB volume (V) [mL]	MetBV (m / V) [-]
	76.7	120	**0.64**

Figure AN 3 – Drops of the Methylene Blue Test with 76.7 g of soil

Table AN 2: Methylene Blue Test results for the first approach with 76.7 g of soil

Reference	Methylene Blue added volume [mL]	Methylene Blue accumulated volume [mL]	Test result	Zoom of the final positive test
a	0	0	-	
b	15	15	Negative	
c	15	30	Negative	
d	20	50	Negative	
e	30	80	Negative	
f	20	100	Negative	
g	20	120	Positive	
h	-	120+1'	Positive	
i	-	120+2'	Positive	
j	-	120+3'	Positive	
k	-	120+4'	Positive	

Figure AN 4 to Figure AN 6 and Table AN 4 indicate the MetBT process and results of each step from test 1. In this case, the MetBV obtained is 0.73 (Table AN 3).

Table AN 3: MetBV result of test 1

First Approach	Mass of soil (m) [g]	MetB volume (V) [mL]	MetBV (m / V) [-]
	32.9	45	**0.73**

Figure AN 4 – Drops of the Methylene Blue Test with 32.9 g of soil (test 1, part 1)

Figure AN 5 – Drops of the Methylene Blue Test with 32.9 g of soil (test 1, part 2)

Figure AN 6 – Drops of the Methylene Blue Test with 32.9 g of soil (test 1, part 3)

Table AN 4: Methylene Blue Test results for the test 1 with 32.9 g of soil

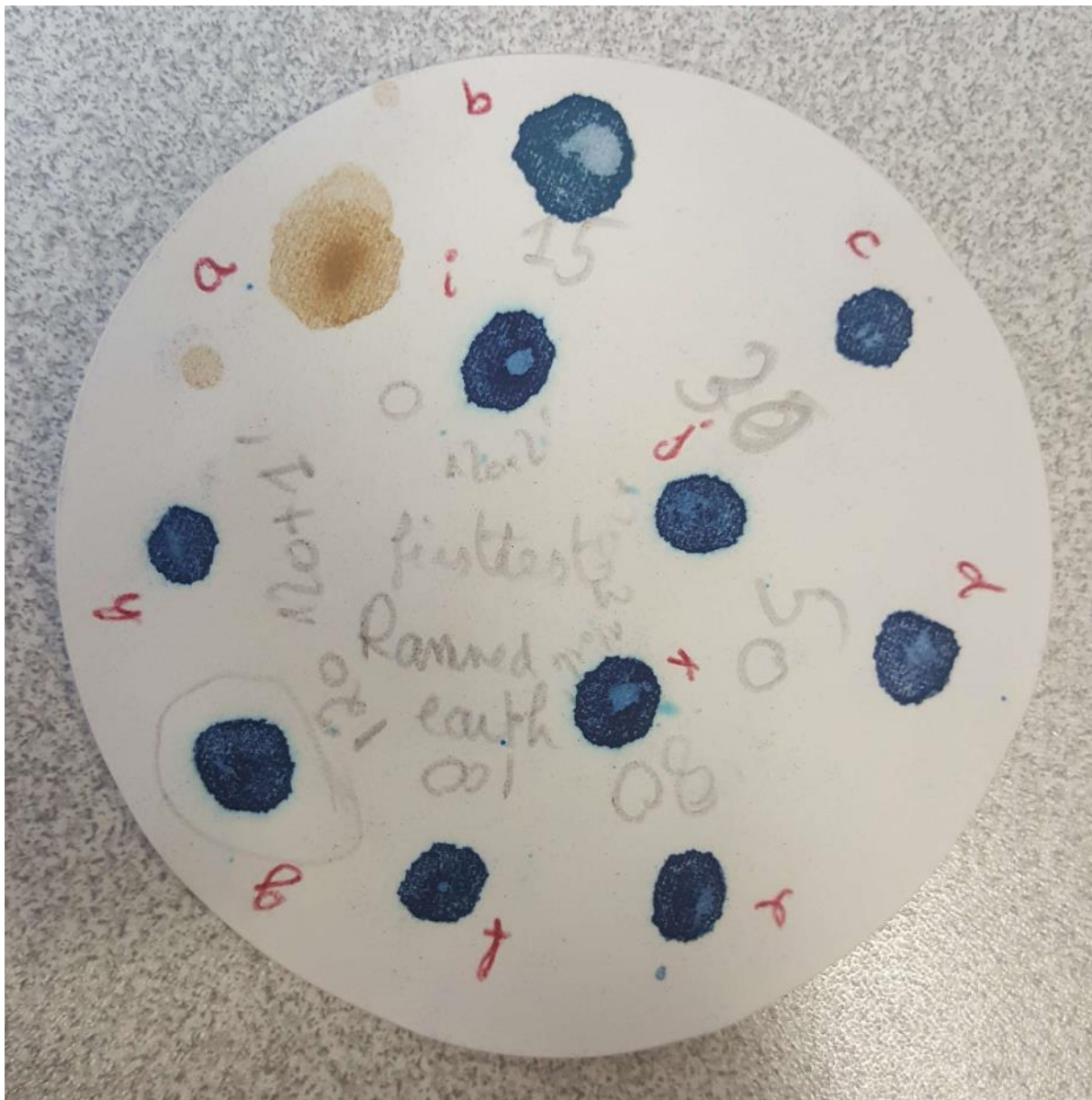| Reference	Methylene Blue added volume [mL]	Methylene Blue accumulated volume [mL]	Test result	Zoom of the final positive test
a	5	5	Negative	
b	5	10	Negative	
c	5	15	Negative	
d	5	20	Negative	
e	5	25	Negative	
f	5	30	Negative	
g	5	35	Positive	
h	-	35+1'	Positive	
i	-	35+2'	Negative	
j	2	37	Negative	
k	2	39	Positive	
l	-	39+1'	Positive	
m	-	39+2'	Negative	
n	2	41	Negative	
o	2	43	Negative	
p	2	45	Positive	
q	-	45+1'	Positive	
r	-	45+2'	Positive	
s	-	45+3'	Positive	
t	-	45+4'	Positive	

Figure AN 7 to Figure AN 9 and Table AN 6 indicate the MetBT process and results of each step from test 2. In this case, the MetBV obtained is 0.73 (Table AN 5).

Table AN 5: MetBV result of test 2

First Approach	Mass of soil (m) [g]	MetB volume (V) [mL]	MetBV (m / V) [-]
	38.3	60	**0.64**

Figure AN 7 – Drops of the Methylene Blue Test with 38.3 g of soil (test 2, part 1)

Figure AN 8 – Drops of the Methylene Blue Test with 38.3 g of soil (test 2, part 2)

Figure AN 9 – Drops of the Methylene Blue Test with 38.3 g of soil (test 2, part 3)

Table AN 6: Methylene Blue Test results for the test 2 with 38.3 g of soil

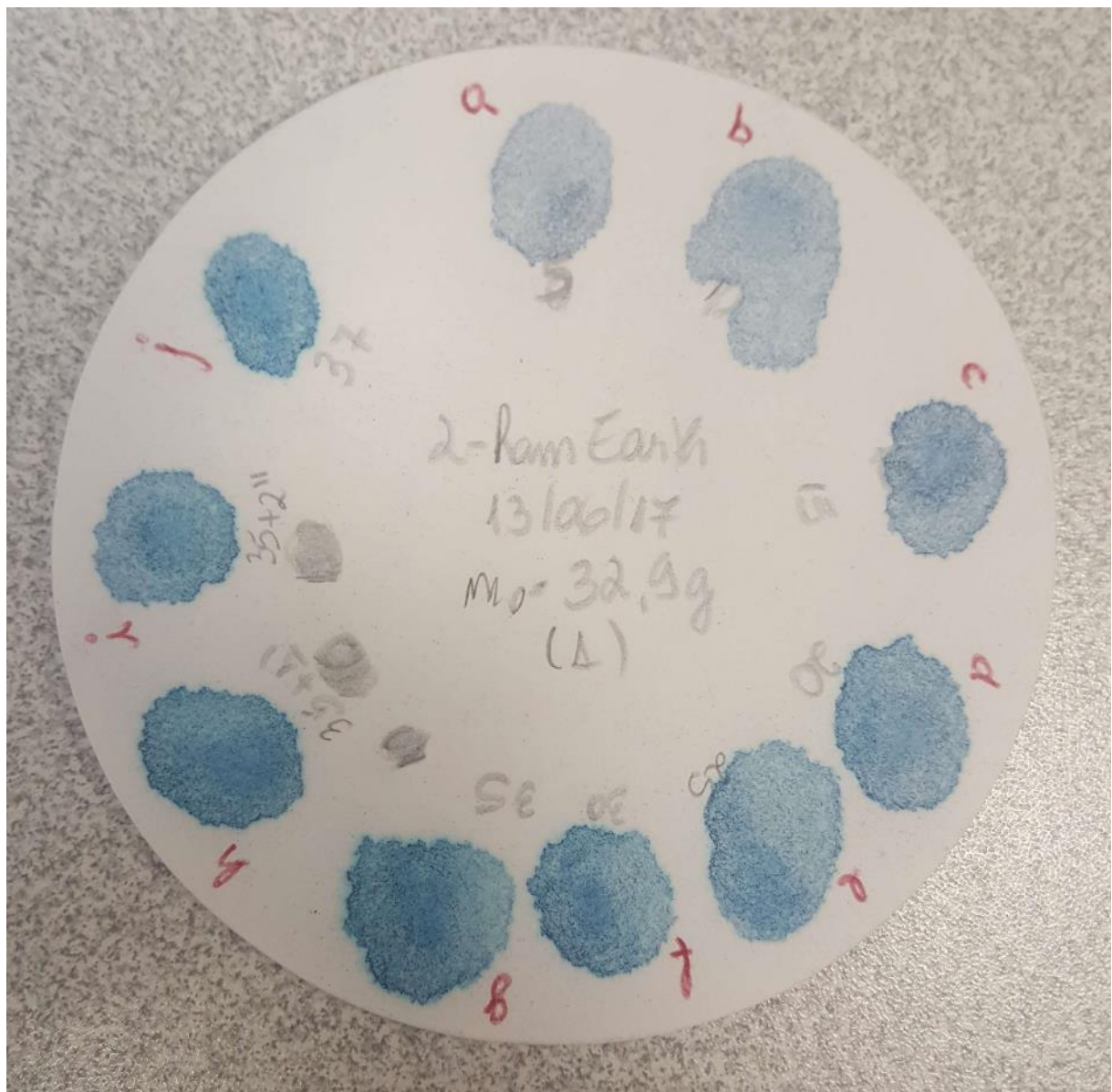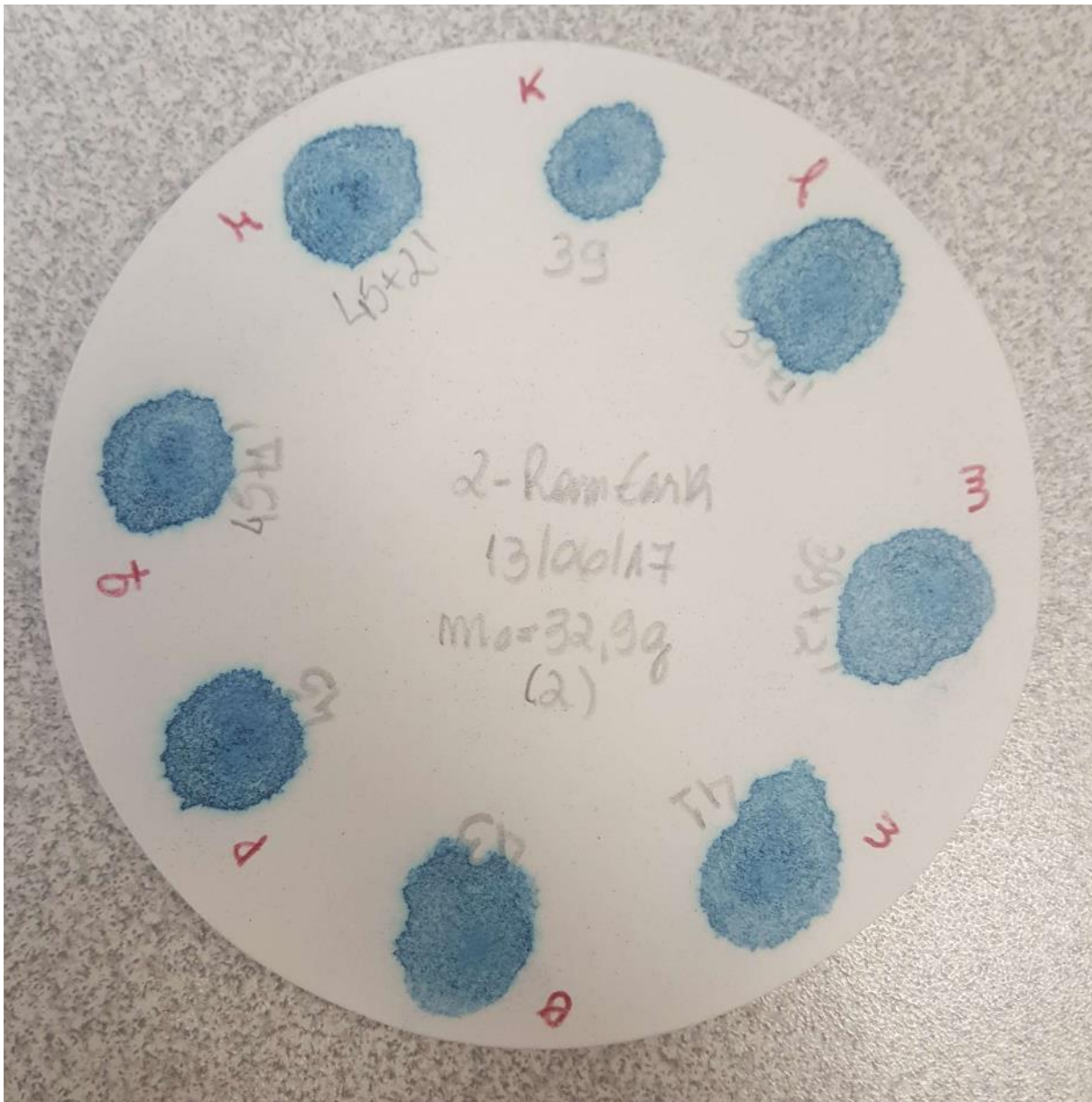| Reference	Methylene Blue added volume [mL]	Methylene Blue accumulated volume [mL]	Test result	Zoom of the final positive test
a	0	0	-	
b	5	5	Negative	
c	5	10	Negative	
d	5	15	Negative	
e	5	20	Negative	
f	5	25	Negative	
g	5	30	Negative	
h	5	35	Negative	
i	5	40	Negative	
j	5	45	Negative	
k	5	50	Positive	
l	-	50+1'	Positive	
m	-	50+2'	Negative	
n	2	52	Negative	
o	2	54	Negative	
p	2	56	Negative	
q	2	58	Positive	
r	-	58+1'	Positive	
s	-	58+2'	Positive	
t	-	58+3'	Negative	
u	2	60	Positive	
v	-	60+1'	Positive	
w	-	60+2'	Positive	
x	-	60+3'	Positive	
y	-	60+4'	Positive	

Figure AN 10 to Figure AN 13 and Table AN 8 indicate the MetBT process and results of each step from test 3. In this case, the MetBV obtained is 0.63 (Table AN 7).

Table AN 7: MetBV result of test 3

First Approach	Mass of soil (m) [g]	MetB volume (V) [mL]	MetBV (m / V) [-]
	31.6	50	**0.63**

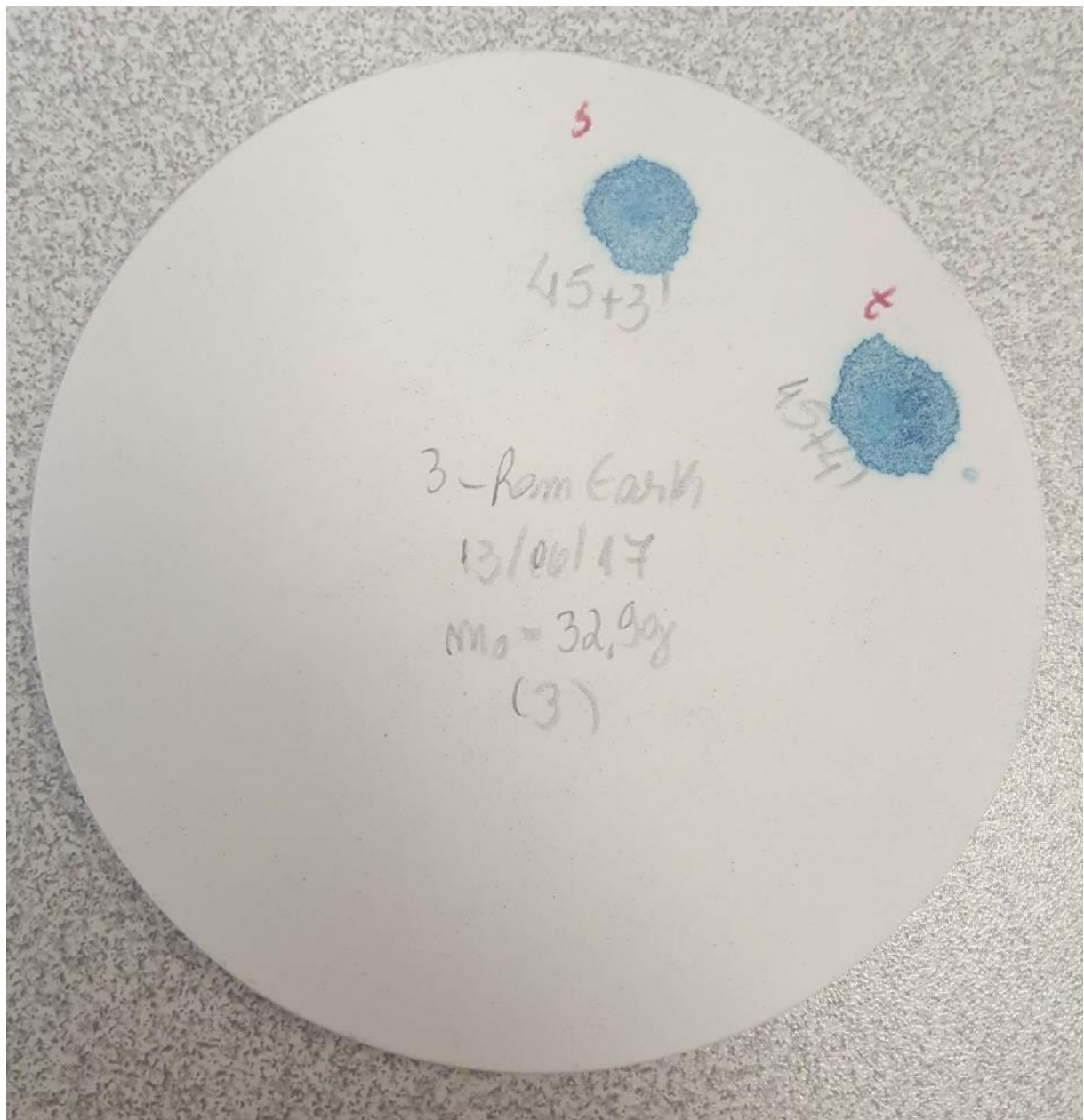**Figure AN 10 – Drops of the Methylene Blue Test with 31.6 g of soil (test 3, part 1)**
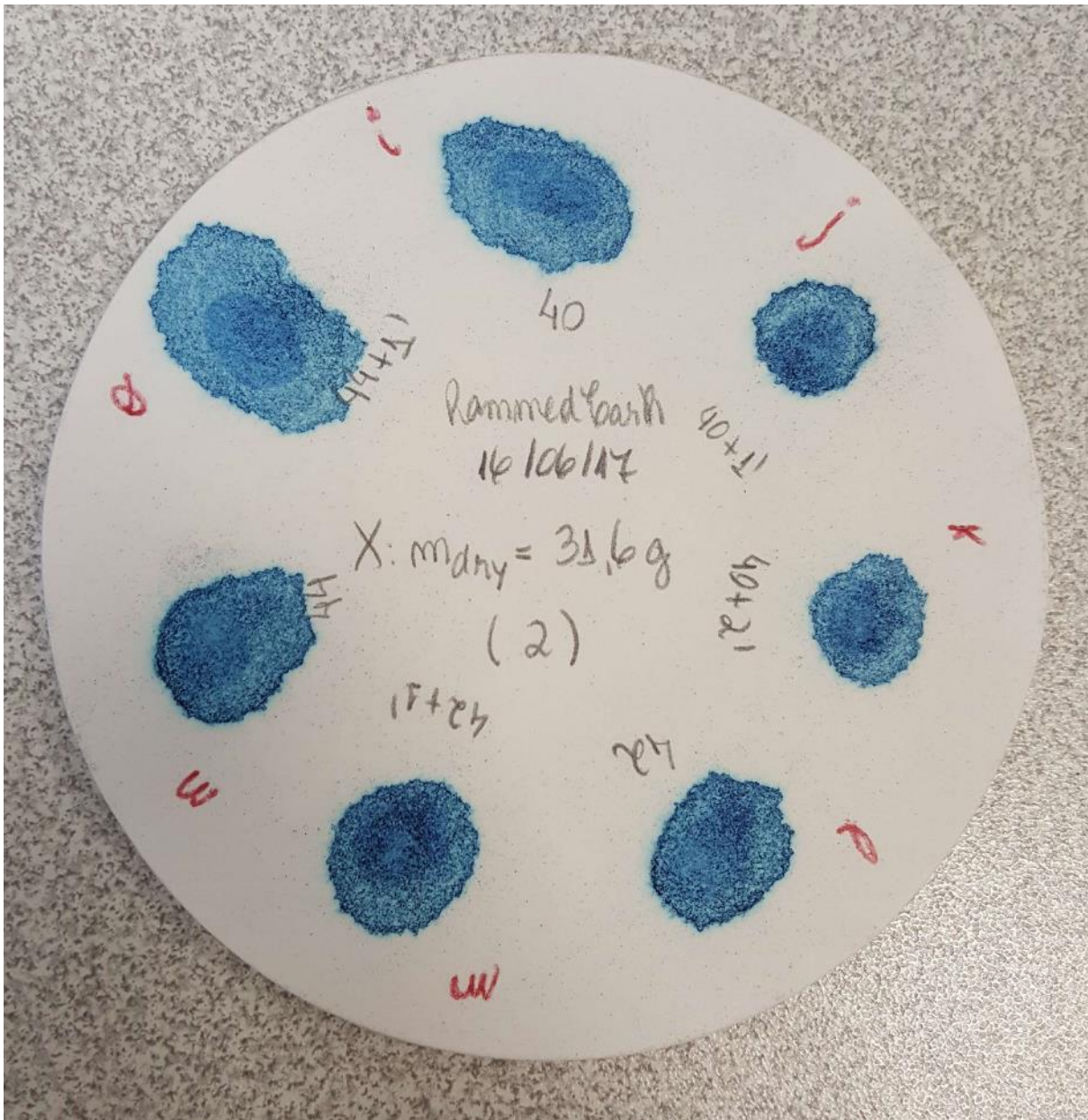
Figure AN 11 – Drops of the Methylene Blue Test with 31.6 g of soil (test 3, part 2)

Figure AN 12 – Drops of the Methylene Blue Test with 31.6 g of soil (test 3, part 3)

Figure AN 13 – Drops of the Methylene Blue Test with 31.6 g of soil (test 3, part 4)

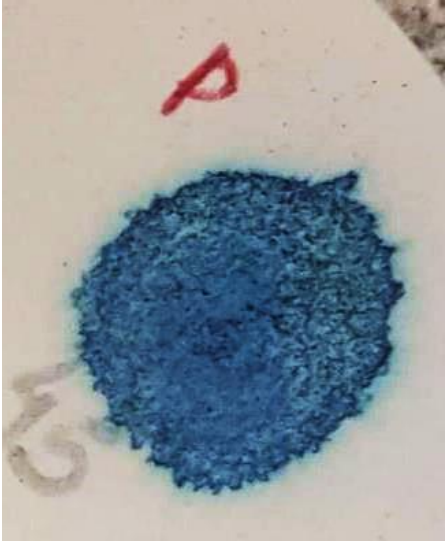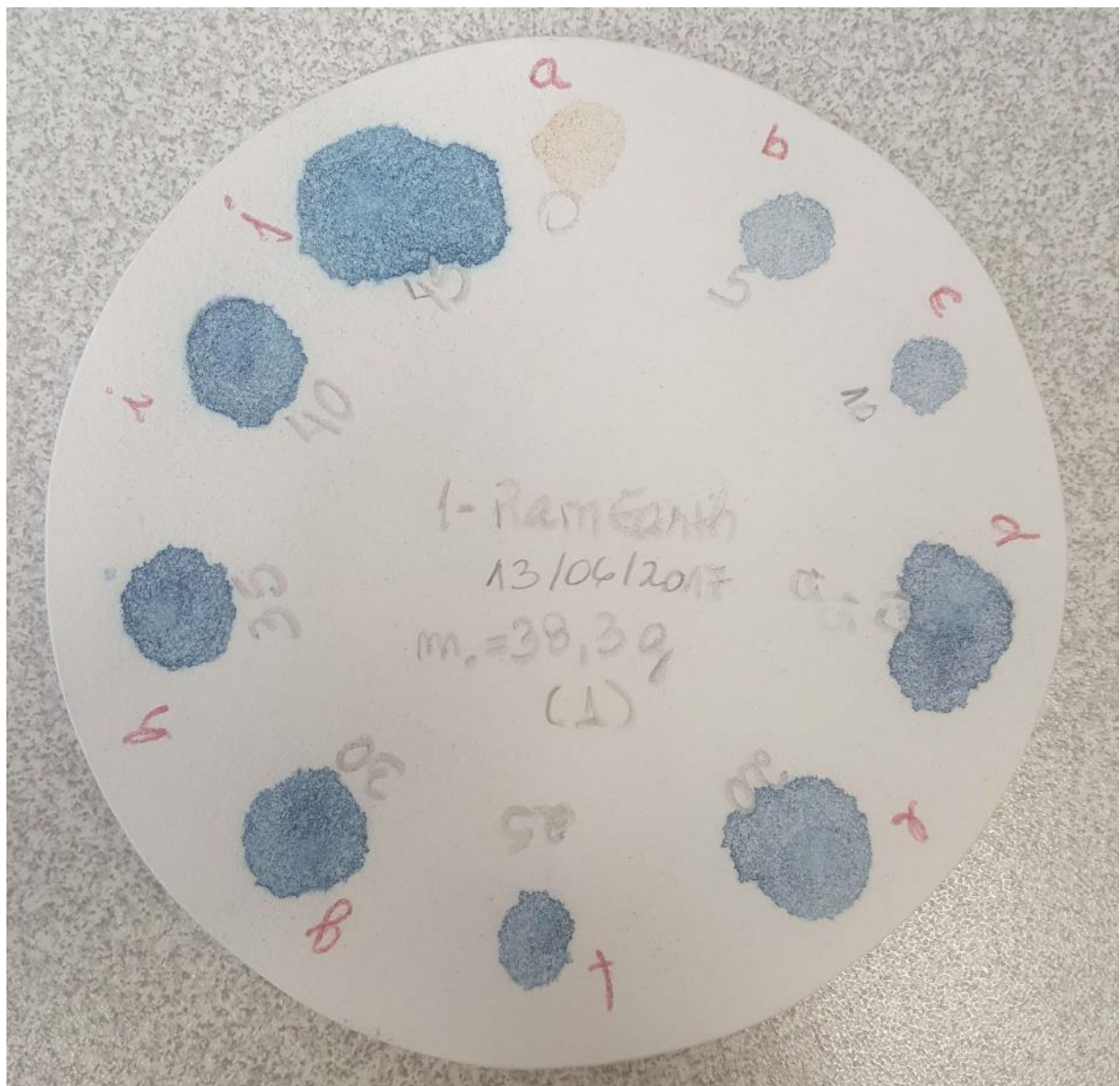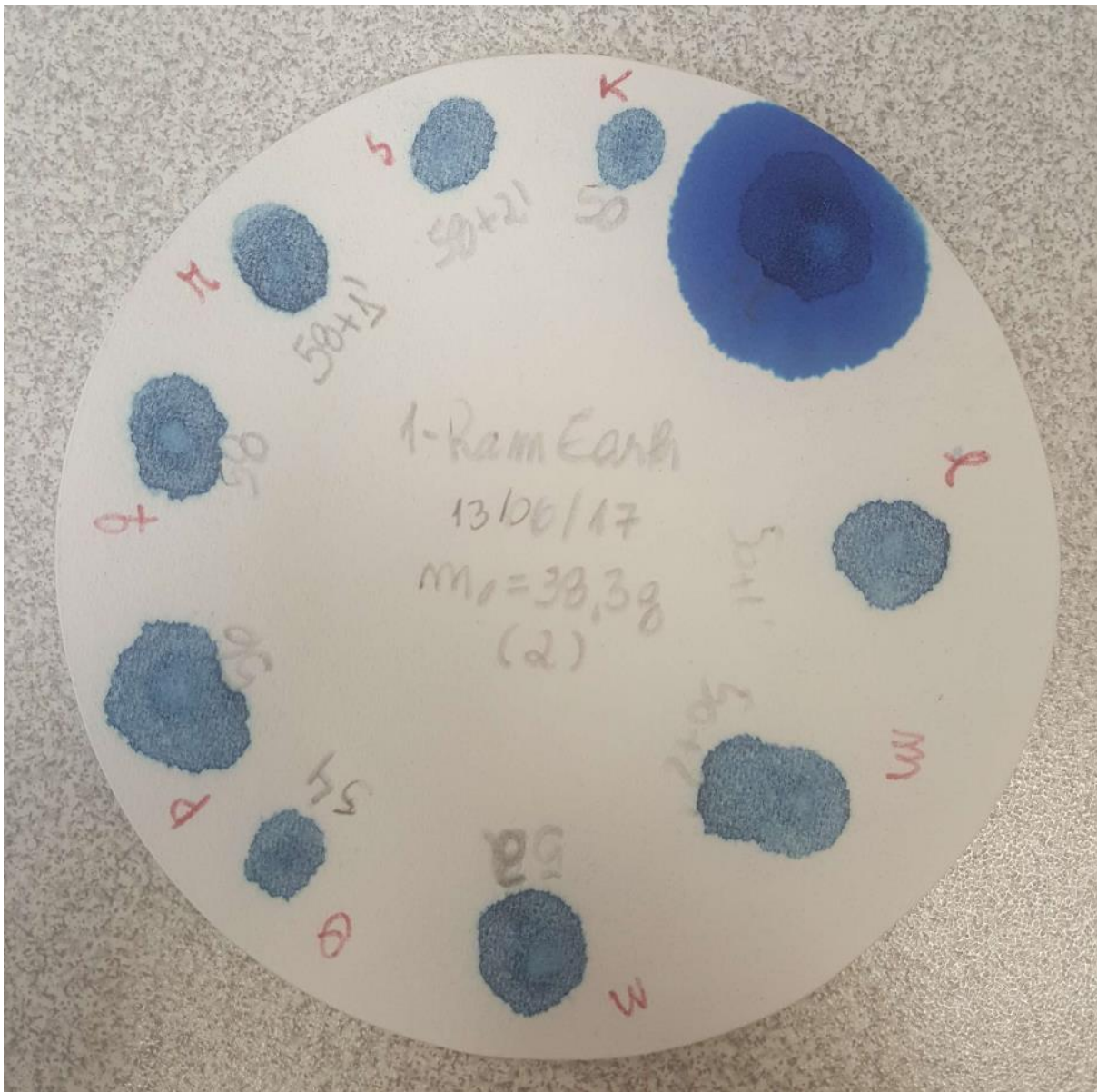**Table AN 8: Methylene Blue Test results for the test 3 with 31.6 g of soil**

Reference	Methylene Blue added volume [mL]	Methylene Blue accumulated volume [mL]	Test result	Zoom of the final positive test
a	0	0	-	
B	5	5	Negative	
C	5	10	Negative	
D	5	15	Negative	
E	5	20	Negative	
f	5	25	Negative	
g	5	30	Negative	
h	5	35	Negative	
i	5	40	Positive	
j	-	40+1'	Positive	
k	-	40+2'	Negative	
l	2	42	Positive	
m	-	42+1'	Negative	
n	2	44	Positive	
o	-	44+1'	Positive	
p	-	44+2'	Negative	
q	2	46	Positive	
r	-	46+1'	Negative	
s	2	48	Positive	
t	-	48+1'	Positive	
u	-	48+2'	Positive	
v	-	48+3'	Positive	
w	-	48+4'	Negative	
x	2	50	Positive	
Y	-	50+1'	Positive	
Z	-	50+2'	Positive	
aa	-	50+3'	Positive	
ab	-	50+4'	Positive	

Figure AN 14 to Figure AN 16 and Table AN 10 indicate the MetBT process and results of each step from test 4. In this case, the MetBV obtained is 0.63 (Table AN 9).

Table AN 9: MetBV result of test 4

First Approach	Mass of soil (m) [g]	MetB volume (V) [mL]	MetBV (m / V) [-]
	34.5	55	**0.63**

Figure AN 14 – Drops of the Methylene Blue Test with 34.5 g of soil (test 4, part 1)
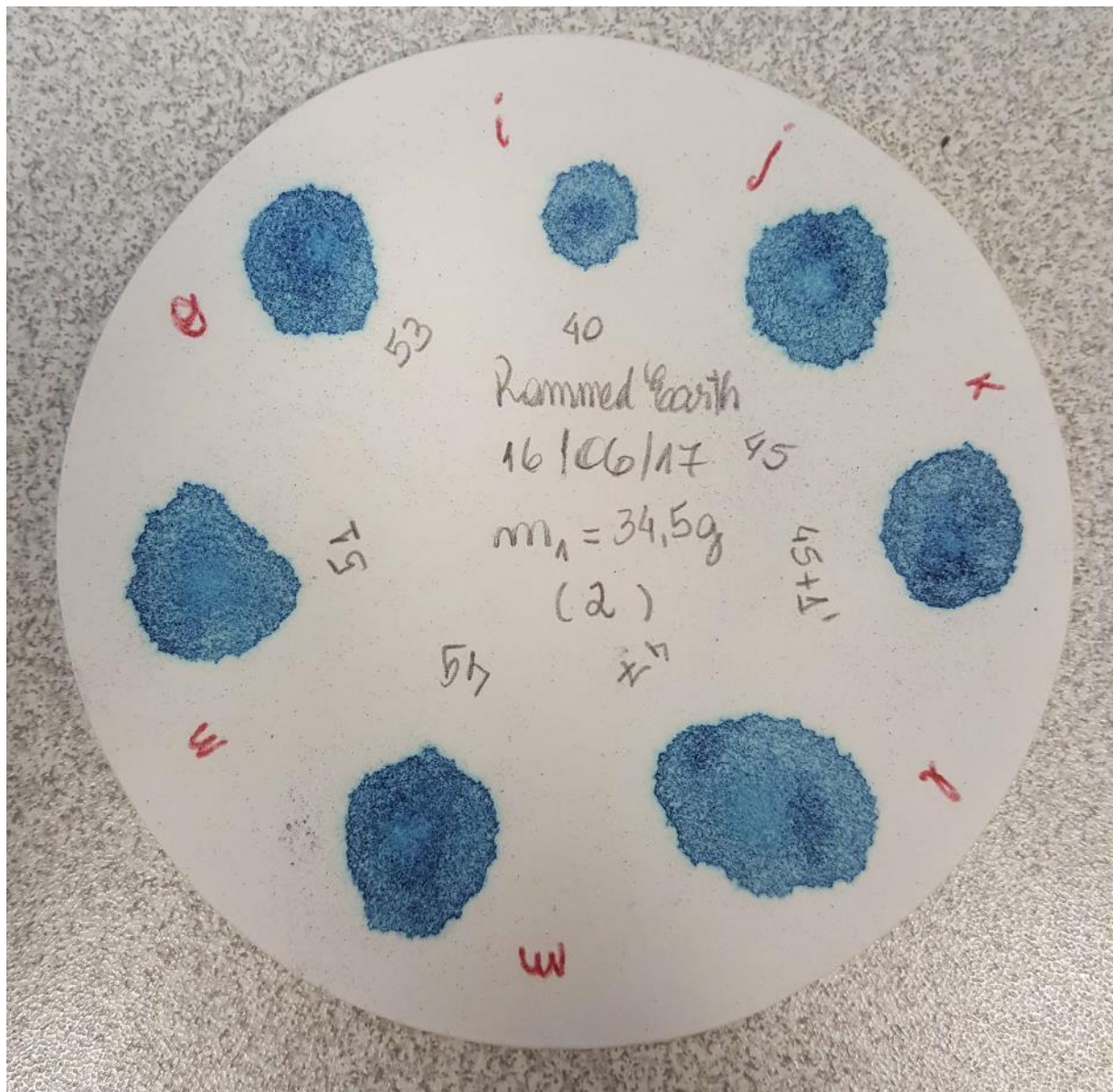
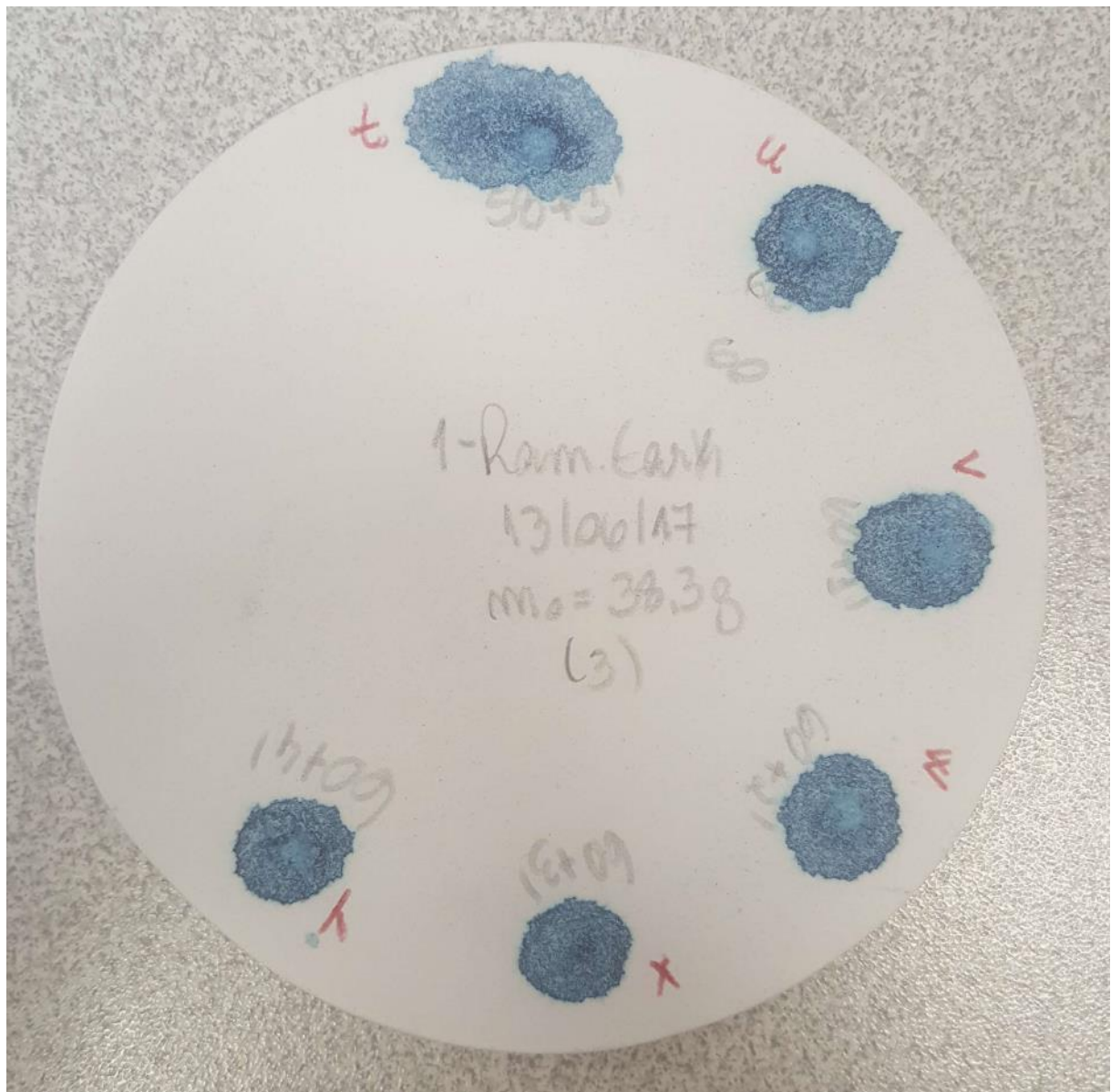**Figure AN 15 – Drops of the Methylene Blue Test with 34.5 g of soil (test 4, part 2)**
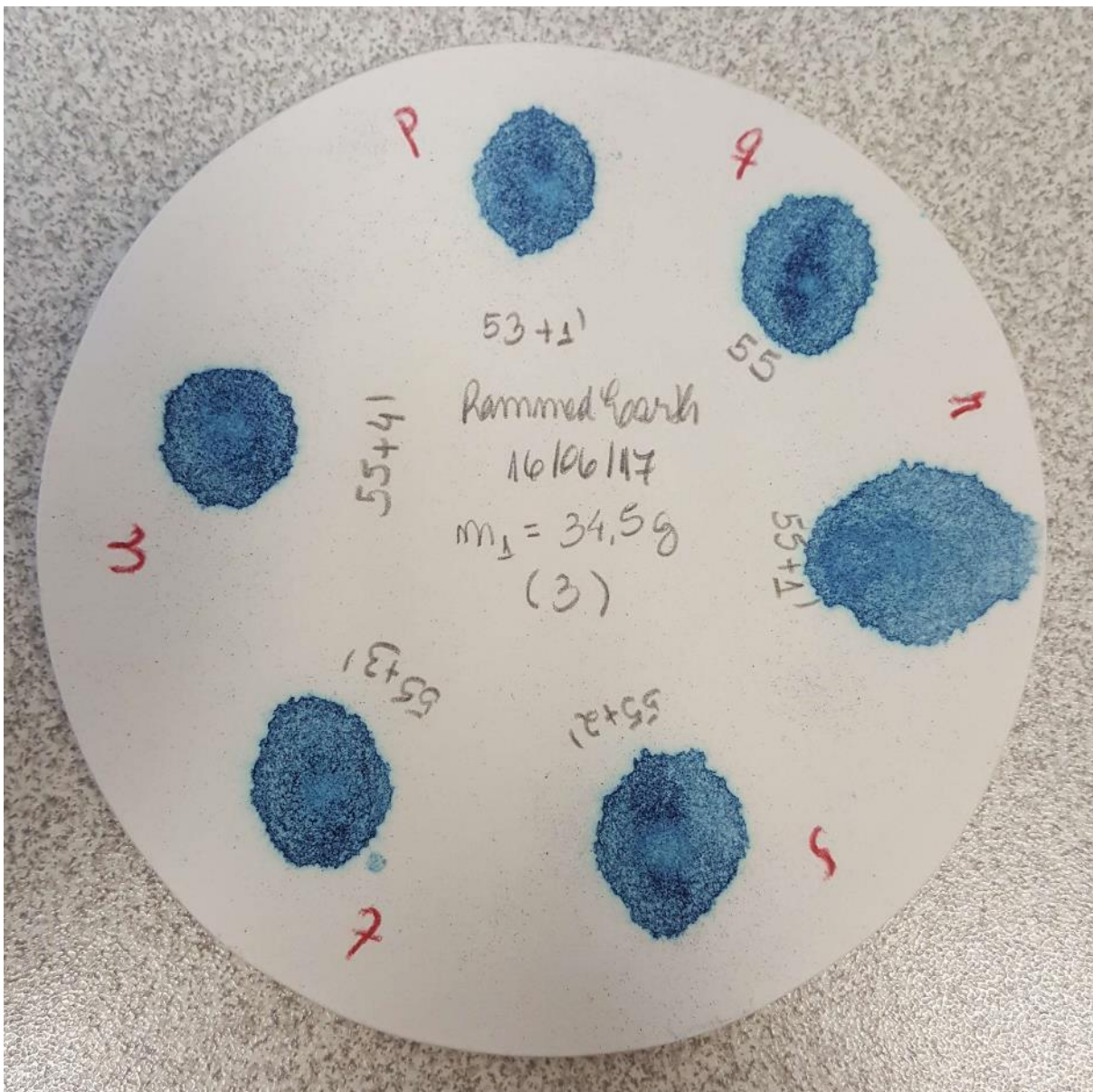
Figure AN 16 – Drops of the Methylene Blue Test with 34.5 g of soil (test 4, part 3)

Table AN 10: Methylene Blue Test results for the test 4 with 34.5 g of soil
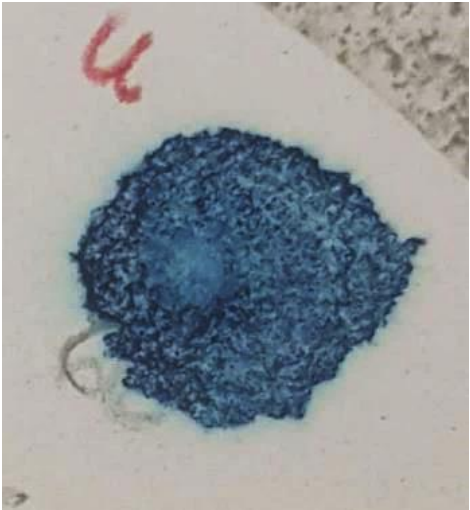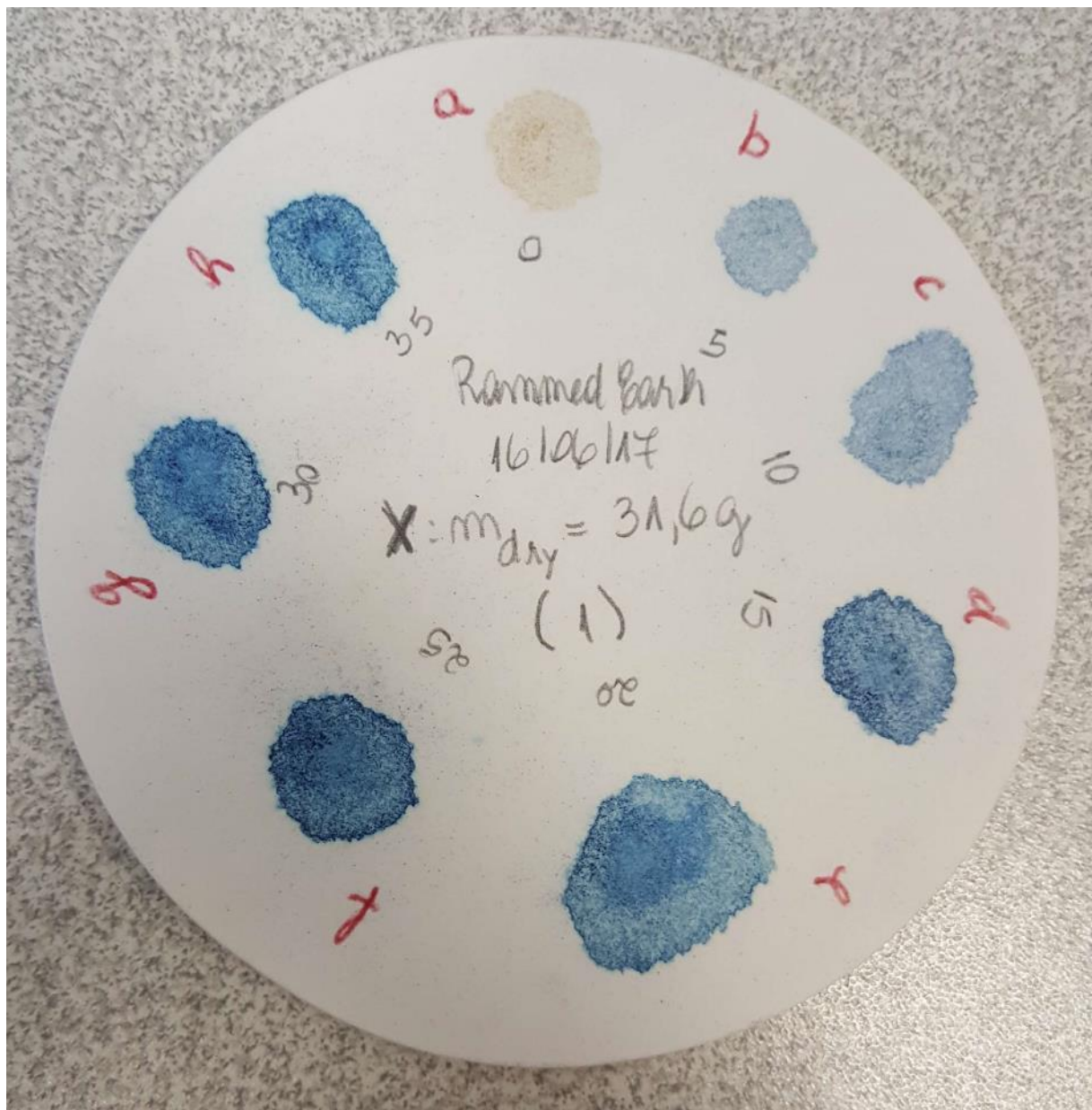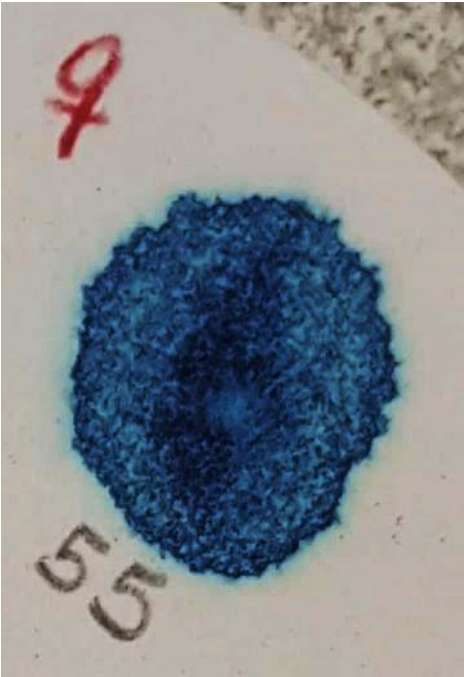
Reference	Methylene Blue added volume [mL]	Methylene Blue accumulated volume [mL]	Test result	Zoom of the final positive test
a	0	0	-	
b	5	5	Negative	
c	5	10	Negative	
d	5	15	Negative	
e	5	20	Negative	
f	5	25	Negative	
g	5	30	Negative	
h	5	35	Negative	
i	5	40	Negative	
j	5	45	Negative	
k	-	45+1'	Positive	
l	2	47	Positive	
m	2	49	Negative	
n	2	51	Negative	
o	2	53	Negative	
p	-	53+1'	Negative	
q	22	55	Positive	
r	-	55+1'	Positive	
s	-	55+2'	Positive	
t	-	55+3'	Negative	
u	-	55+4'	Positive	

Figure AN 17 to Figure AN 18 and Table AN 12 indicate the MetBT process and results of each step from test 5. In this case, the MetBV obtained is 0.65 (Table AN 11).

Table AN 11: MetBV result of test 5

| First Approach	Mass of soil (m) [g]	MetB volume (V) [mL]	MetBV (m / V) [-]
	26.0	40	**0.65**
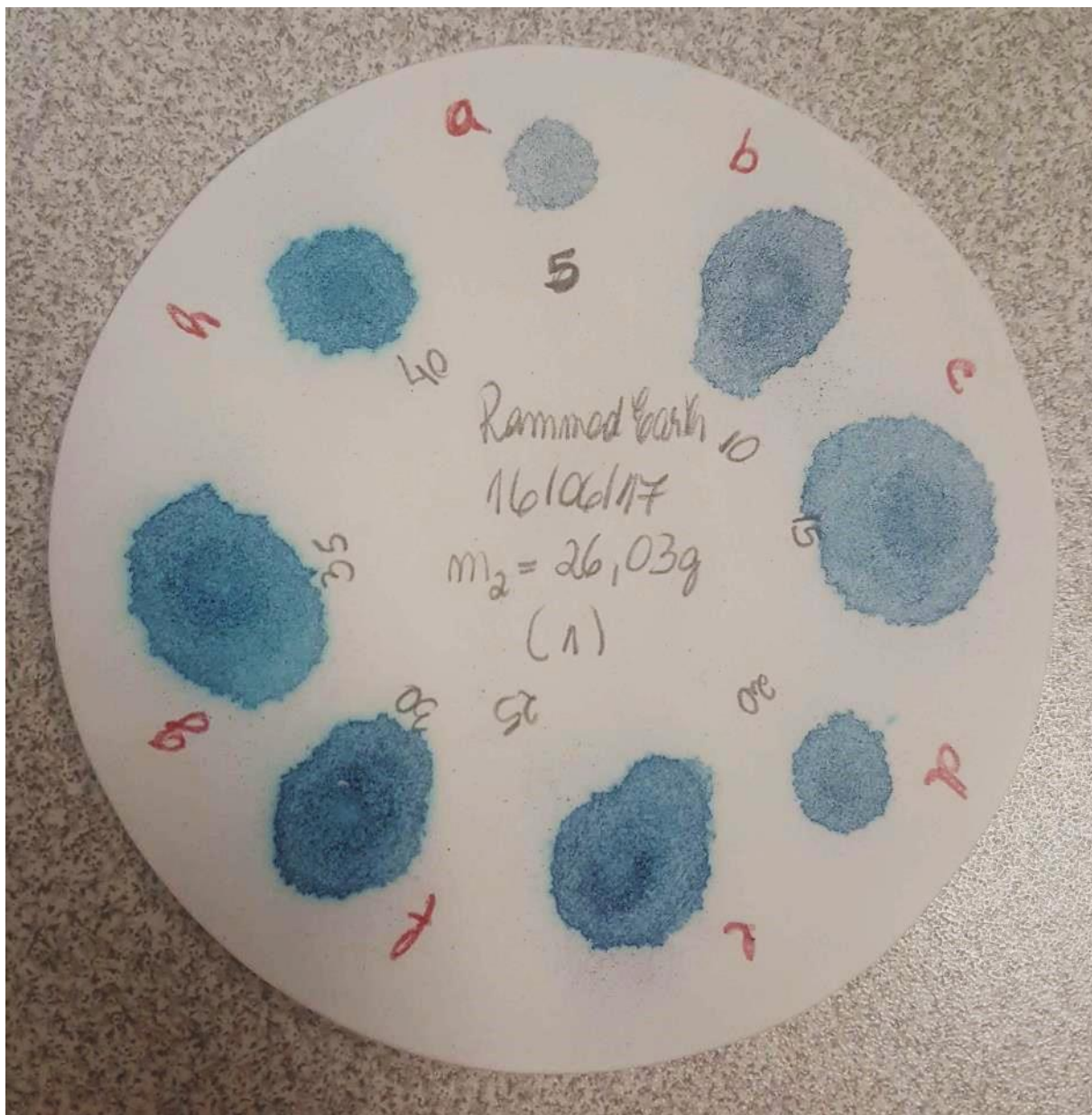
Figure AN 17 – Drops of the Methylene Blue Test with 26.0 g of soil (test 5, part 1)
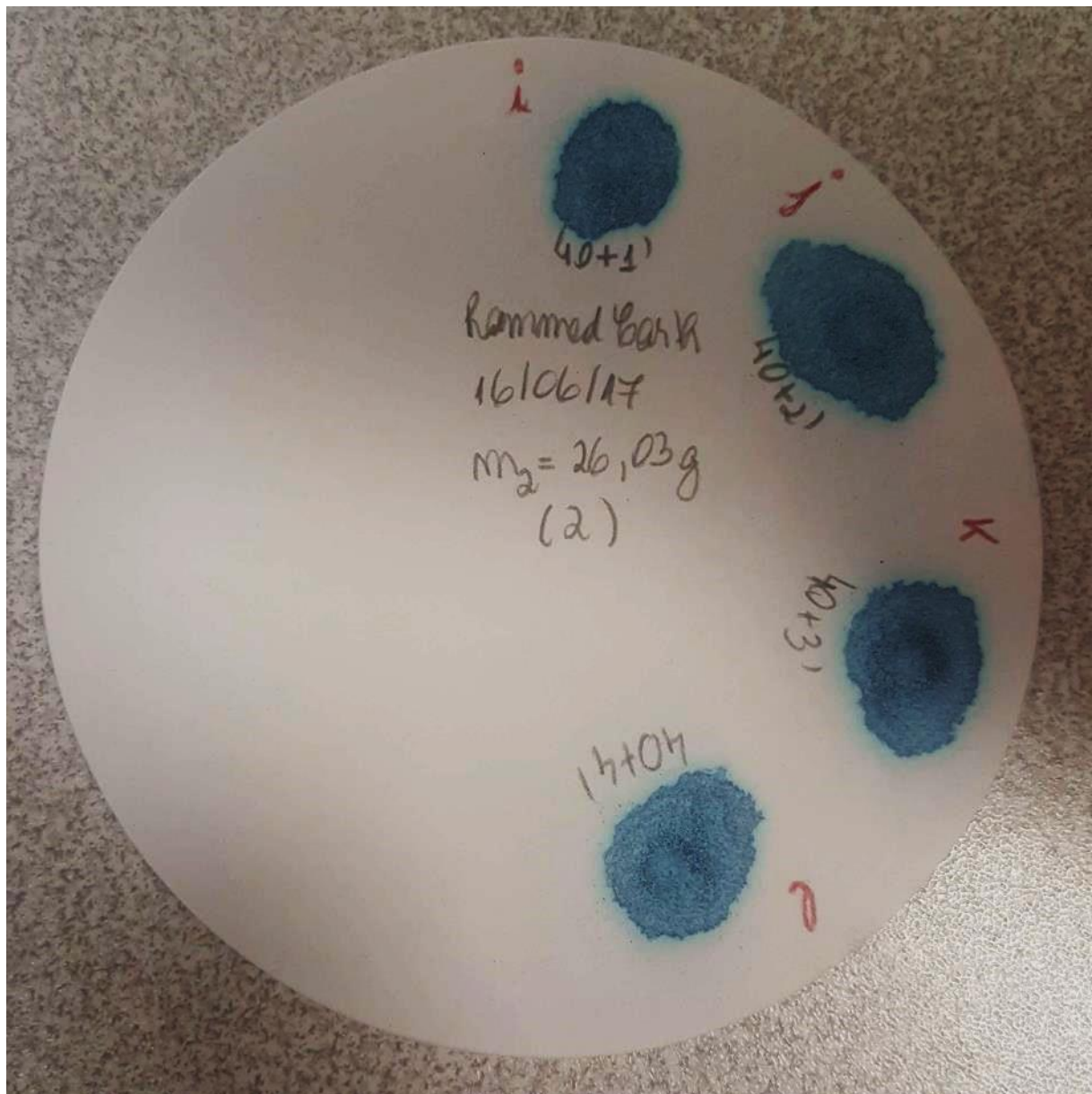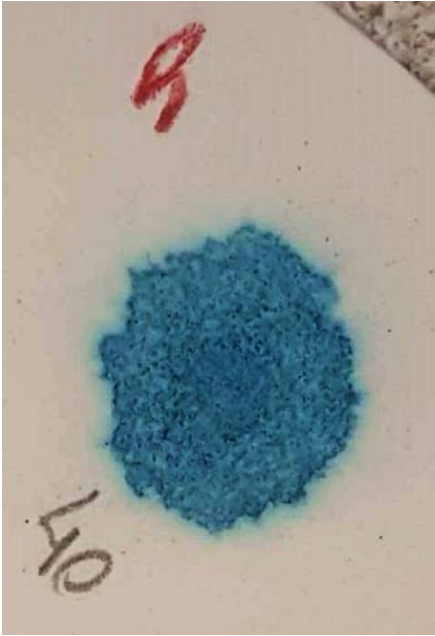
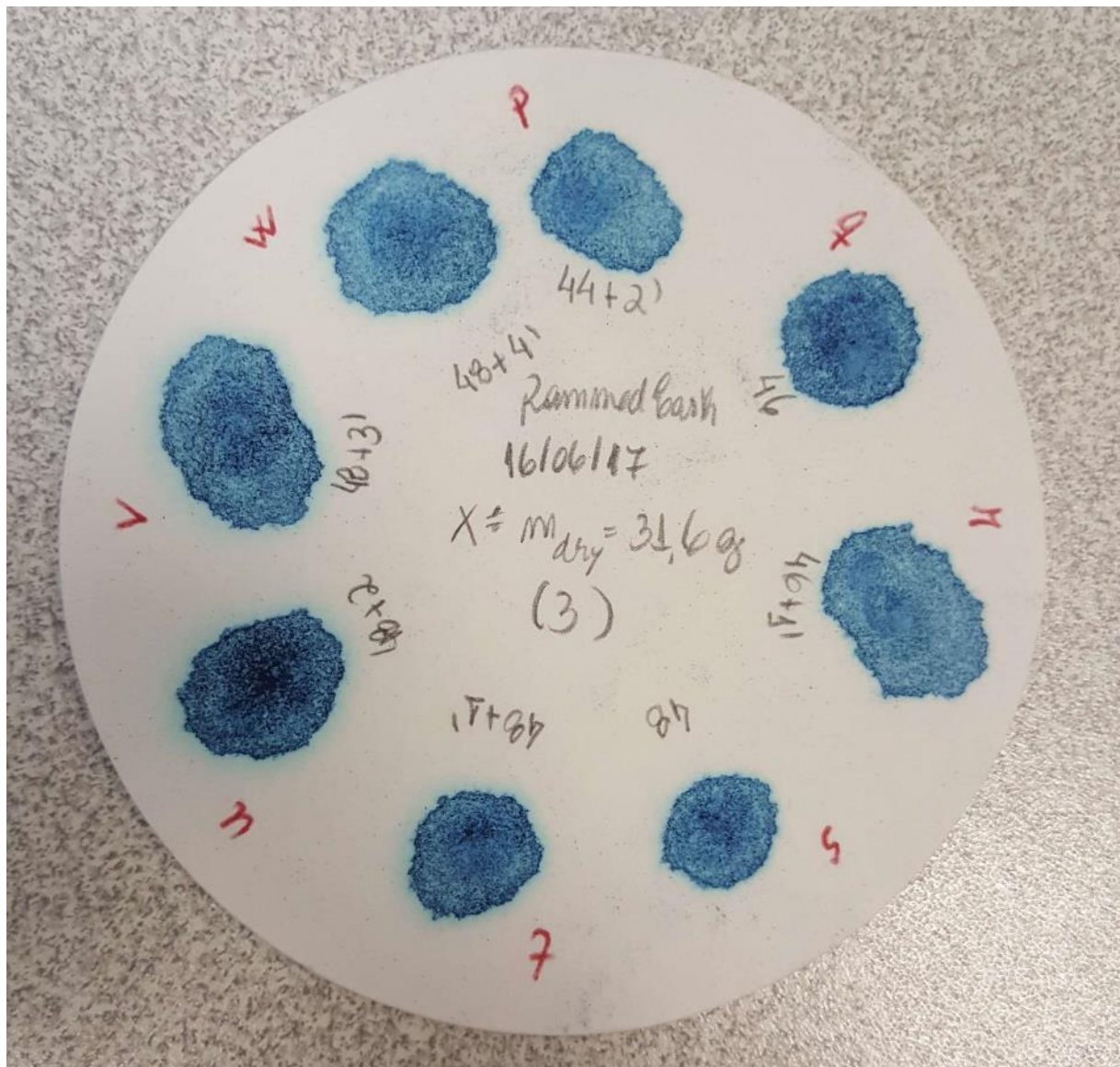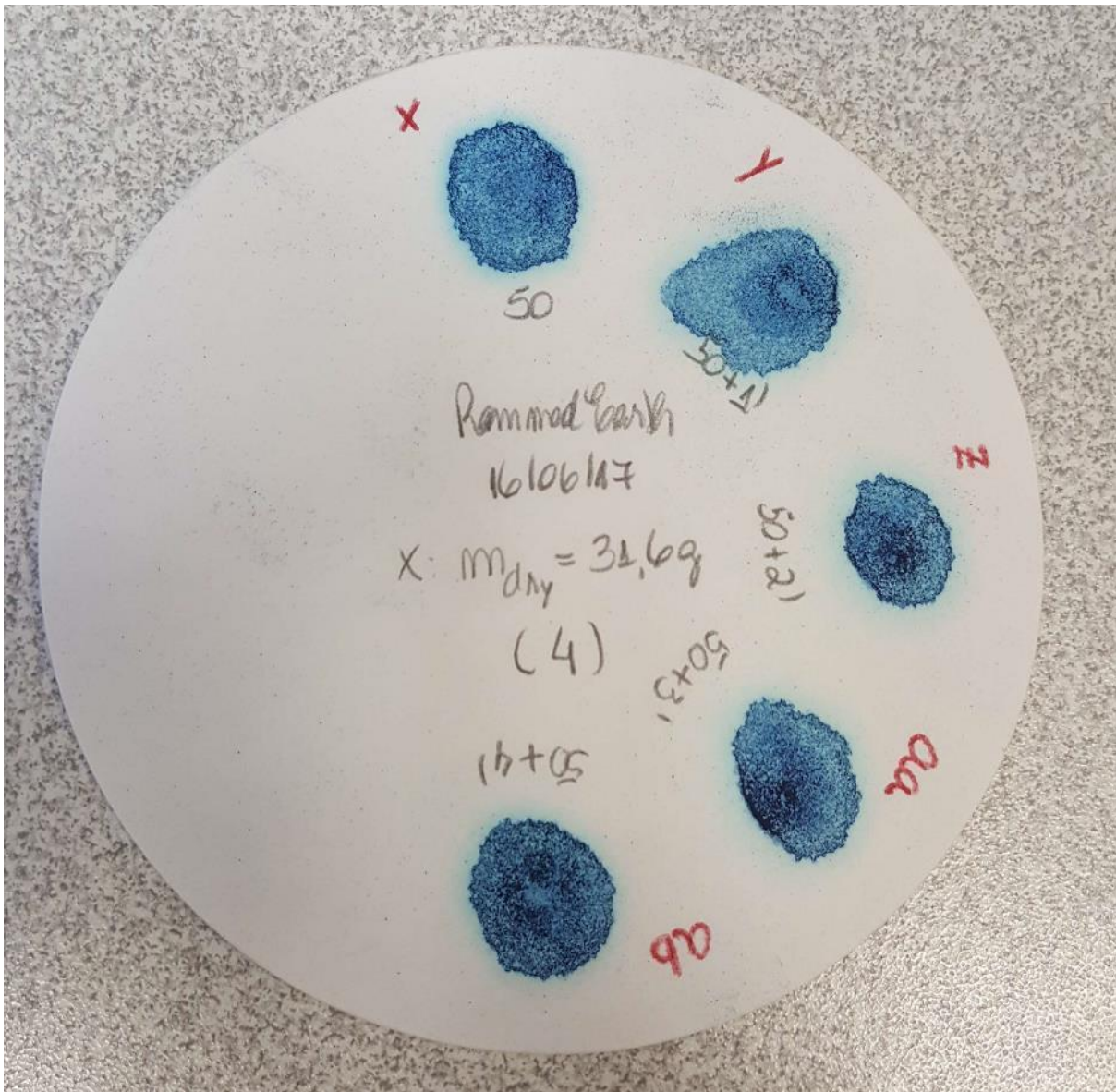**Figure AN 18 – Drops of the Methylene Blue Test with 26.0 g of soil (test 5, part 2)**

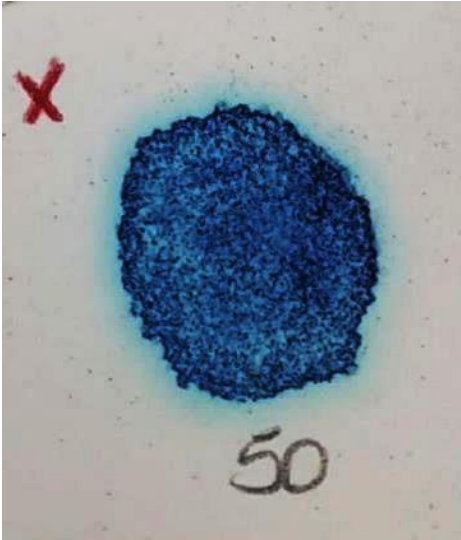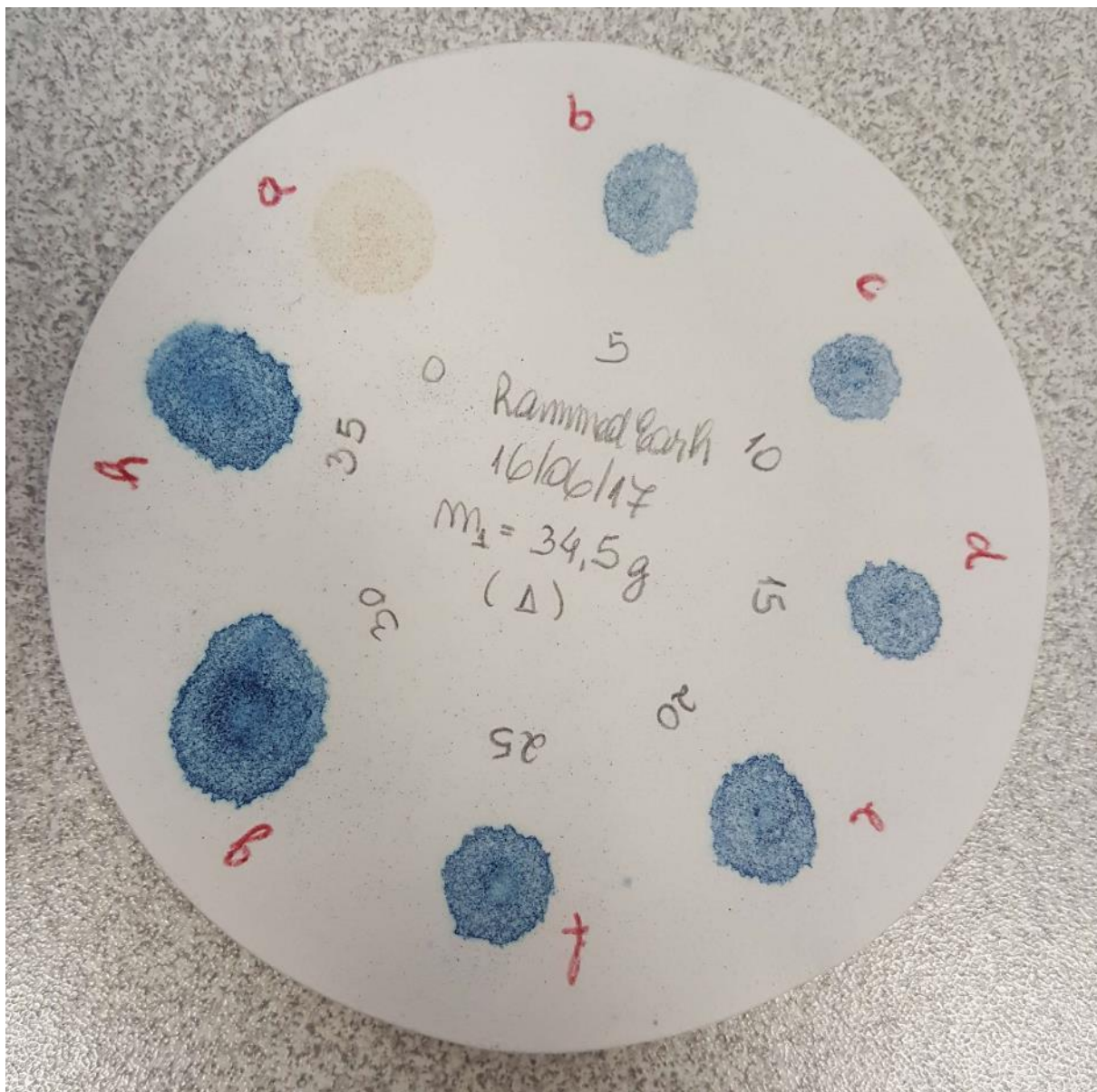**Table AN 12: Methylene Blue Test results for the test 4 with 34.5 g of soil**

Reference	Methylene Blue added volume [mL]	Methylene Blue accumulated volume [mL]	Test result	Zoom of the final positive test
a	5	5	Negative	
b	5	10	Negative	
c	5	15	Negative	
d	5	20	Negative	
e	5	25	Negative	
f	5	30	Negative	
g	5	35	Negative	
h	5	40	Positive	
i	5	40+1'	Positive	
j	5	40+2'	Positive	
k	-	40+3'	Positive	
l	-	40+4'	Positive	

APPENDIX C – Properties of tested samples

Table AN 13: Properties of manufactured samples

Sample	Set of soil	Status	Average dry density [kg/m³]	Mass of tested sample (estimation without plaster) [g]	Water content within tested sample
1	B	broke	-	-	-
2	B	tested	1637	891	1.0%
3	B	tested	1637	891	1.0%
4	B	tested	1637	891	1.0%
5	C	broke	-	-	-
6	C	tested	1637	893	1.3%
7	C	broke	-	-	-
8	C	tested	1637	893	1.3%
9	C	broke	-	-	-
10	C	broke	-	-	-
11	C	tested	1637	892	1.2%
12	C	invalid test	-	-	-
13	B	broke	-	-	-
14	C	tested	1637	892	1.2%
15	C	broke	-	-	-
16	B	tested	1637	893	1.3%
17	A	tested	1629	908	3.4%
18	A	tested	1629	904	3.0%
19	A	tested	1629	907	3.3%
20	A	tested	1629	913	4.0%
21	B	tested	1637	892	1.2%
22	C	tested	1637	908	3.0%
23	B	invalid test	-	-	-
24	B	invalid test	-	-	-
25	B	tested	1637	908	3.0%

(continues on the next page)

Table AN 13 (continued)

Sample	Set of soil	Status	Average dry density [kg/m³]	Mass of tested sample (estimation without plaster) [g]	Water content within tested sample
26	B	broke	-	-	-
27	B	tested	1637	909	3.1%
28	B	broke	-	-	-
29	B	broke	-	-	-
30	B	broke	-	-	-
31	Bd	broke	-	-	-
32	Bd	invalid test	-	-	-
33	Bd	tested	1748	959	1.8%
34	Bd	invalid test	-	-	-
35	Bd	tested	1803	989	1.8%
36	Bd	tested	1756	963	1.8%
37	Bd	broke	-	-	-
38	Bd	tested	1721	944	1.8%
39	Bd	invalid test	-	-	-
40	Bd	invalid test	-	-	-
41	Bd	tested	1798	986	1.8%
42	Bd	tested	1761	966	1.8%
43	Bd	for future test	-	-	-
44	Bd	for future test	-	-	-
45	Bd	for future test	-	-	-
46	C	broke	-	-	-
47	C	broke	-	-	-
48	C	broke	-	-	-
49	C	broke	-	-	-
50	C	broke	-	-	-
51	D	broke	-	-	-

(continues on the next page)

Table AN 13 (continued)

Sample	Set of soil	Status	Average dry density [kg/m³]	Mass of tested sample (estimation without plaster) [g]	Water content within tested sample
52	D	tested	1675	929	3.0%
53	D	broke	-	-	-
54	D	tested	1675	936	3.7%
55	D	broke	-	-	-
56	D	tested	1675	929	3.0%
57	D	tested	1675	930	3.1%
58	D	tested	1675	929	3.0%
59	D	tested	1675	929	3.0%
60	D	broke	-	-	-
61	D	tested	1675	915	1.4%
62	D	broke	-	-	-
63	D	tested	1675	931	3.2%
64	D	broke	-	-	-
65	D	tested	1675	915	1.4%
66	D	tested	1675	916	1.5%
67	D	tested	1675	915	1.4%
68	E	tested	1698	931	1.8%
69	E	for future tests	-	-	-
70	E	tested	1698	944	3.2%
71	E	tested	1698	951	4.0%
72	E	tested	1698	929	1.6%
73	E	tested	1698	933	2.0%
74	E	broke	-	-	-
75	E	broke	-	-	-
76	E	tested	1698	930	1.7%
77	E	tested	1698	932	1.9%

(continues on the next page)

Table AN 13 (continued)

Sample	Set of soil	Status	Average dry density [kg/m³]	Mass of tested sample (estimation without plaster) [g]	Water content within tested sample
78	E	tested	1698	933	2.0%
79	F	tested	1667	909	1.2%
80	F	tested	1667	909	1.2%
81	F	tested	1667	909	1.2%
82	F	broke	-	-	-
83	F	tested	1667	907	1.0%
84	F	tested	1667	914	1.8%

APPENDIX D – Results of all compression, extension and Brazilian tests

Table AN 14: Results of repeatability tests for compression stress path (w = 2% and 4%)

water content (w)	confining pressure [KPa]	Label	Test	Set of samples	Sample	Dry density	Maximum load [kN]	Maximum strength [MPa]	Elastic modulus [MPa]
2%	unconfined	U2%i	Test3	C	11	1637	2.80	0.72	130
		U2%ii	Test7	B	3	1637	2.82	0.73	144
		U2%iii	Test12	B	21	1637	2.53	0.65	108
		U2%Bd	Test10	Bd	35	1803	3.70	0.95	149
	300	C3bar2%i	Test1	B	2	1637	6.51	1.64	135
		C3bar2%ii	Test5	B	4	1637	6.17	1.55	180
		C3bar2%iii	Test6	C	6	1637	5.18	1.30	221
		C3bar2%Bd	Test11	Bd	41	1798	8.76	2.22	181
	600	C6bar2%i	Test8	C	8	1637	8.51	1.87	128
		C6bar2%ii	Test13	B	16	1637	8.61	1.84	144
		C6bar2%iii	Test15	C	14	1637	8.04	2.00	157
		C6bar2%Bd	Test9	Bd	33	1748	10.53	2.26	144
	800	C8bar2%i	Test33	B	72	1698	10.42	2.21	149
		C8bar2%ii	Test34	E	73	1698	10.40	2.12	151
		C8bar2%iii	Test36	F	79	1667	10.49	2.35	187
4%	unconfined	U4%i	Test18	A	17	1629	1.86	0.48	60
		U4%ii	Test19	A	19	1629	1.94	0.50	59
	300	C3bar4%i	Test17	A	18	1629	4.80	1.08	149
		C3bar4%ii	Test30	C	22	1637	4.27	1.00	112
	600	C6bar4%i	Test16	A	20	1629	8.80	1.65	103
		C6bar4%ii	Test49	D	56	1675	7.03	1.51	102
	800	C8bar4%i	Test47	D	63	1675	10.07	1.94	105
		C8bar4%ii	Test48	D	58	1675	10.12	1.92	96

Table AN 15: Results of repeatability tests for extension stress path (w = 2% and 4%)

water content (w)	confining pressure [KPa]	Label	Test	Set of samples	Sample	Dry density	Maximum load [kN]	Maximum strength [MPa]
2%	600	E6bar2%i	Test27	D	65	1675	2.09	0.54
		E6bar2%ii	Test28	D	67	1675	2.13	0.55
		E6bar2%iii	Test37	F	80	1667	2.15	0.56
		E6bar2%Bdi	Test20	Bd	38	1721	2.02	0.52
		E6bar2%Bdii	Test21	Bd	36	1756	1.98	0.51
	800	E8bar2%i	Test25	D	61	1675	2.44	0.63
		E8bar2%ii	Test26	D	66	1675	2.78	0.72
		E8bar2%iii	Test38	F	81	1667	2.55	0.66
	1000	E10bar2%Bd	Test23	Bd	42	1761	3.25	0.84
	1300	E13bar2%i	Test24	E	68	1698	3.57	0.93
		E13bar2%ii	Test46	F	83	1667	3.78	0.98
		E13bar2%iii	Test52	F	84	1667	3.82	0.99
4%	600	E6bar4%i	Test32	B	25	1637	1.93	0.50
		E6bar4%ii	Test50	D	57	1675	1.80	0.47
	800	E8bar4%i	Test35	B	27	1637	2.19	0.57
		E8bar4%ii	Test51	D	59	1675	2.31	0.60
	1300	E13bar4%i	Test53	D	52	1675	3.62	0.94
		E13bar4%ii	Test54	D	54	1675	3.42	0.89

Table AN 16: Results of repeatability tests for Brazilian tests (w = 2% and 4%)

water content (w)	Label	Test	Set of samples	Sample	Dry density	Maximum load [kN]	Maximum strength [MPa]
2%	B2%i	Test40	E	76	1698	0.67	0.04
	B2%ii	Test41	E	77	1698	0.75	0.05
	B2%iii	Test42	E	78	1698	0.62	0.04
4%	B4%i	Test43	E	70	1698	0.43	0.03
	B4%ii	Test44	E	71	1698	0.35	0.02

ANNEX A – Deviatoric stress and invariants

Deviatoric stress tensor and its invariants are frequently used in failure criteria. They derive from the stress tensor acting on a body, which is reviewed in this section specifically for a third-order problem. Nevertheless, the concepts can be extrapolated to systems of higher order. All the information here provided is based on RockMechs review (RockMechs - Rock Mechanics for Engineers, 2011).

The matrix form of stress tensor $[\sigma]$ acting on a body is:

$$[\sigma] = \begin{bmatrix} \sigma_{11} & \sigma_{12} & \sigma_{13} \\ \sigma_{21} & \sigma_{22} & \sigma_{23} \\ \sigma_{31} & \sigma_{32} & \sigma_{33} \end{bmatrix} \tag{28}$$

The stress tensor can be expressed as a sum of two other stress tensors: the hydrostatic stress tensor $p[\delta]$ and the deviatoric stress tensor $[s]$. The hydrostatic (or volumetric) stress tensor is responsible to distort the volume of the body. On the other hand, the deviatoric stress tensor tends to modify its shape. Hence, the stress tensor is expressed as:

$$[\sigma] = [s] + p[\delta] \tag{29}$$

where $[\delta]$ is the Kronecker delta tensor (with $\delta_{ij} = 1$ if $i = j$ and $\delta_{ij} = 0$ if $i \neq j$) and p is the mean stress (pressure value), which is given by:

$$p = \frac{1}{3}(\sigma_{11} + \sigma_{22} + \sigma_{33}) = \frac{1}{3}I_1 \tag{30}$$

where σ_{11}, σ_{22} and σ_{33} are the principal stresses acting on a body (or the eigenvalues of a problem system), and the coefficient I_1 is the first invariant of the stress tensor. The first (I_1), the second (I_2) and the third (I_3) invariants of the stress tensor are defined as:

$$I_1 = \sigma_{11} + \sigma_{22} + \sigma_{33} \tag{31}$$

$$I_2 = \sigma_{11}\sigma_{22} + \sigma_{22}\sigma_{33} + \sigma_{11}\sigma_{33} - \sigma_{12}{}^2 - \sigma_{23}{}^2 - \sigma_{13}{}^2 \tag{32}$$

$$I_3 = \sigma_{11}\sigma_{22}\sigma_{33} + 2\sigma_{12}\sigma_{23}\sigma_{31} - \sigma_{12}{}^2\sigma_{33} - \sigma_{23}{}^2\sigma_{11} - \sigma_{13}{}^2\sigma_{22} \tag{33}$$

Then, the deviatoric stress tensor can be obtained by subtracting the hydrostatic stress tensor from the stress tensor:

$$[s] = [\sigma] - p[\delta] = \begin{bmatrix} \sigma_{11} - p & \sigma_{12} & \sigma_{13} \\ \sigma_{21} & \sigma_{22} - p & \sigma_{23} \\ \sigma_{31} & \sigma_{32} & \sigma_{33} - p \end{bmatrix} \tag{34}$$

The principal directions of the deviatoric stress tensor coincide with the principal directions of the stress tensor. The invariants of the deviatoric stress tensor are values which satisfy the characteristic equation for the deviatoric stress tensor:

$$det([s] - s[\delta]) = s^3 - J_1 s^2 - J_2 s - J_3 = 0 \tag{35}$$

The values J_1 (or S_I), J_2 (or - S_{II}, since S_{II} = - J_2), J_3 (or S_{III}) are identified as the first, the second and the third invariants of the deviatoric stress tensor, respectively. They are obtained similarly to the invariants of the stress tensor (I_1, I_2 and I_3):

$$J_1 = (\sigma_{11} - p) + (\sigma_{22} - p) + (\sigma_{33} - p) = (\sigma_{11} + \sigma_{22} + \sigma_{33}) - 3p = 0 \tag{36}$$

$$J_2 = \frac{1}{3}I_1{}^2 - I_2 \tag{37}$$

$$J_3 = \frac{2}{27}I_1{}^3 - \frac{1}{3}I_1 I_2 + I_3 \tag{38}$$

The fact that $J_1 = 0$ means that the deviatoric stress tensor describes a state of the body with pure shear.